THÈSE

Présentée pour l'obtention du grade de

DOCTEUR DE L'UNIVERSITÉ LOUIS PASTEUR
STRASBOURG I

Mention: *Physique – Photonique*

par

Olivier MAGNIN

Application de l'optique diffractive à l'hématologie

Soutenue le 12 juillet 2002 devant la commission d'examen:

Membres du jury

Professeur Patrik MEYRUEIS:	Directeur de thèse Professeur à l'ULP, Directeur du LSP
Professeur Joël FONTAINE:	ENSAIS, Strasbourg Rapporteur interne
Professeur Olivier PARRIAUX:	TSI, Saint–Etienne Rapporteur externe
Professeur Pierre AMBS:	ESSAIM, Mulhouse
Patrice TWARDOWSKI:	Maître de conférence à l'ULP Examinateur

Membre invité

Didier LEFEVRE :	Abx Diagnostics (Groupe HORIBA) Directeur adjoint du département Recherche

Table of contents

List of Figures

Publications

- O. Magnin and P. Meyrueis. Design of a diffractive beam shaper adapted to blood cells optical characterization. *Optics Communications*, (Proposed).
- Y. Maruyama, O. Magnin, H. Satonozo and M. Ishikawa. Ground and Excited State Isomerization of Triphenylmethane Dyes in the Femtosecond Regime. *Journal of Physical Chemistry*. Vol. 103, Num. 29, p.5629–2635, 1996.

National Conferences

- Groupement des Industries Françaises de l'Optique (GIFO). "Application de l'optique diffractive à l'hématologie." Strasbourg, France, (October 11, 2001).

Acknowledgment

I would first like to thank Mr. Henri Champseix (Abx Diagnostics R&D manager) and Mr. Didier Lefevre (Abx Diagnostics R&D vice–manager) who have initiated the project of using diffractive optics in Abx Diagnostics future analyzers. This decision to use latest optical technologies in an industrial environment was a challenge to take up for a middle size private company. So, I am especially grateful to them for having supported and trusted me during those years of work.

I also had the opportunity to work with Dr. Sverker Hård (Chalmers University, Göteborg, Sweden) and Dr. Michael Larsson (Radians Innova, Göteborg, Sweden) during the prototyping step of that project. I would like to warmly thank them for the quality of DOEs that were realized and for the advises they gave me.

Finally, I would especially like to give my greatest gratitude to Prof. Patrick Meyrueis (Director of Photonic Systems Laboratory LSP, Strasbourg, France) who has been my supervisor throughout this work. Guidelines he gave me from the earlier steps to the end of that project lead to a particularly efficient work.

Olivier Magnin

Montpellier, May 2002

Abstract

The topic of this thesis is blood cells characterization by optical methods. Throughout this work we propose to design and realize a diffractive beam shaper especially adapted to blood cells differentiation, the beam shaper will be next integrated in a blood cell analyzer.

The proposed diffractive beam shaper is globally optimized taking into account specific constraints of flow cytometry optical measurements as well as constraints linked to diffractive optics design and fabrication. The proposed design will reduce misalignments sensitivity and enhance measurement accuracy at lower cost than standard optical setups.

In order to set the context of the study we first introduce the required hematology and flow cytometry backgrounds. The rest of the work focuses on the proposed diffractive beam shaper synthesis: specifications, phase function determination, prototype fabrication and experimental validation.

Prototypes of the proposed diffractive beam shaper have been realized. Those prototypes have first been tested and validated as stand alone optical components. They have next been integrated in the overall optical blood cells differentiation system. Experiments we have realized have proven that the proposed diffractive beam shaping function is especially adapted to optical blood cells characterization: alignment and tolerancing of one critical component have been relaxed and measurement stability has been enhanced.

Keywords: diffractive optics, beam shaping, kinoform, Computer Generated Hologram, diffraction, scatterring, biophotonics, hematology, flow cytometry, blood cells.

Résumé

Ce travail de thèse porte sur la caractérisation des cellules sanguines par méthodes optiques. Nous proposons de concevoir et fabriquer un élément optique diffractif particulièrement adapté à la différenciation des cellules sanguines et de l'intégrer dans un système approprié.

Ce composant est étudié afin de prendre en compte les contraintes propres à la cytometrie en flux et à la synthèse d'éléments diffractifs. Nous montrons que ce composant permet d'améliorer les perfomances pour un coût de fabrication inférieur aux systèmes actuels.

Compte tenu de la spécificité du domaine de l'hématologie, nous procédons d'abord à une rapide présentation des bases de l'hématologie et de la cytométrie en flux. Nous traiterons ensuite du cahier des charges, de la synthèse et de la réalisation de l'élément diffractif puis de son intégration suivie d'une validation expérimentale.

Nous prenons en charge toutes les étapes: spécifications, calcul de la fonction de phase, simulation des performances et synthèse des fichiers de fabrication. Une fois le prototype réalisé, l'élément diffractif, après avoir été testé isolément, est intégré dans le système optique de caractérisation de cellules sanguines.

Nous discutons ensuite cette intégration. Des tests permettent de mettre en évidence le gain de précision et de fiabilité apporté par le système réalisé. Nous concluons en faisant un bilan des résultats et en présentant des éléments de prospectives.

Chapter 1

Introduction

During the last 15 years the role of optics has become obvious in fields like communication, mass–storage or metrology. Less known is the increasing role it plays in biology and medicine. Ranging from fiber optics endoscope to fluorescence microscopy, biophotonics is now the ultimate tool in many applications. If we restrict our considerations to light–tissue interaction, it is surprising to note that there are still a lot of applications: skin diseases treatment, laser surgery or breast cancer detection.

In the present work we are going to focus on one specific branch of biology: hematology. Hematology is the study of blood cells: their number, their type and their shape. Although largely unknown, hematology dates back to the invention of the optical microscope. It has somehow stagnated until the middle of that century where new tools became available: flow cytometers. Flow cytometers allow measurement of characteristics of biological particles such as bacteria, liposome, blood cells or multi–cellular organisms. Those measurements are made while particles pass, in single file, through the measuring apparatus in a water stream (see Fig. 1.1). Flowing particles (blood cells in our case) are characterized either by interaction with an electric field (see §2.3.1) or by light–particle interaction (see §2.3.2). Light–cell interaction is, by far, the most refined method to get an accurate differentiation of blood cells. It however requires many constraints onto the overall optical detection system.

Blood cells analyzers can roughly be seen as automated flow cytometers. Optical blood cells differentiating systems are embedded in high range analyzers. Our final goal is to design a new optical blood cells characterization system that should enhance performances of actual systems at lower costs. The optical blood cell differentiation system we are going to design can be divided in two parts: blood cell illumination and light–cell interaction measurement. Those two functionalities are of course linked, we then have to

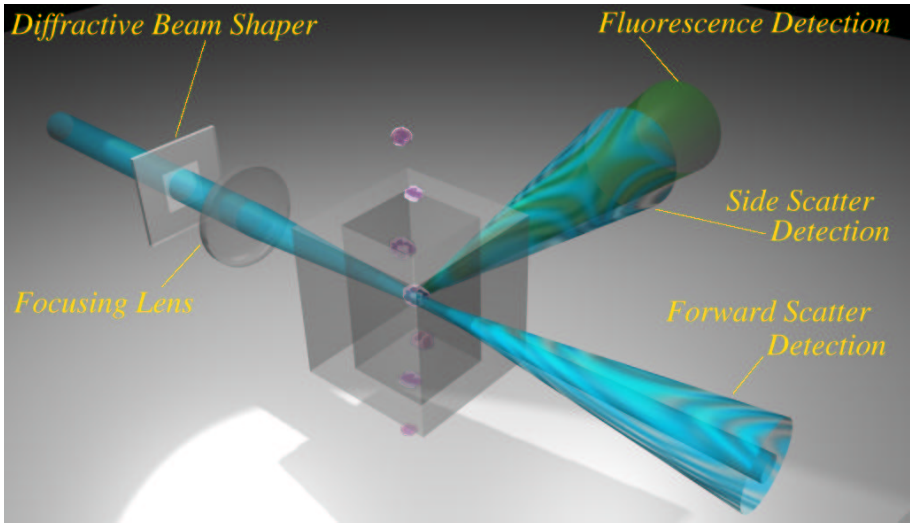

Figure 1.1: Schematic representation of measurement of fluorescence and light diffracted by a white blood cell.

take into account some of the constraints associated to the detection when designing the illumination system. Throughout this thesis we are going to focus on the design of the blood cell illumination system. Enhancements of the light–cell interactions measurement system, although out of the scope of that work, will briefly be discussed in the last chapter.

As depicted figure 1.1, the measurement point is the location where the water stream that transports blood cells crosses the laser beam. So to increase the light–blood cell SNR, the laser beam has to be focused at that point. All cytometers optical setups that have been designed up to now rely on a pair of cylindrical lenses to focus the laser beam. As a consequence, the light intensity distribution at the measurement point is Gaussian along both directions (see Fig. 1.2a). So, the light–blood interaction detected intensity depends on the cell position inside the flowing stream (see Fig. 1.2a). We unfortunately can not avoid those fluctuations of blood cell position inside the stream. To overcome that problem it would be necessary to generate the uniform intensity distribution represented Fig. 1.2b at the measurement point. This, however, can not be done with standard refractive lenses. Throughout this work we propose a new illumination setup that will generate the optimal light distribution of Fig. 1.2b at the measurement point.

We propose to use a diffractive beam shaper to enhance the efficiency of the illuminating system of the optical blood cells differentiation system that will be integrated in future analyzers. This design should take into

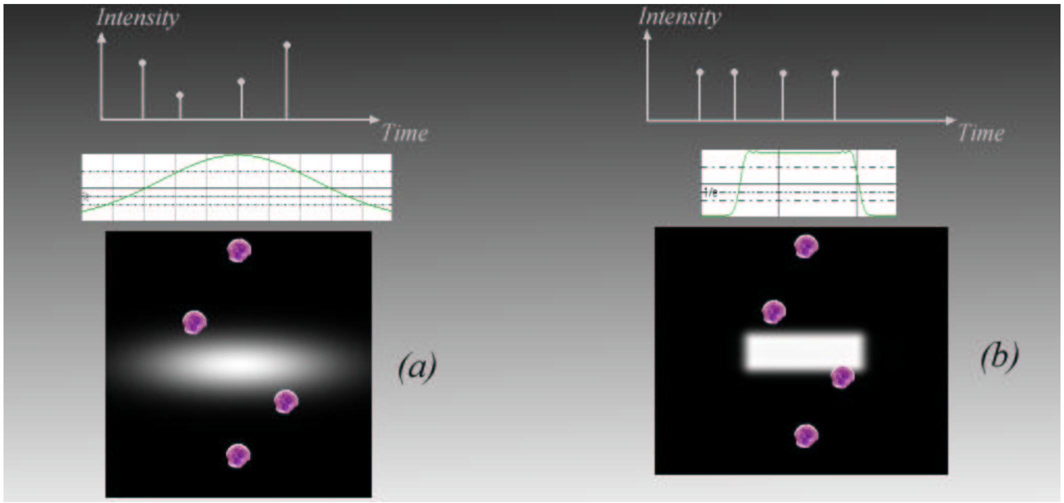

Figure 1.2: Intensity distribution at measurement point in standard optical setups (a); generated with the diffractive beam shaper (b).

account constraints of diffractive optics synthesis as well as constraints that are specific to our application: blood cells characterization. Once the design of this globally optimized diffractive beam shaper will be achieved, prototypes will be realized and tested.

The synthesis of this diffractive beam shaper will be the first step toward a new generation of optical systems dedicated to blood cells differentiation.

Chapter 2

Context of the research: Hæmatology

We have seen in the previous introducing chapter that the goal of our work is to design a new optical system for blood cell characterization. This system, which is based on light–blood cell interaction, will allow simultaneous measurement of three optical parameters (see §2.3.2) for each of the blood cell that are crossing the laser beam one after another. This new optical setup will be integrated in Abx Diagnostics' future top of the range analyzers. Those analyzers can, from a sample of whole blood, give information such as the munber of white and red blood cells and platelets. One can roughly say that blood cells analyzers are automated flow cytometers (see §2.2).

Since blood is definitely the context of the study, we are going to briefly present the different types of blood cells our detector will have to distinguish: red blood cell, reticulocytes, white blood cells (lymphocytes, monocytes, neutrophils, eosinophils) and platelets. We will next introduce flow cytometry and typical optical parameters that are measured in this field.

2.1 Blood essentials

Blood is classified as a connective tissue. In order to be classified as a connective tissue, a tissue must consist of living cells in a non–living matrix. Cells in blood include red and white blood cells and platelets. The matrix in blood is the plasma, which remains liquid unless blood clotting is needed. The function of blood that everyone is familiar with, is the delivery of oxygen to the tissues. Oxygen diffuses into capillaries surrounding the alveoli in the lungs, and as the blood moves through the body oxygen unloads to needy tissues. Carbon dioxide, a waste product of cellular metabolism, will then make the journey back to the lungs in the blood, where it is exhaled. Other cellular wastes are disposed of by the kidneys.

Blood vessels surrounding the stomach and intestines absorb nutrients and water from the food we eat, the nutrients are then distributed throughout the body via the circulatory system. Hormones produced in the endocrine glands also use the blood highway for getting to their target organs and cells.

What changes in body when exercising? Increased heart rate and respiration will certainly occur, as well as sweating, and perhaps a flushed appearance. Why does face get so red when exercise? Blood vessels near the surface of the skin dilate and fill with blood. As the blood moves through these vessels it is cooled, helping to reduce body temperature.

Proteins and other solutes present in the blood help maintain an appropriate pH for the body tissues, and act as buffers. (Buffers are substances which help resist large swings in pH - for instance after you drink a glass of acidic orange juice, blood pH does not drop due to the effect of buffers.) These same proteins and solutes also help maintain blood volume by controlling the rate of osmosis - the movement of water across a differentially permeable membrane. The proteins and solutes remain in the blood vessels, insuring adequate blood volume by causing water to remain in the circulatory system.

White blood cells have the ability to fight off foreign invaders and prevent wide–scale invasion. Blood is also unique because it can prevent the loss of itself. Blood clotting occurs when blood vessels are damaged, preventing excessive blood loss.

The average adult has about five liters of blood living inside of their body. Because it contains living cells, blood is alive. Red blood cells and white blood cells are responsible for nourishing and cleansing the body. Since the cells are alive, they too need nourishment. Vitamins and Minerals keep the blood healthy. The blood cells have a definite life cycle, just as all living organisms do. Approximately 55% of blood is plasma, a straw–colored clear liquid. The liquid plasma carries the solid cells and the platelets which help blood clot. Without blood platelets, it wuld be possible bleed to death. When the human body loses a little bit of blood through a minor wound, the platelets cause the blood to clot so that the bleeding stops. Because new blood is always being made inside of bones, the body can replace the lost blood. When the human body loses a lot of blood through a major wound, that blood has to be replaced through a blood transfusion from other people. But everybody's blood is not the same. There are four different blood types. Blood also has Rh factors which make it even more unique. Blood received through a transfusion must match. Patients who are scheduled to have major surgery make autologous blood donations (donations of their own blood) so that they have a perfect match.

2.1.1 Plasma

It is a straw–colored, clear liquid that is 90% water, and it is an essential ingredient for human survival. It might seem like plasma is less important than the blood cells it carries. But that would be like saying that the stream is less important than the fish that swims in it. You can't have one without the other. Besides water, plasma also contains dissolved salts and minerals like calcium, sodium, magnesium, and potassium. Microbe–fighting antibodies travel to the battlefields of disease by hitching a ride in the plasma. Without plasma, the life-giving blood cells would be left floundering without transportation. Never underestimate the importance of plasma.

2.1.2 Red blood cells

Erythrocytes (red blood cells, or RBCs) constitute the bulk of the blood cells, a sample of blood is composed of approximately 45% erythrocytes. RBCs are biconcave in shape (see Fig. 2.1), which gives the cells some advantages - namely the flexibility needed to move through tiny capillaries; and increased surface area which makes oxygen loading and unloading more efficient. RBCs are anucleate and have a life span of only 100–120 days. RBCs are packed with the protein hemoglobin, which carries oxygen. Hemoglobin is composed

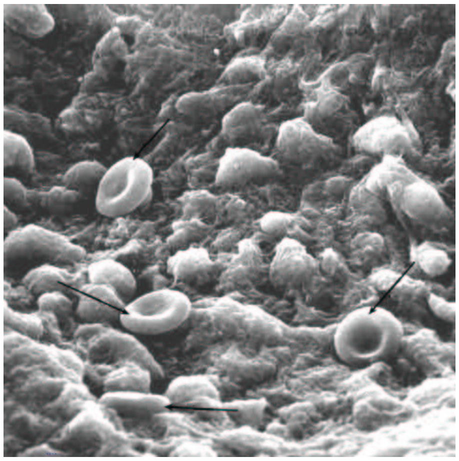

Figure 2.1: Scanning Electron Microscope image of red blood cells (see arrows). Photo: Department of Cell Biology, Vanderbilt University Medical Center.

of four protein chains with a heme group in the middle of each chain. One atom of iron is embedded in the middle of each heme group. A molecule of oxygen can bind with each iron atom, so the maximum amount of oxygen a molecule of hemoglobin can carry is four molecules. All blood cells derive from a common ancestor - the hemocytoblast (blood cell builder). Erythrocyte production is controlled by the hormone erythropoietin, which is made by the kidneys. The kidneys monitor the amount of oxygen in the blood, and when it is low erythropoietin is released. All blood cells are made in red bone marrow found in the ends of some long bones, and in the spongy portions of some flat bones. The formation of red blood cells is known as erythropoiesis. The general term given to the formation of all blood cells is hematopoiesis. Developing red blood cells produce lots of ribosomes. Ribosomes are the site of protein synthesis and juvenile RBCs need to make a lot of proteins (hemoglobin) before they are ready to take on their adult role - carrying oxygen. After the RBC has made all its hemoglobin it ejects its nucleus - quite an unusual thing you might say, and yet it makes perfect sense. The RBCs want to travel light allowing for maximum oxygen carrying capabilities. Mature RBCs are really just cell membranes packed with hemoglobin.

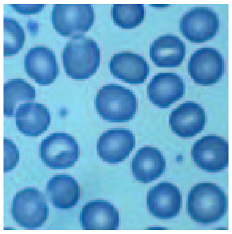

Figure 2.2: Smear of red blood cells.

2.1.2.1 Reticulocytes

Reticulocytes are immature red blood cells that have just been released by marrow of bones in the circulating blood. Unlike mature red blood cells, reticulocytes still have RNA fragments in their cytoplasm (see 2.3). The amount of RNA fragments will decrease progressively with maturation of the cell (see 2.4). After 24 hours the cytoplasm contains no RNA at all; the cell is a mature red blood cell. So the number of reticulocytes in the circulating blood reflects the activity of the marrow of bones and its ability to regenerate red blood cells. The information is of primary importance to detect diseases such as anemia.

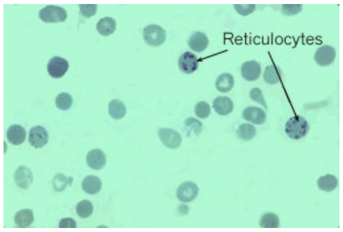

Figure 2.3: Reticulocytes (i.e. immature red blood cells).

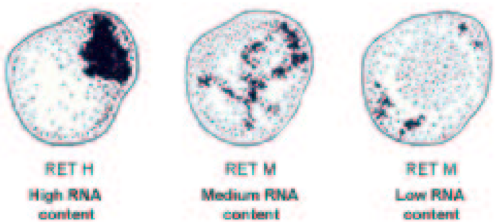

Figure 2.4: Maturation of reticulocytes (i.e. immature red blood cells).

2.1.3 White blood cells

The number of white blood cells, or *leukocytes*, is much smaller than the number of RBCs. Leukocytes reside mainly in the body tissues, and use the circulatory system for transportation. Leukocytes are able to leave the blood vessels and travel throughout the body using a process known as diapedesis. Leukocytes use amoeboid motion to slip through tight spots - one portion of the cell membrane is extended, followed by cytoplasm, followed by more cell membrane, followed by more cytoplasm, ...

Leukocytes can also respond to chemical signals via a process known as chemotaxis. When more leukocytes are needed in a specific area the leukocytes can call in reinforcements by secreting chemicals that other WBCs will respond to.

Leukocytes are classified into two groups based on the presence, or absence, of membrane–bound granules in the cytoplasm, see table 2.1.

2.1.3.1 Basophils

The *basophils* granules contain histamine, which causes inflammation and dilates blood vessels. The blood vessels become leaky leading to tissue swelling. When a foreign allergen invades the body's tissues the basophils respond by

Granular Leukocytes	Agranular Leukocytes
Basophils	Monocytes
Eosinophils	Lymphocytes
Neutrophils	

Table 2.1: White blood cells (leukocytes) are classified according to five sub–populations.

releasing the contents of their granules. Histamine also acts as a chemical signal to recruit other leukocytes to the area. The most aesthetically pleasing of all the leukocytes, the basophils are also the least numerous. They are easily recognized by their very large, deep purple cytoplasmic granules which overlie, as well as flank, the nucleus (eosinophil granules, by contrast, only flank the nucleus but do not overlie it). It is tempting to assume that the basophil and the mast cell are the blood and tissue versions, respectively, of the same cell type. Actually it is controversial as to whether this concept is true or whether these are two different cell types.

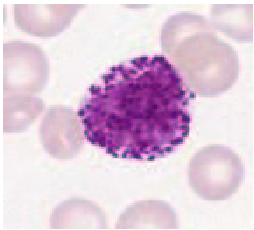

Figure 2.5: Basophil type white blood cell surrounded with red blood cells.

2.1.3.2 Eosinophils

Eosinophils have a particular fondness for parasitic worms. The eosinophils' granules contain digestive enzymes which are released from the cell onto the parasite. A number of eosinophils will gather around the "foreigner", each releasing enzymes which digest the invader. Larger numbers of eosinophils are found in the digestive system and skin - both opportune sites for infection by parasites. Eosinophils are capable of ameboid motion (in response to chemotactic substances released by bacteria and components of the complement system) and phagocytosis. They are often seen at the site of invasive parasitic infestations and allergic (immediate hypersensitivity) responses. Individuals

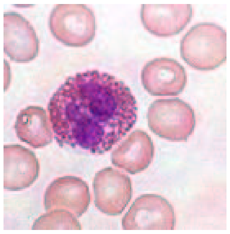

Figure 2.6: Eosinophil type white blood cell surrounded with red blood cells.

with chronic allergic conditions (such as atopic rhinitis or extrinsic asthma) typically have elevated circulating eosinophil counts. The eosinophils may serve a critical function in mitigating allergic responses, since they can 1) inactivate slow reacting substance of anaphylaxis (SRS-A), 2) neutralize histamine, and 3) inhibit mast cell degranulation. The life span of eosinophils in the peripheral blood is about the same as that of neutrophils. Following a classic acute phase reaction, as the granulocyte count in the peripheral blood drops, the eosinophil count temporarily rises.

2.1.3.3 Neutrophils

Neutrophils are especially fond of bacteria and fungi. Their granules contain hydrolytic enzymes and proteins which act like antibiotics. Neutrophils ingest their prey, then inject the contents of their granules into them. Unfortunately the explosive act of killing the prey also kills the neutrophil. They are also the most populous of the circulating white cells (55 to70% of all leukocytes are neutrophils) they are also the most short lived in circulation. After production and release by the marrow, they only circulate for about eight hours before proceeding to the tissues, where they live for about a week, if all goes well. They are produced as a response to acute body stress,

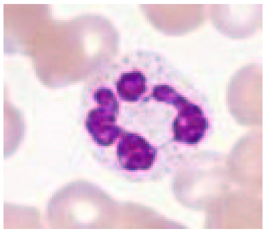

Figure 2.7: Neutrophil type white blood cell surrounded with red blood cells.

whether from infection, infarction, trauma, emotional distress, or other noxious stimuli. When called to a site of injury, they phagocytose invaders and other undesirable substances.

2.1.3.4 Monocytes

Monocytes are known as macrophages once they leave the circulatory system. The macrophages are good all–around killers, able to destroy viruses, bacteria, and parasites. Their name (big–eater) gives a good indication of the activity of this cell type. Macrophages are not particularly selective in their choices any foreign invader will do just fine. Macrophages are good neighbors too, as they help the lymphocytes recognize intruders, helping to initiate the immune response. Most lymphocytes reside in the lymph nodes where they function as part of the immune system. Two distinct types of lymphocytes are found - T cells and B cells. The T cells (called T cells because they mature in the thymus gland) are involved in the hand to hand combat activities of the immune system. T cells are programmed to detect specific foreign antigens, unlike the macrophages, which aren't picky about what they kill. B cells make substances known as antibodies - free-flowing molecules which act like hand grenades when attacking foreign substances. These large cells are actually more closely related to neutrophils than are the other granulocytes, the basophil and eosinophil. Monocytes and neutrophils share the same stem cell. They are produced by the marrow, circulate for five to eight days, and then enter the tissues where they are mysteriously transformed into histiocytes. Here they serve as the welcome wagon for any outside invaders and are capable of processing foreign antigens and presenting them to the immunocompetent lymphocytes. They are also capable of the more brutal activity of phagocytosis. Unlike neutrophils, histiocytes can usually survive the phagocytosis of microbes. What they trade off is killing power.

Figure 2.8: Monocyte type white blood cell surrounded with red blood cells.

For instance, mycobacteria can live in histiocytes (following phagocytosis) for years.

2.1.4 Platelets

Platelets, or *thrombocytes* are not complete cells, they are fragments of an unusual cell type called the megakaryoblast. All blood cells are descendents of the hemocytoblast - the megakaryoblast would be the first generation, as are the erythroblasts which form the RBCs, and the two cell types which eventually become leukocytes. Megakaryoblasts undergo repeated rounds of mitosis (division of the cytoplasm) without undergoing cytokinesis (division of the cytoplasm). The nuclei do not become distinct, instead they merge into one very large and irregularly shaped nucleus. When the cell is mature the plasma membrane begins to form around small segments of the cytoplasm - walling off the cell into thousands of small compartments. Eventually the cell ruptures and the individual membrane bound cell fragments are then called platelets. The most important job of platelets is to help form blood clots.

As a conclusion for this section dedicated to blood essentials, we have to stress that carefull review of peripheral blood adds significant value to the clinical history and physical examination. For that reason flow cytometry plays a role of primary importance aiding in the diagnostic of diseases.

2.2 Introduction to flow cytometry

We have previously mentioned that Abx Diagnostics blood cells analyzers can roughly be considered as automated flow cytometers. Underlying measurements principles are the same and the only differences lye in the fact that standard cytometers require the blood sample to be manually prepared (diluted, addition of lysing agents) whereas those operations are automated in Abx Diagnostics analyzers. We are going to present flow cytometry and then focus on standard parameters that are measured in flow cytometry in which we will include our work.

Cytometry refers to the measurement of the physical and/or chemical characteristics or cells or, by extension, of other biological particles [1][2]. Flow cytometry is a process in which such measurements are made while the cells or particles pass, in single file, through the measuring apparatus in a fluid stream. Biological particles which have been subjected to flow cytometric analysis include viruses, liposomes, bacteria, chromosomes, cell aggregates and multicellular organisms. The first application of flow cytometry was counting the number of particles present in a given sample volume. Most of the present interest of flow cytometers is their ability to quantify and determine the heterogeneity of a cell population. Actual flow cytometers can measure a wide range of parameters, from the particle volume to its DNA contents.

Flow cytometers are also able to sort particles according to some selected characteristics. This is realized by employing electrical or mechanical to divert cells with preselected characteristics from the main stream, and so can be use to isolate subpopulations of cells [3][4][5][1][2]. The most prominent use of flow cytometry in medical practice are in the related fields of laboratory hematology and clinical immunology for a variety of tasks involving blood cell counting and classification. Clinical applications are also being pursed in the fields of genetics, microbiology, pharmacology and toxicology. In order to use flow cytometry to study characteristics of intact cells from sold tissues or tumors, or of cultured cells which grow attached to one another, various methods are used to prepare single cell suspensions from the starting material.

2.3 Measured parameters in flow cytometry

We have seen in chapter 2 that any sample of whole blood contains erythrocytes, leukocytes an platelets. A first separation between various cell populations can be realized by a chemical reagent (a lysing agent) that destroys a specific population (RBCs and platelets) leaving other cells (WBCs) unaffected. The problem is then splitted into two parts. On the one hand red blood cells and platelets, on the other hand the five white blood cells sub–populations. To be able to distinguish between cell types, we have to find a set of parameters that reflect differences from one blood cell to another. Traditional parameters are cell volume, its light transmittance, its diffraction pattern or fluorescence level. For instance if we represent white blood cells volume versus transmittance (see Fig. 2.9) four sub–populations of white blood cells can clearly be distinguished [3][6]. Available technologies for measurement of cell parameters are either electrical (impedance or RF based) or optical (light–blood cell interaction based).

2.3.1 Resistive measurement

One electrical engineer, Wallace Coulter, pursued the goal of blood cells counting. His detection setup was based upon the fact that the electrical conductivity of cell is lower than that of saline solution. Coulter reasoned

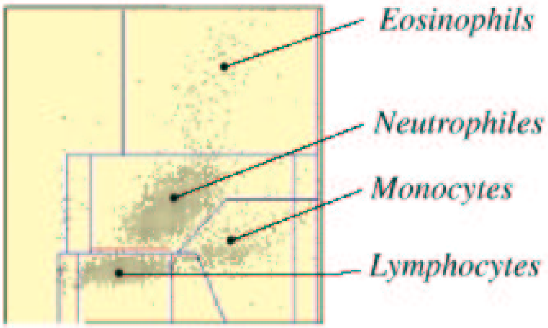

Figure 2.9: Representation of white blood cells volume determined by the impedance method (X–axis) versus their optical transmittance (Y–axis).

that blood cells, suspended in a saline solution and passing one at a time through a small orifice (see Fig. 2.10), would be detectable by the change in electrical impedance of the orifice produced as they passed through [5][2][1]. The electrical conductivity of a blood cell is different from the conductivity of the surrounding saline solution. So anywhere a cell passes through the aperture, the overall conductivity of the cylindrical cross section of Figure 2.10 is modified according to the well known electrical law:

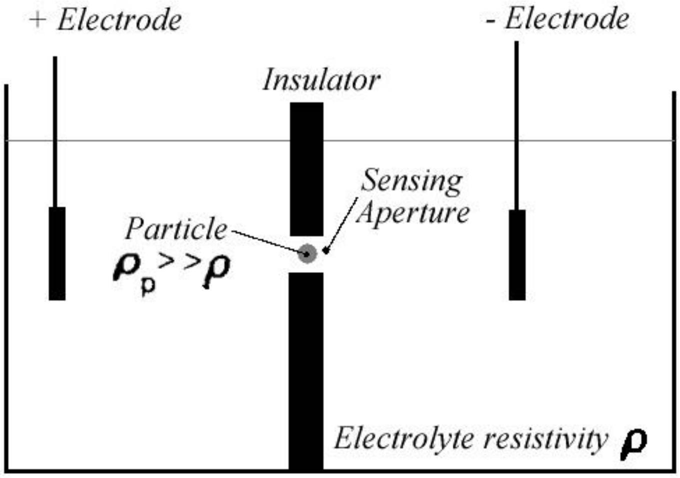

Figure 2.10: Coulter resistive measurement setup for particles (like blood cells) volume determination.

$$\Delta R = (\rho - \rho')V$$

where R is the impedance, ρ the conductivity and V the volume. So, by measuring variations of the impedance of the cylindrical cross section, one can get a direct information concerning the passing blood cell [7].

The first orifice that Coulter realized was made of cellophane wrapper from a cigarette package. The Coulter counter proved accurate for counting and sizing blood cells [7][4]. Apparatus based on this principle are still worldwide used in clinical and research laboratories and allows very accurate measurement of particles ranging from 2μm to 20μm depending on the aperture size [2][1]. Impedance measurement gives the overall volume of a blood cell but gives no information concerning its structure (cytoplasm, kernel, granularity, ...). To get accurate information of concerning cell structure, optical technologies are more adapted.

Another electrical method is used to count blood cells. The setup is quite similar to the previous one (see Fig. 2.10) except that it is based on high frequency current and not DC current like in Coulter principle. This method also gives information concerning the cytoplasm contents.

2.3.2 Standard optical measurements in flow cytometry

Optical detection is, by far, the most refined method to get accurate information concerning blood cells characteristics [6][2][1]. As we are going to see, a blood cell can interact with an incoming light beam in various ways.

2.3.2.1 Blood cells optical transmittance

Although blood cells are basically made of water, they are not perfectly transparent at visible wavelengths. Their index of refraction varies slightly from water index. This allows measurement of the optical transmittance of the blood cell in flowing water [6][2]. Measuring the optical transmittance of a blood cell can be of primary importance to determine its type. For example, Fig. 2.9 represents volume (X–axis) versus optical transmittance (Y–axis) of white blood cells. It is obvious, observing the diagram, that light transmittance parameter provide a significant opportunity in the determination of white blood cells sub–populations.

2.3.2.2 Light scattering by blood cells

Blood cells contain many structures, like RNA structures, whose dimensions are small enough to diffract visible light. This means that any illuminated cell will produce a diffraction pattern that reflects its structure. Then, one

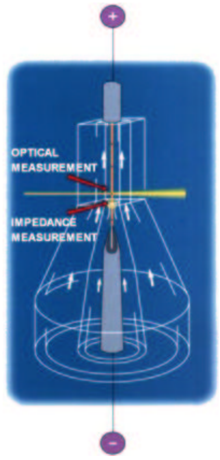

Figure 2.11: Volume impedance and light transmittance measurements of a blood cell.

could think of an ideal detection device that maps a 4π steradiant sphere centered on the cell to collect the full diffraction pattern. Such device have been realized, and experiments [6][8] have proven that those measurements can be reduced to measurement of diffracted light along two directions : the forward scatter (very small angle diffraction) and the side scatter (right angle diffraction) [3][9][8].

Forward scatter basically gives information related to the cell volume. That parameter is pretty close to the volume measured by the impedance method (see §2.3.1). Nevertheless it allows detection of much smaller cells (platelets) than impedance method [2][1][10].

Side scatter is sometimes assimilated to diffusion. Intensity of diffused light depends on the contents of the cytoplasm [2][1]. If the cell has a mucleus, then its very fine structures (like RNA structures) will diffract light over a wide angle range: diffraction states that the finer the structures are, the stronger incoming light rays will be bend [11][2][1]. That is, cells with high cytoplasm contents will give a strong side scatter signal whereas cells with no nucleus will give a weak side scatter signal [2][1].

2.3.2.3 Blood cells and fluorescence

Fluorescence methods typically distinguish cells that are labeled with a dye molecule [1][2]. In the example of reticulocytes, cells are labeled with an RNA specific dye: thiazole orange. In case of presence of RNA in the cell cytoplasm, the RNA–thiazole orange complex will emit fluorescence light at

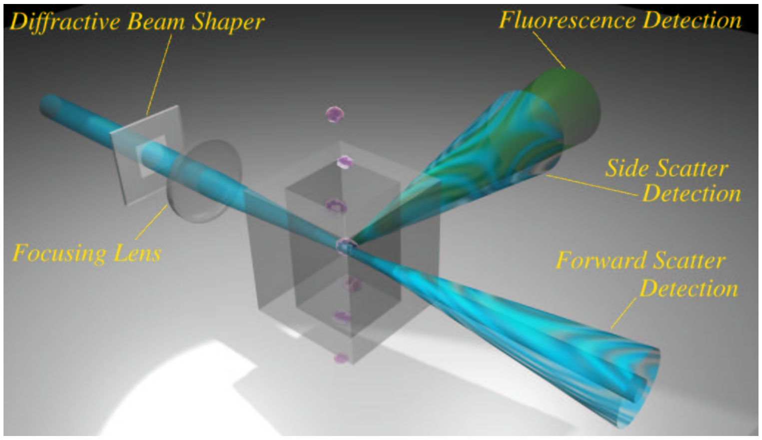

Figure 2.12: Schematic representation of measurement of forward scatter, side scatter and fluorescence of white blood cells.

530nm when excited with a 488nm Argon ion laser. If the cell's cytoplasm does not contains any RNA fragment, no RNA–dye complex is formed and only weak residual fluorescence light is detected [10].

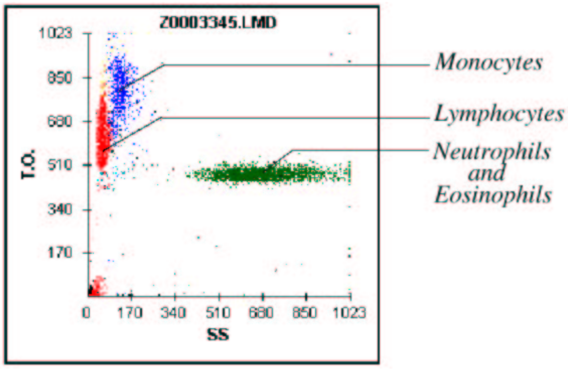

Figure 2.13: Fluorescence (Y–axis) versus large angle scattering (X–axis) parameters diagram for white blood cells.

2.3.2.4 Blood cell and light polarization

Experiments have been realized to determine white blood cells sub–populations using polarization of large angle scattered light [1][2]. This method is based on the fact that large diffracting structures ($\approx \lambda$) tend to leave the polarization state unchanged, whereas fine diffracting structures ($\ll \lambda$) usually modify the polarization state [11]. So, by splitting the diffracted light into two channels with perpendicular polarizers, it is possible to get two independent measured parameters for each cell. We then obtain a 2D representation where sub–populations of white blood cells are distinguishable.

In that chapter we have introduced the context of our research; hematology and blood cells. We have seen that blood cells can be accurately differentiated using dedicated optical setups that measure parameters such as diffraction or fluorescence.

In the rest of that work we are going to focus on the light distribution at the measurement point. This point is the location where the stream that transports blood cells crosses the laser beam. It is, of course, located inside the flow cell (see Fig. 2.12 and Fig. 2.11).

As we are going to see, our setup will rely on diffraction for two reasons. The first one has been exposed previously; we are going to measure light diffracted by blood cells. But we are also going to see that diffraction will play an important role in the generation of the desired light distribution at the measurement point. For this reason, the next chapter will start by a short discussion on physics of diffraction.

Chapter 3

Diffractive Optical Elements

The previous two chapters were dedicated to the overall presentation of our working environment and goals. We have seen in chapter 2 that hematology is the context of our study and that our goal is the design a new generation of optical system for blood cell characterization. This optical system will be integrated in future blood cell automated analyzers. Since blood cells analyzers are basically automated flow cytometers, we have presented in section 2.3 parameters that are usually measured in flow cytometry. But we have not turned our attention to the underlying technology that allows the determination of those parameters.

In that chapter, we are going to introduce an innovating technology, diffractive optics, that will both enhance the measurement accuracy and lower fabrication costs of the new optical system targeted. The role that diffractive optics will play in our application has already been briefly explained in chapter 1 and will be further detailled in chapter 4. We are then going to focus on diffractive optics technology in this chapter. We are first going to thoroughly study the physics of diffraction since it is the basis of both diffractive optics and blood cell scattering. We will then get a general view of diffractive elements synthesizing methods and fabrication.

3.1 Introduction

Bending light beams by diffraction has been known from a long time (Fresnel zone plate) but until recently, diffractive optical components were only used where chromatic behavior was desired. Controling propagation of light with diffractive components really appeared with the invention of holography by Gabor in 1948. With holography it has become possible to control propagation of light so that a previously optically recorded diffractive component can reconstruct the in–depth image of an existing object. Synthesis of such holograms are based on an interferometric record of a real object. In the late 60's modern technology (computer and microlithography) made possible the generation of artificially–computed interferometric records: digital holography was born. The first *Computer Generated Hologram* (CGH) or *Diffractive Optical Element* (DOE) was realized by Brown and Lohmann [12]. Those DOEs gave rise to many interest since it was then possible to modify the propagation of light so that objects that have no real existance are reconstructed.

Computer generated elements were first fabricated with binary amplitude masks [12]. This fabrication method allowed only very limited diffraction efficiency [13]. In the 1980's it was suggested that only the modulation of the phase of an incoming beam was necessary to perform the CGH function [14][15]. This was achieved by generating height reliefs on one surface of a transparent substrat (see Fig. 3.1). As light traverses the plate, the relief modulates the phase of the beam thereby the intensity distribution is modified in a plane behind the diffractive element. Those phase–only diffractive elements or equivalentely *kinoform* absorb no energy and allow generation of one single diffraction order that leads to high diffraction efficiency. Fabrication of those kinoforms started in the 80's using photolithographic methods [16][17].

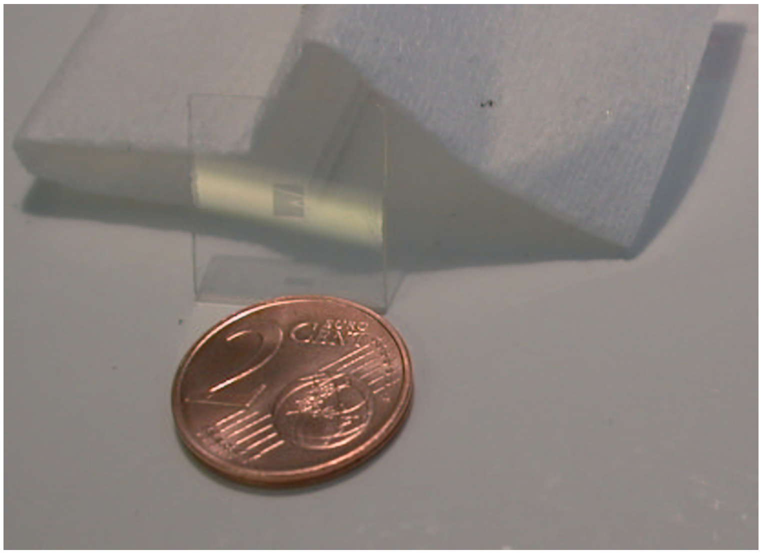

Figure 3.1: Phase only diffractive element (kinoform). Diffracting surface reliefs can clearly be seen at the center of the glass plate.

Diffractive optical elements are today widely used in applications as various as laser machining [18], laser printing, telecom engineering, optical image processing or metrology. Computer generated holograms can perform very complex tasks as splitting, focusing or redistributing an incoming light beam.

Analysis of DOEs is crucial for an understanding of this technology, equally important is the understanding of their design. Diffraction is the basis of computer generated holograms, to be able to synthesize DOE it is first necessary to thoroughly study mechanisms of diffraction. So we will be able to answer to the DOE synthesizing question: what diffracting structure gives the desired distribution of light? Furthermore, measured parameters in hematology also rely on diffraction of light by a blood cell (see §2.3). Since diffraction is definitely the cornerstone of our work, we are going to set strong basis of physics of diffraction in the next sections.

3.2 Diffraction

As explained in the previous two chapters, the new blood cells counting optical system we are going to design relies on diffraction for two reasons. The first reason is explained in section 2.3.2: flow cytometry involves measurement of diffraction of an incoming laser beam by a blood cell. The second reason was exposed in the previous section: diffractive optics will play a major role in the design of the optical blood cell characterization setup we propose.

In the following sections we are going to introduce the physics of diffraction that will be intensively used through the rest of that work.

3.2.1 Background

Refraction and reflexion are phenomena that can bend light rays along their propagation. Refraction occurs in a region were there is a change of the local velocity of the light wave. At the boundary between two media of different refractive index, rays are bent according to the Snell's law:

$$n \sin\theta = n' \sin\theta' \tag{3.1}$$

which is the basement of geometrical optics. It should be noticed that incident and refracted rays are located in two different media. Reflexion also bends light rays but occurs at an interface. Incident and reflected rays still belong to the same media. Angle of incident and reflected rays with respect to the interface normal are equal. Refraction and reflexion are enough to accurately describe a very wide range of optical systems. Nevertheless, it has been noticed very early that light beams are sometimes bent in a way neither refraction nor reflexion can explain. In particular, if we examine thoroughly the region just next to an aperture stop, we would notice that light distribution is not what we could have expected. Transition between shadow and light is not sharp but rather gradual. With an even closer look, it is also possible to distinguish intensity oscillations between bright and dark regions. In that case, reflexion and refraction laws are inadequate to describe propagation of light; diffraction theory has to be introduced.

Diffraction comes from the limitation of the lateral extend of a wave. This phenomenon was observed for the first time by Leonardo da Vinci (1452–1519) in a very rough way. The first accurate description of diffraction was introduced by Grimaldi (1618–1663) in his book[1] published in 1665; that is, two years after his death. At those times corpuscular theory, that was widely believed to describe accurately light propagation, failed to explain diffraction phenomenon. Christian Huygens (1629–1695) , in the year 1678, proposed a wave theory for propagation of light that described diffraction as *a source of secondary spherical disturbance.* Sir Isaac Newton (1642–1727)has been a strong adviser of the corpuscular theory since 1704. His strong influence over contemporary scientists stopped progress in understanding diffraction during the whole 18th century. In the year 1804 Thomas Young (1773–1829) introduced the concept of interferences that directly proceeds from the wave nature of light. Augustin Jean Fresnel (1788–1827) brought together ideas of Huygens and Young in his famous memoir[2]. In 1860, James Clerk Maxwell (1831–1879) identified light as an electromagnetic wave. Gustav Kirchhoff (1824–1887) gave a more mathematical form to Fresnel expression of diffraction. His work basically relies on two assumptions concerning the field at the diffracting aperture. Although those assumptions were quite empirical, his formulation gives a very good approximation of the real diffracted field. In the year 1884, Arnold J.W. Sommerfeld (1868–1951) modified Kirchhoff's theory. Thanks to Green's theorem he suppressed one of the two assumptions Kirchhoff made earlier to derive the so called Rayleigh–Sommerfeld diffraction theory. Later, Sommerfeld was also the first to find the full rigorous solution to the problem of diffraction by a conducting half–plane [11].

---

[1] F.M. Grimaldi *Physico-Mathesis de lumine, coloribus, et iride* (Bologna, 1665).

[2] A. Fresnel, *Mém. de l'Acad. Sci. Paris* (1850).

3.2.2 Rigorous diffraction theory

Light is identified as an electric field $\vec{\mathcal{E}}$ and a magnetic field $\vec{\mathcal{H}}$ linked by the so called Maxwell's equations:

$$\begin{aligned} curl\,\vec{\mathcal{E}} &= -\mu\frac{\partial\vec{\mathcal{H}}}{\partial t} & \qquad div\ \epsilon\vec{\mathcal{E}} &= 0 \\ curl\,\vec{\mathcal{H}} &= \epsilon\frac{\partial\vec{\mathcal{E}}}{\partial t} & \qquad div\ \mu\vec{\mathcal{H}} &= 0 \end{aligned} \tag{3.2}$$

where ϵ and μ are permittivity and permeability tensors related to the medium properties. If we restrict our analysis to a linear, isotropic but non–homogeneous medium $\epsilon = \epsilon(x, y, z)$ and $\mu = \mu(x, y, z)$ are scalar functions depending on position only (time–dependence is not considered here). It's then possible to derive equations in which either $\vec{\mathcal{E}}$ or $\vec{\mathcal{H}}$ fields appear separately:

$$\begin{aligned} \nabla^2\vec{\mathcal{E}}-\epsilon\mu\frac{\partial^2\vec{\mathcal{E}}}{\partial t^2} &+ grad\,(\ln\mu)\times rot\left(\vec{\mathcal{E}}\right)+grad\left(\vec{\mathcal{E}}\cdot grad\,(\ln\epsilon)\right) &= 0 \\ \nabla^2\vec{\mathcal{H}}-\epsilon\mu\frac{\partial^2\vec{\mathcal{H}}}{\partial t^2} &+ grad\,(\ln\epsilon)\times rot\left(\vec{\mathcal{H}}\right)+grad\left(\vec{\mathcal{H}}\cdot grad\,(\ln\mu)\right) &= 0 \end{aligned}$$

If we further restrict our analysis to a linear, isotropic and homogeneous medium, permittivity and permeability are then scalar constants $\epsilon = C^{te}$ and $\mu = C^{te}$ and all gradient functions are null functions. Previous equations become:

$$\nabla^2\vec{U} - \frac{1}{v^2}\frac{\partial^2\vec{U}}{\partial t^2} = 0 \tag{3.3}$$

where $v = 1/\sqrt{\epsilon\mu}$ is the velocity of propagation in the medium and $\vec{U}$ represents either $\vec{\mathcal{E}}$ or $\vec{\mathcal{H}}$. Equation (3.3) is known as the *vector wave equation.* Re–writting this equation for each vector components in a rectangular basis gives:

$$\begin{cases} \nabla^2 U_x - \dfrac{1}{v^2}\dfrac{\partial^2 U_x}{\partial t^2} = 0 \\ \nabla^2 U_y - \dfrac{1}{v^2}\dfrac{\partial^2 U_y}{\partial t^2} = 0 \\ \nabla^2 U_z - \dfrac{1}{v^2}\dfrac{\partial^2 U_z}{\partial t^2} = 0 \end{cases}$$

Keeping in mind that $\vec{U}$ represents either $\vec{\mathcal{E}}$ or $\vec{\mathcal{H}}$. All components of the field obviously have to satisfy to the same equation. This can be summarized within a single *scalar wave equation*:

$$\nabla^2 U - \frac{1}{v^2}\frac{\partial^2 U}{\partial t^2} = 0 \tag{3.4}$$

In the very specific case of monochromatic plane waves, amplitude and phase of any of the field components can be represented by a complex function of position and time:

$$U(x, y, z; t) = A(x, y, z)\mathrm{e}^{-j\varphi(x,y,z)}\mathrm{e}^{j\omega t} \tag{3.5}$$

where $\omega = 2\pi\nu$ and φ is the phase of the wave. Eq. (3.4) can then be re–written:

$$(\nabla^2 + k^2)U = 0 \tag{3.6}$$

where the wave number $\vec{k}$ is defined as $k = \frac{2\pi}{\lambda}$ with λ wavelength in the dielectric medium and $\vec{r} = x\vec{u_1} + y\vec{u_2} + z\vec{u_3}$ is the vector position[3]. Equation (3.6) is a time–independent equation known as *Helmholtz equation.* Any space–dependent part of a propagating strictly monochromatic scalar wave has to obey equation (3.6).

It should be noticed that the only approximation we made to derive eq.(3.4) concerns the medium in which light propagates. For free space propagation of light (i.e. no limitation of its lateral extend, no boundary conditions), eq.(3.4) is not an approximation but the accurate description of what happens. In the case of propagation of light through an index step like an air–glass interface (see Fig. 3.2), things get more complicated. At the air–glass boundary the assumption of homogeneous and isotropic medium is, of course, no longer valid. We should then expect some deviation between the scalar theory and the real diffracted fields. Let's consider the case of a linear, non–isotropic and non–homogeneous medium, ϵ and μ are tensors and the Maxwell's vector equation $curl\vec{\mathcal{H}} = \epsilon\frac{\partial\vec{\mathcal{E}}}{\partial t}$ can be re–written:

$$curl\ \vec{\mathcal{E}} = -\begin{pmatrix} \epsilon_{00} & \epsilon_{01} & \epsilon_{02} \\ \epsilon_{10} & \epsilon_{11} & \epsilon_{12} \\ \epsilon_{20} & \epsilon_{21} & \epsilon_{22} \end{pmatrix} \begin{bmatrix} \frac{\partial\mathcal{H}_x}{\partial t} \\ \frac{\partial\mathcal{H}_y}{\partial t} \\ \frac{\partial\mathcal{H}_z}{\partial t} \end{bmatrix}$$

Examining previous system along the first unit vector of a rectangular basis, it becomes:

$$\frac{\partial\mathcal{E}_z}{\partial y} - \frac{\partial\mathcal{E}_y}{\partial z} = \epsilon_{00}\frac{\partial\mathcal{H}_x}{\partial t} + \epsilon_{01}\frac{\partial\mathcal{H}_y}{\partial t} + \epsilon_{02}\frac{\partial\mathcal{H}_z}{\partial t}$$

---

[3] Refractive index of a medium is defined as $n = \sqrt{\frac{\epsilon\mu}{\epsilon_0\mu_0}}$ where ϵ_0 and μ_0 are vacuum permittivity and permeability. Since we will only consider non–magnetic media, $\mu = \mu_0$ and $n = \sqrt{\frac{\epsilon}{\epsilon_0}}$.

At the boundary $\vec{\mathcal{E}}$ and $\vec{\mathcal{H}}$ vectors components are not independent. It appears clearly that y and z components of the $\vec{\mathcal{E}}$ field are not only coupled one to another, but also coupled with $\vec{\mathcal{H}}$ field components. As a result, amplitude and phase of diffracted fields at the step differ depending on whether they are evaluated with scalar or rigorous theory (see Fig. 3.2). Scalar theory expect no amplitude variations and a perfect phase step, whereas rigorous theory (i.e. real diffracted fields) shows no sharp discontinuity but ripple oscillations at the interface. It is worth stressing that deviation between scalar and rigorous theory is noticeable in the immediate vicinity of the interface or at the edges of the limiting aperture only. So as soon as we are a few wavelengths away, scalar and rigorous theory are pretty close and coupling can safely be ignored.

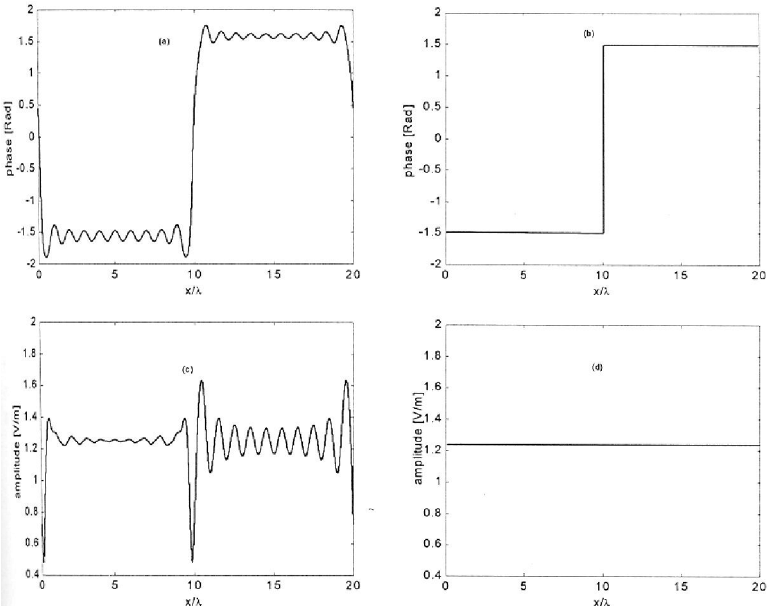

Figure 3.2: Amplitude and phase of the field at a step discontinuity having a height of 2π in a material of index n=1.5 . Evaluation by scalar diffraction theory (right) and rigorous diffraction theory (left).

For that reason we are only going to consider scalar diffraction in our optical blood cell counting setup. The smallest cell present in blood is platelet with dimensions more than ten times the measuring wavelength (see chapter 5). Concerning diffractive elements, we will also see in chapter 5 that the chosen feature size is also about ten times the illuminating wavelength. In that case we can safely consider our diffractive phase elements as thin phase–plates. So, in the followinf report of our work, computer generated holograms will be referenced by their phase functions $\varphi(x,y)$ and the complex amplitude notation will be used to perform all the scalar diffraction calculations.

3.2.3 Full scalar diffraction

Let's consider an arbitrary wave front $U(x,y;z)$ propagating from $z=0$ along the positive z axis of a Cartesian basis. This arbitrary wave front can be Fourier–transformed as:

$$\mathcal{U}(u,v;z)=\iint_{-\infty}^{\infty} U(x,y;z)\mathrm{e}^{-2\pi j(ux+vy)}dxdy \tag{3.7}$$

The arbitrary wavefront $U(x,y;z)$ can then be considered as the inverse Fourier transform of $\mathcal{U}(u,v;z)$ defined by the inverse Fourier transform:

$$U(x,y;z)=\iint_{-\infty}^{\infty} \mathcal{U}(u,v;z)\mathrm{e}^{2\pi j(ux+vy)}dudv \tag{3.8}$$

that is $U(x,y;z)$ can be seen as an infinite composition of the set of functions $\mathrm{e}^{-2\pi j(ux+vy)}$ weighted by $\mathcal{U}(u,v;z)$ components. Keeping in mind the complex representation plane waves eq.(3.5), it is obvious that $\mathrm{e}^{-2\pi j(ux+vy)}$ can be seen as a plane wave propagating in the z direction with direction cosines $(\lambda u;\lambda v;\sqrt{1-\lambda^2u^2-\lambda^2v^2}\ )$. That means $U(x,y;z)$ has been decomposed over a plane waves basis weighted by $\mathcal{U}(u,v;z)$ functions. We define $\mathcal{U}(u,v;z)$ as the *angular spectrum* of the field $U(x,y;z)$.

Now let's examine how the angular spectrum propagates from a $z=0$ plane to another parallel plane defined by $z=z_0$. That is, we have to find a relation between $\mathcal{U}(u,v;0)$ and $\mathcal{U}(u,v;z_0)$ with $z_0>0$. According to the scalar diffraction theory (see §3.2.2) the space–dependent part of any propagating field $U(x,y;z)$ has to obey the Helmholtz equation (3.6):

$$\left(\nabla^2+k^2\right)U(x,y;z)=0 \tag{3.9}$$

Since $U(x,y;z)$ can be represented by eq.(3.8) the previous equation becomes:

$$\begin{split}\nabla^2\left(\iint_{-\infty}^{\infty}\mathcal{U}(u,v;z)\mathrm{e}^{2\pi j(ux+vy)}dudv\right)\\ +k^2\left(\iint_{-\infty}^{\infty}\mathcal{U}(u,v;z)\mathrm{e}^{2\pi j(ux+vy)}dudv\right)=0\end{split}$$

We finally get the differential equation:

$$\frac{\partial^2 \mathcal{U}}{\partial z^2}(u,v;z) + k^2(1-\lambda^2u^2-\lambda^2v^2)\mathcal{U}(u,v;z) = 0$$

where an obvious solution is:

$$\mathcal{U}(u,v;z) = \mathcal{U}(u,v;0)\mathrm{e}^{jkz\sqrt{1-\lambda^2u^2-\lambda^2v^2}} \tag{3.10}$$

So the effect of propagation along z axis is only described by the phase factor $\mathrm{e}^{jkz\sqrt{1-\lambda^2u^2-\lambda^2v^2}}$.

So, we have demonstrated that the optical disturbance can be decomposed in an infinite sum of planes waves, each traveling in direction given by components:

$$\begin{cases} u^2 \\ v^2 \\ \sqrt{1-u^2-v^2} \end{cases}$$

where u and v were chosen to be cosines director of $\vec{k}$. This ensure we have $1-u^2-v^2>0$. But if we were[4] to have $1-u^2-v^2<0$ we would get the following relation:

$$\begin{cases} u^2 \\ v^2 \\ j\sqrt{u^2+v^2-1} \end{cases}$$

which represents a wave that rapidly vanishes due to the positive real term in the exponential. Those are evanescent waves.

We have demonstrated that knowing the field at a point Z_0, it's possible to evaluate it at Z $(Z-Z_0>0)$ with very few approximations. We just have to take the angular spectrum of the field, multiply each term of the angular spectrum by a Z–linear phase factor, and transform it back using inverse angular spectrum relation.

Diffraction calculations based on the propagation of angular spectrum is the most refined model for evaluation of diffracted fields [19][11]. It only relies on the linear, isotropic and homogeneous properties of the medium and on the fact that apertures (or interfaces) are large with respect to the wavelength. It is, however, probably not the most convenient tool to solve general purpose problems. Angular spectrum calculations require that both diffraction and calculated surfaces are plane and parallel [20][21], which is

---

[4] Since (u,v) are cosines director we, theoretically, can't have $1-u^2-v^2<0$. However the scalar theory neglects ripple oscillations of the field at the aperture boundary so the case $1-u^2-v^2<0$ might happen and corresponds to a real phenomenon.

seldom the case in optics where surfaces are rather curved than planes. For that reason other theories like Fresnel–Kirchhoff, although less accurate, have proven their utility.

3.2.4 Fresnel–Kirchhoff diffraction integral

Fresnel–Kirchhoff theory relies on the Kirchhoff–Helmholtz integral theorem. As shown in Appendix A, this theorem is derived from the Helmholtz equation and the Green's theorem. The Kirchhoff–Helmholtz integral theorem expresses the optical disturbance at a point in terms of its values and values of its first derivative on a surrounding volume:

$$U(P_0) = \frac{1}{4\pi} \iint_{\mathcal{A},\mathcal{B},\mathcal{C}} \frac{1}{s} \mathrm{e}^{jks} \left(U \left(jk - \frac{1}{s} \right) - \frac{\partial U}{\partial n} \right) ds$$

where U is the disturbance to be determine and $G = \frac{1}{s}\mathrm{e}^{jks}$ the auxiliary Green's function. The Kirchhoff–Helmholtz integral theorem, of course, imply that conditions of validity of scalar theory are met. That is, we only consider large diffracting apertures compared to the wavelength. Let's consider the following setup According to Fig. 3.3 the Kirchhoff–Helmholtz integral can be evaluated using the three surfaces $\mathcal{A}$, $\mathcal{B}$ and $\mathcal{C}$. Surface $\mathcal{A}$ is the hole of the aperture. Surface $\mathcal{B}$ is the hidden surface just next to the aperture. Surface $\mathcal{C}$ a portion of the sphere of radius R centered on P. It can be shown (see [19] p.43) that the contribution of the spherical cap $\mathcal{C}$ to the integral

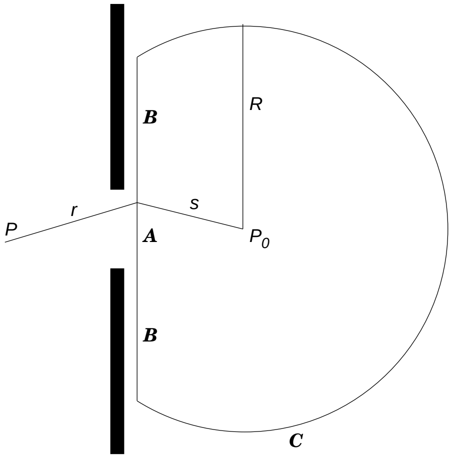

Figure 3.3: Volume and surfaces of integration used to derived the Fresnel–Kirchhoff integral.

3.2.4 is zero. To evaluate the integral 3.2.4 on surfaces $\mathcal{B}$ and $\mathcal{C}$, Kirchhoff made two assumptions:

1. On surface $\mathcal{B}$ we have $U = 0$ and $\frac{\partial U}{\partial n} = 0$.
   That is, on the region shadowed by the screen the disturbance *and* its first derivative are null.
2. On surface $\mathcal{A}$ we have $U = U^i$ and $\frac{\partial U}{\partial n} = \frac{\partial U^i}{\partial n}$.
   Over that surface the disturbance and its first derivative are exactly what they would be without the opaque screen.

In that case, the integral 3.2.4 reduces to the integral over surface $\mathcal{A}$:

$$U(P_0) = \frac{1}{4\pi} \iint_{\mathcal{A}} \frac{1}{s} \mathrm{e}^{jks} \left(U \left(jk - \frac{1}{s} \right) - \frac{\partial U}{\partial n} \right) ds \tag{3.11}$$

If we further consider that the aperture is illuminated by a spherical diverging wave, the disturbance U, the auxiliary function G and their first derivative are:

$$U = \frac{1}{r} \mathrm{e}^{jkr} \qquad \frac{\partial U}{\partial n} = \left(jk - \frac{1}{r} \right) \mathrm{e}^{jkr} \cos(\vec{n}, \vec{r})$$

$$G = \frac{1}{s} \mathrm{e}^{jks} \qquad \frac{\partial G}{\partial n} = \left(jk - \frac{1}{s} \right) \mathrm{e}^{jks} \cos(\vec{n}, \vec{s})$$

Considering that we only evaluate the optical disturbance at points far from the aperture, we furthermore have $k \gg \frac{1}{r}$ which simplify previous relations to:

$$U = \frac{1}{r} \mathrm{e}^{jkr} \qquad \frac{\partial U}{\partial n} = jk\mathrm{e}^{jkr} \cos(\vec{n}, \vec{r})$$

$$G = \frac{1}{s} \mathrm{e}^{jks} \qquad \frac{\partial G}{\partial n} = jk\mathrm{e}^{jks} \cos(\vec{n}, \vec{s})$$

Reporting those expressions in the integral 3.11 gives the *Fresnel–Kirchhoff diffraction integral*:

$$U(P_0) = \frac{1}{j\lambda} \iint_{\mathcal{A}} \frac{\mathrm{e}^{jk(r+s)}}{rs} \left[\frac{cos(\vec{n}, \vec{r}) - cos(\vec{n}, \vec{s})}{2} \right] ds \tag{3.12}$$

Finally in the very specific case of normally incident plane wave illumination eq. 3.12 becomes:

$$U(P_0) = \frac{1}{j\lambda} \iint_{\mathcal{A}} \frac{\mathrm{e}^{jk(r+s)}}{rs} \left[\frac{1 + cos\theta}{2} \right] ds \tag{3.13}$$

It has experimentally been proven [22][23] that Fresnel–Kirchhoff diffraction theory gives the diffracted fields with an excellent accuracy[24][25]. This is the reason why Fresnel–Kirchhoff diffraction integral is widely used[26].

We, however, have to notice that Fresnel–Kirchhoff theory has inconsistencies. The assumptions Kirchhoff made for surface $\mathcal{B}$ require that both the field and first derivative to be zero. It can be shown that if those requirements are met, the field must be identically zero everywhere. Moreover the approximation $k \gg \frac{1}{r}$, although valid when we are many wavelengths away from the aperture, leads to wrong results as soon as we get closer to the diffracting screen. That is why light distribution at the aperture is different from what Kirchhoff's assumptions involve.

In the next chapter we will see that either one of the two assumptions is enough: $U = 0$ *or* $\frac{\partial U}{\partial n} = 0$. Depending on the chosen assumption we get either the first or the second Rayleigh–Sommerfeld diffraction integral for the diffracted field.

3.2.5 Rayleigh–Sommerfeld theory

Although the Fresnel–Kirchhoff diffraction integral gives excellent results, some inconsistencies in this theory have driven the need for a more mathematically accurate formulation of the diffraction integral. As we have seen in §3.2.4, the two Kirchhoff's assumptions $U = 0$ and $\frac{\partial U}{\partial n} = 0$ lead to the mathematical conclusion that the disturbance must be identically zero everywhere (see [23] p.199). To solve this contradiction Rayleigh shown that either $U = 0$ or $\frac{\partial U}{\partial n} = 0$ is enough to derive another relation: the Rayleigh–Sommerfeld diffraction integral.

The Rayleigh–Sommerfeld diffraction integral also relies on the Kirchhoff–Helmholtz integral theorem (see A.5). This involve that we are still dealing with apertures large compared to the wavelength:

$$U(P_0) = \frac{1}{4\pi} \iint_{\mathcal{A}} \frac{1}{s} \mathrm{e}^{jks} \left(U \left(jk - \frac{1}{s} \right) - \frac{\partial U}{\partial n} \right) ds$$

We also keep the same Green's auxiliary function $G = \frac{1}{s}\mathrm{e}^{jks}$ but the volume $\mathcal{V}$ of integration differs. Considering two symmetric points its possible to derive the two kind of Rayleigh–Sommerfeld diffraction formulae:

$$U(x, y, z) = \frac{1}{2\pi} \iint_{\mathcal{A}} U(x', y', z') \frac{\partial}{\partial z'} \left(\frac{\mathrm{e}^{jks}}{s} \right) ds$$

The first solution is obviously based on the first Kirchhoff's assumption $U = 0$ while the second one is based on the second Kirchhoff's assumption $\frac{\partial U}{\partial n} = 0$.

As we did in the case of Fresnel–Kirchhoff integral, we suppose that the field inside the aperture hole is exactly what it would be without the aperture. If we further consider a diverging spherical incident wave:

$$U = \frac{1}{r}\mathrm{e}^{jkr} \qquad\qquad \frac{\partial U}{\partial n} = \left(jk - \frac{1}{r}\right)\mathrm{e}^{jkr}\cos(\vec{n},\vec{r})$$

the final Rayleigh–Sommerfeld relations are:

$$U_1(x,y,z) = \frac{1}{2\pi}\iint_{\mathcal{A}} \frac{\mathrm{e}^{jkr}}{r}\left(jk + \frac{1}{s}\right)\frac{\mathrm{e}^{jks}}{s}\cos(\vec{n},\vec{s})ds$$

$$U_2(x,y,z) = \frac{-1}{2\pi}\iint_{\mathcal{A}} \frac{\mathrm{e}^{jkr}}{r}\left(jk - \frac{1}{r}\right)\frac{\mathrm{e}^{jks}}{s}\cos(\vec{n},\vec{r})ds$$

The Rayleigh–Sommerfeld diffraction integral is believed to be more accurate the Fresnel–Kirchhoff formulation because of its mathematical consistency but also by its ability to reproduce closely the diffracted field just behind the aperture. However it has been experimentally shown [27][28][22] that Fresnel–Kirchhoff diffraction gives more accurate results than the Rayleigh–Sommerfeld theory (assuming that we are many wavelength away from the diffracting aperture) [25][26]. Moreover Rayleigh–Sommerfeld theory is limited to plane surfaces which is a strong limitation since we usually deal with curved surfaces in optics. On the contrary, Fresnel–Kirchhoff relation can handle surfaces of any shape [24][19].

Finally, if we restrict our study to large distances from the aperture ($k \gg \frac{1}{r}$) and to a normally incident plane wave illumination $U_1(x,y,z)$ and $U_2(x,y,z)$ reduce to:

$$U_1(x,y,z) = \frac{j}{\lambda}\iint_{\mathcal{A}} \frac{\mathrm{e}^{jkr}}{r}\frac{\mathrm{e}^{jks}}{s}\cos(\vec{n},\vec{s})ds \tag{3.14}$$

$$U_2(x,y,z) = -\frac{j}{\lambda}\iint_{\mathcal{A}} \frac{\mathrm{e}^{jkr}}{r}\frac{\mathrm{e}^{jks}}{s}\cos(\vec{n},\vec{r})ds \tag{3.15}$$

It seems obvious that considering small angles, the obliquity factor of previous relations are unity. In this very specific case the Fresnel–Kirchhoff and the two Rayleigh–Sommerfeld formulations are equivalent [19][11].

3.2.6 Fresnel diffraction

We have seen in eq.(3.15) of §3.2.5 that the first Rayleigh–Sommerfeld diffraction integral can be written:

$$U(P_0) = \frac{1}{j\lambda}\iint_{\mathcal{A}} U(P)\frac{\mathrm{e}^{jkr}}{r}\cos\theta ds \tag{3.16}$$

where θ is the angle defined by the normal $\vec{n}$ to the surface $\mathcal{A}$ and vector $\vec{r}$: Examining Fig. 3.4, it is obvious that $\cos\theta = \frac{z}{r}$. So without any approximation, the previous relation can be re–written:

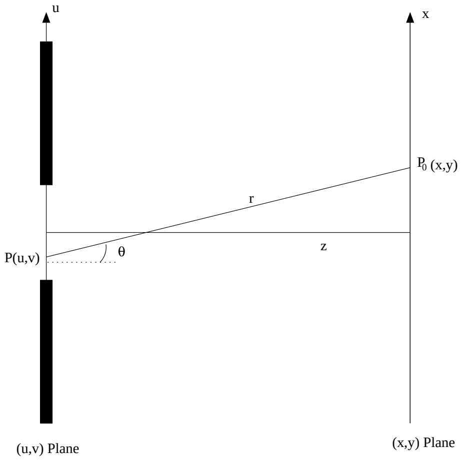

Figure 3.4: Fresnel diffraction setup.

$$U(P_0) = \frac{z}{j\lambda} \iint_{\mathcal{A}} U(P) \frac{\mathrm{e}^{jkr}}{r^2} du dv \tag{3.17}$$

The Rayleigh–Sommerfeld diffraction integral (3.15) was derived first assuming that the aperture dimensions are much larger than wavelength, then further restricting to a far observation plane from the aperture. In that particular case r distance can be approximated as following:

$$\begin{aligned} r &= \sqrt{(x-u)^2 + (y-v)^2 + z^2} \\ &= z\sqrt{1 + \left(\frac{x-u}{z}\right)^2 + \left(\frac{y-v}{z}\right)^2} \\ &= z\left(1 + \frac{1}{2}\left(\frac{x-u}{z}\right)^2 + \frac{1}{2}\left(\frac{y-v}{z}\right)^2\right) \end{aligned}$$

Reporting that approximation in the exponential part of eq.(3.17) and taking $r \approx z$ for the demoninator gives:

$$U(P_0) = \frac{z}{j\lambda} \iint_{\mathcal{A}} U(P) \frac{1}{z^2} \mathrm{e}^{jkz\left(1+\frac{1}{2}\left(\frac{x-u}{z}\right)^2+\frac{1}{2}\left(\frac{y-v}{z}\right)^2\right)} du dv \tag{3.18}$$

which gives the Fresnel diffraction formulation:

$$U(P_0) = \frac{\mathrm{e}^{jkz}}{jz\lambda} \iint_{\mathcal{A}} U(P) \mathrm{e}^{j\frac{k}{2z}\left((x-u)^2+(y-v)^2\right)} dudv \tag{3.19}$$

The previous equation can be developed as:

$$U(P_0) = \frac{\mathrm{e}^{jkz}}{jz\lambda} \mathrm{e}^{j\frac{k}{2z}(x^2+y^2)} \iint_{\mathcal{A}} \left[U(P)\mathrm{e}^{j\frac{k}{2z}(u^2+v^2)}\right] \mathrm{e}^{-j\frac{k}{2z}(ux+vy)} dudv \tag{3.20}$$

This highlights the fact that, according to the Fresnel diffraction theory, the optical disturbance at $Z = Z_0$ is basically the Fourier transform of the product of the optical distrubance $U(p)$ with a quadratic phase factor [19][11]. We will use that remark in section 3.4 to implement the Fresnel numerical propagator that we propose [29][30].

3.2.7 Fraunhofer diffraction

We have seen in the previous section that if the observation plane is far from the diffracting aperture, the diffracted field given by the Kirchhoff diffraction integral can be simplified to the Fresnel diffraction formulation [19][11]:

$$U(P_0) = \frac{\mathrm{e}^{jkz}}{jz\lambda} \mathrm{e}^{j\frac{k}{2z}(x^2+y^2)} \iint_{\mathcal{A}} \left[U(P)\mathrm{e}^{j\frac{k}{2z}(u^2+v^2)}\right] \mathrm{e}^{-j\frac{k}{2z}(ux+vy)} dudv \tag{3.21}$$

In the case of very far observation plane i.e. $z \gg \frac{k}{2}(u^2+v^2)$ the previous relation can be further simplied and leads to the Fraunhofer diffraction integral:

$$U(P_0) = \frac{\mathrm{e}^{jkz}}{jz\lambda} \mathrm{e}^{j\frac{k}{2z}(x^2+y^2)} \iint_{\mathcal{A}} U(P) \mathrm{e}^{-j\frac{k}{2z}(ux+vy)} dudv \tag{3.22}$$

In that case, the optical disturbance $U(P_0)$ in a plane far from the diffracting aperture can easily be determined by taking the Fourier transform of the complex transmittance of the diffracting aperture [31][32].

3.3 Numerical representation of diffracted fields

Until now all calculations involving optical disturbances or phase functions were performed using their analytical continuous mathematical representations. But due to the pixelated–oriented fabrication method of diffractive elements (see section 3.6), we have to sample those functions and adapt diffraction formulations of the previous section to the discrete case.

3.3.1 Sampling

Sampling a continuous function requires much more care as it could seem at the first glance. It is demonstrated in reference [19] that a function can be completely reconstructed from its samples provided the fact that sampling rate satisfies to the Nyquist theorem (see [32] p.189 and [19]). This theorem states that, considering a bandlimited function, sampling rate has to be at least twice the highest frequency present in the function to be able to recover all values between sampling points [32][29][33]:

$$\nu_{f_{Sampled}} \geqslant 2 \sup \left[\nu_{f_{BandLimited}}\right] \tag{3.23}$$

If this criterion is not satisfied, spectrum overlapping will appear when the sampled version of the function is Fourier–transform in frequency domain [32][19]. This phenomenon will be taken into account in chapter 5 when designing our diffractive elements.

3.3.2 The Fourier transform

In sections 3.2.6 and 3.2.7, we have seen that both Fresnel and Fraunhofer diffraction formulations rely on the Fourier transform. Since those formulations are, by far, the most intensively used in diffractive optics, we are going to briefly discuss a few points concerning the discrete Fourier transform. Discrete Fourier transform formulations are derived from their continuous case counterparts [32][31]:

$$\mathcal{F}(u) = \int_{-\infty}^{\infty} f(x) \mathrm{e}^{-2\pi j u x} dx \qquad \mathcal{F}(p) = \sum_{n=0}^{N-1} f(n) \mathrm{e}^{-2\pi j p \frac{n}{N}}$$

$$f(x) = \int_{-\infty}^{\infty} \mathcal{F}(u) \mathrm{e}^{+2\pi j u x} du \qquad f(n) = \frac{1}{N} \sum_{p=0}^{N-1} \mathcal{F}(p) \mathrm{e}^{+2\pi j n \frac{p}{N}}$$

The above formulations describe the one dimensional case only. Since diffractive optical elements are represented by two dimensional arrays, we have to first transform rows then columns.

3.3.2.1 Fast Fourier Transform

Since standard computer generated holograms are typically made of at least 1000×1000 cells, the Fourier transforming operation is very time consuming. For this reason we propose to restrict the array dimensions to a power of two; this allows the use of the very efficient *Fast Fourier Transform* (FFT)

[32][31][34][35] algorithm. In particular huge 4096 × 4096 matrices of complex numbers that we will use in chapter 5 were Fourier transformed using by one the various FFT implementations we propose: the ASM–SSE FFT algorithm. This implementation is based on the parallel–floating point instruction set of the Pentium III processor. This pretty efficient implementation was of great help when designing diffractive elements of chapter 5 since a 4096 × 4096 matrix is Fourier transformed in less than 6 seconds with a 600MHz computer.

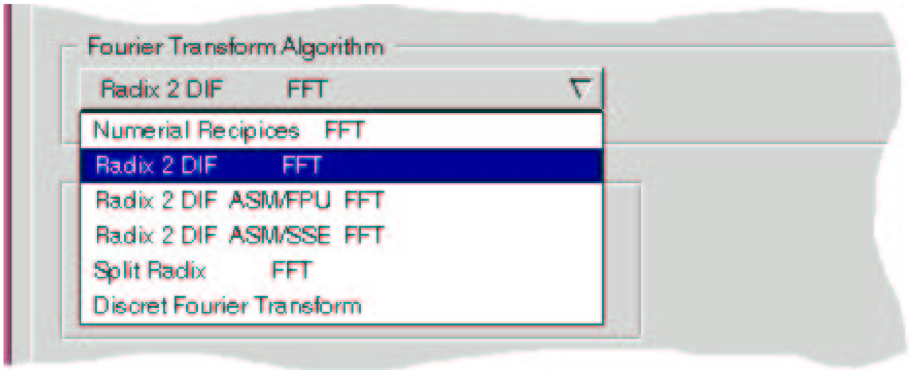

Figure 3.5: FFT algorithms implemented in the realized diffractive elements CAD software.

3.3.2.2 Dimensions

A little drawback of the FFT algorithm is that dimensions of frequency plane can not be freely chosen. Once the sampling interval Δx and the sample number N in the space coordinate plane are fixed, sampling interval in frequency plane $\Delta\nu$ is also fixed (see [32] p.362 and [29]) by:

$$\Delta\nu = \frac{1}{N\Delta x}$$

It is now worth remembering that in the Fraunhofer formulation of diffraction (see section 3.2.7) we had to write $u = v/\lambda f$ to exactly match the Fourier transform formulation. So in the case of Fraunhofer diffraction dimension p' of a square pixel in the image plane is [31][19][32]:

$$p' = \frac{\lambda f}{Np} \tag{3.24}$$

where λ is the wavelength, f the focal length of the Fourier transforming lens (see Fig. 4.9), p is the pixel size of our DOE and N the number of pixel along each direction (see [19] p.353).

3.3.2.3 Interpolation

We have seen above that an array of $N \times N$ pixels in the coordinate plane also gives an array of $N \times N$ pixels when FFT–transformed in the frequency plane. However it is often desirable to enhance either dimensions or accuracy of the frequency plane. There are two simple ways to do this with the FFT algorithm.

By embedding the $N \times N$ array in a larger one [31] (let's say $2N \times 2N$) is it obvious, taking a look at eq. (3.24), that the new pixel size p' is half the previous one, so accuracy is twice[32].

If, in the spatial coordinates plane, we oversample our $N \times N$ array by a factor of two, then dimensions in the frequency plane will also be twice.

Those methods will be intensively used in chapter 5 to carefully examine the reconstruction pattern of our computer generated holograms.

3.3.2.4 Applications of uncertainty principle

The Heisenberg's uncertainty principle of quantum mechanics states that the product of the uncertainty in position times the uncertainty of momentum must be greater than $h/2\pi$. We will see that, if we apply this fundamental relation to our case, it is then possible derive a relation of primary importance for our beam shaping problem.

3.3.2.4.1 Uncertainty principle Let's consider a time–dependent physical phenomenon represented by the mathematical function $f(t)$. Since $f(t)$ represents a physical phenomenon, it has an infinite number of derivatives. It is well know that the bandwidth–duration product of a signal can not be less than a minimum value. This comes from the interdependence of time and frequency variables that prevents arbitrary specification for both variables. If a signal if very brief it also must be wideband; on the contrary an ideal monochromatic wave must last forever. If we define the variance Δ_x of the function $f(x)$ as:

$$\Delta_x = \sqrt{\frac{\int_{-\infty}^{+\infty} x^2 |f(x)|^2 dx}{\int_{-\infty}^{+\infty} |f(x)|^2 dx}} \tag{3.25}$$

the previous statement can be given (see [32] p.160 and [36] p.30) a more mathematical form:

$$\Delta_x \Delta_u \geqslant \frac{1}{4\pi} \tag{3.26}$$

where Δ_x is the root–mean–square width of the function $f(x)$ and Δ_u is the r.m.s width of its Fourier–transformed $F(u)$. The inegality 3.26 is called *uncertainty principle of quantum mechanics.* The uncertainty principle is a constraint on the lower limit of the product of the r.m.s width of a function and its r.m.s bandwidth. This might appears pretty far from our concern but, from that principle we are going to derive a relation of primary importance for our beam shaping problem.

3.3.2.4.2 Space Band Width Product (SBWP) The direct application of Heisenberg's uncertainty relation (see 3.3.2.4.1) to signal processing leads to the very well known time–bandwith inequality. Similarly it is convenient, in diffractive optics, to define the Space Band Width Product. Let's consider a physically–realizable function f of a space coordinate x. Its associated Fourier transform in spatial–frequency domain is $F(u)$. Since we have chosen f to be physically–realizable both f and its transformed F are limited. This means that both f and F have significant values over a finite distance Δ_x (resp. Δ_u) and vanish anywhere else. The space bandwidth product (SBWP) of this function is then defined as (see [19] p.27):

$$SBWP = \Delta_x \Delta_u \tag{3.27}$$

In our case spatial–dimensions are the dimensions (e.i. height and width) of the DOE whereas spatial–frequency plane is the reconstruction plane. The SBWP product states that if we want infinitely sharp edges in the

The SBWP can be regarded as the number of degree of freedom of a function, it is also a measure of its complexity [19].

3.3.2.4.3 Beam shaping coefficient β We have seen from 3.3.2.4.1 that the uncertainty principle is a constraint on the lower limit of the product of the r.m.s width of a function and its r.m.s bandwidth $\Delta_x \Delta_u \geqslant \frac{1}{4\pi}$. If we restrict this general result to the problem of beam shaping we consider, it possible to derive a relation that reflects the quality of the beam shaper.

The field distribution in the focal plane of the Fourier–transform lens in given by [19]:

$$v = \frac{x'}{\lambda f}$$

where λ is the wavelength, f the focal length and x' the coordinate in the focal plane. Replacing this relation in the uncertainty principle gives [36][11]:

$$\frac{\Delta_x \Delta_{x'}}{\lambda f} \geqslant \frac{1}{4\pi}$$

Value of β parameter	Beam shaper quality
$\beta \leqslant 4$	Beam shaper will not produce acceptable result
$4 \leqslant \beta \leqslant 32$	Diffraction effects are significant
$\beta \geqslant 32$	good results

Table 3.1: Beam shaping β parameter

If we now convert width to Gaussian $1/e^2$ radius, the previous equation becomes [36] :

$$\beta = \frac{2\sqrt{2\pi} r_0 y_0}{\lambda f} \geqslant 0.69$$

where r_0 is the radius of the Gaussian input beam, y_0 the half–width of the shaped beam [36].

In section 3.2 we have derived mathematical diffraction formulations for various approximation levels. In the above sections, we have seen how to represent those diffracted fields taking into account the pixelated nature of phase only diffractive elements. In the next section we are going to bring together those concepts to derive computer algorithms that will make possible the numerical calculations of diffracted fields in various cases.

3.4 Proposed propagators

Preceding sections of that chapter were dedicate to the physics of diffraction and to the numerical representation of optical disturbances. So we now have all necessary tools for numerical calculations of optical disturbances diffracted by computer generated holograms. In that section we are going to focus on computer algorithms that allow numerical calculations of diffracted fields: propagators. We will see in section 3.5 that propagators are not only used for simulation of performances but also for the design of diffractive elements.

It would be tempting to use diffraction calculations algorithms available in commercial software package. Unfortunately, no actual commercial software can easily handle an arbitrary phase function $\varphi(x, y)$ as input data. Furthermore, neither a commercial software can take into account other requirements of DOE design like optimization constraints or phase quantization (see chapter 4.1). As a result, we had to develop our own computer software to be able to handle the full design of diffractive optical elements from specifications to generation of e–beam fabrication input files. We are going to present proposed functionalities of that software as we encounter the need for a specific task. We are alos going to introduce propagators we have implemented and briefly discuss their usefulness.

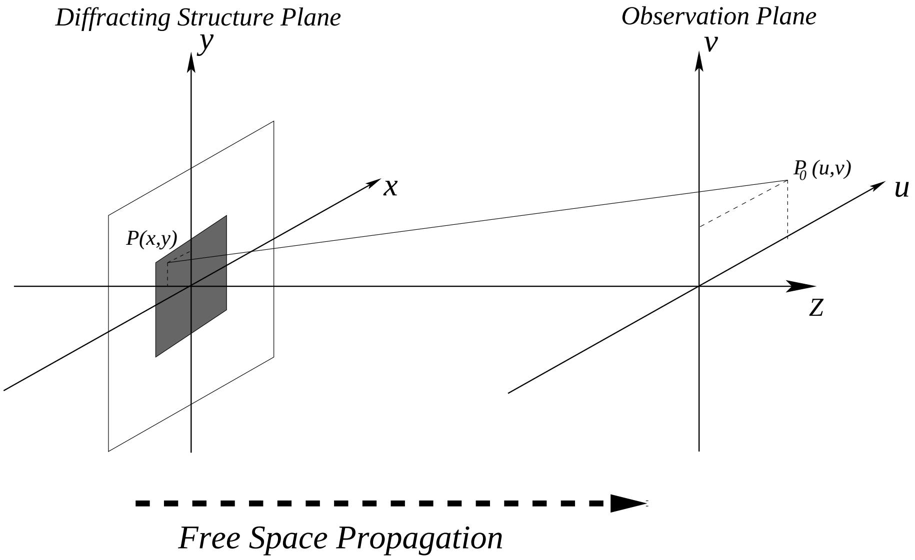

Figure 3.6: Free space propagation.

We will see in chapter 5 that the typical feature size of our DOEs is much longer than the illuminating wavelength. In that case, it has been demonstrated in section 3.2.2 that scalar diffraction theory is enough to give very accurate results [11][19]. So only scalar diffraction will be used. As a consequence, diffractive phase elements will be considered as thin phase plates and described with the complex amplitude notation.

We are now going to review all implemented versions of diffraction formulations presented in section 3.2. One question could arise: why implementing several propagators where one or two would be enough to design diffractive elements? The answer can be given considering two points. First, we will also have to simulate performances of our synthesized DOEs. This involve a thorough examination of the optical disturbance propagating from DOE plane to reconstruction plane. Depending on what you want to check (far field, depth of field, Speckle, . . .) one propagator will be used rather than another. Second, we have encoded a total of five different propagators to be able to validate them mutually. To validate an encoded propagator we use well known diffracting apertures like slits, half planes or lenses to check the calculated result. We also compare with resulst given by other propagators, if they are obviously too different then something went wrong in the implementation.

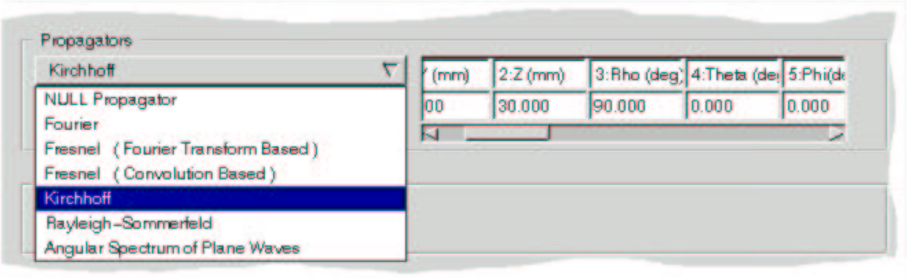

(mm)	2:Z (mm)	3:Rho (deg	4:Theta (de	5:Phi(d
00	30.000	90.000	0.000	0.000

Figure 3.7: Propagators implemented in the realized diffractive elements CAD software.

3.4.1 Angular spectrum of plane waves propagator

This formulation of diffraction, presented §3.2.3, is the most accurate method for evaluation of diffracted fields since it only relies on the scalar diffraction approximation. As seen on figure 3.8 even if the reconstruction plane is very close from the diffracting structure, the calculated diffraction pattern is still correct [19][11]. This method also has two strong advantages. It is first reversible that is, the inverse propagator can easily be derived from the direct one. Second, propagation of angular spectrum basically relies on Fourier transforms. So, by using FFT algorithm presented §3.3.2 computing time is low compared to other propagators [21]. Drawbacks of the method of angular spectrum were already mentioned in §3.2.3; we are restricted to parallel plane

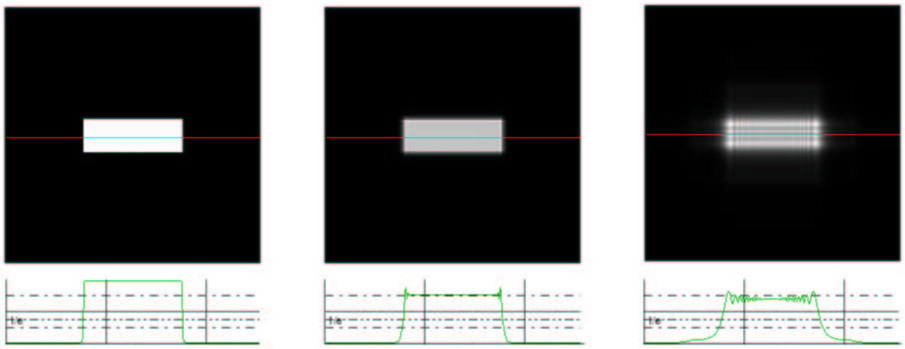
(a) (b) (c)

Figure 3.8: Simulated field amplitude behind an uniformly illuminated slit of dimensions 300μm$\times$100μm. Calculations were realized with the angular spectrum propagator at a distance: Z=10μm (a), Z=100μm (b) and Z=1mm (c) behind the slit.

surfaces [20][21]. Moreover if FFT is used, dimensions of the reconstructed plane are then automatically fixed (see section 3.3.2 and references [32][31]). We used this propagator to study the diffracted fields just behind the aperture but also for validation of other propagators like the Kirchhoff one which follows.

3.4.2 Kirchhoff propagator

The Kirchhoff formulation of diffraction is widely used in the design of diffractive optical elements as it gives invaluable information concerning the diffracted fields. Since no limitation on surfaces type are imposed by this formulation of diffraction, both diffracting and reconstructed surfaces can be curved, tilted or off–axis [25][24]. Dimensions of the reconstructed plane can also be freely chosen[5]. As the calculation of Kirchhoff integral does not rely on some kind of time–efficient FFT algorithm, it takes quite a long time to reconstruct the diffracted optical disturbance [25][24]. For this reason, the Kirchhoff propagator is particularly used for simulation of synthesized CGH rather than during the optimization process.

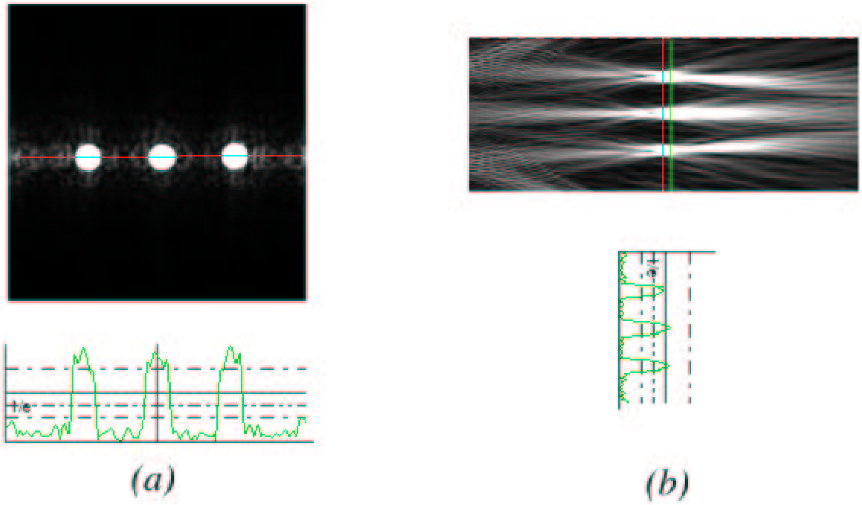

(a) (b)

Figure 3.9: Kirchhoff based calculations of diffracted fields along a plane perpendicular (a) and parallel (b) to the optical axis.

In chapter 5 we will consider the ability of that propagator to calculate the diffracted field along tilted surfaces to examine the depth of focus of

---

[5] The Nyquist sampling theorem has nevertheless to be satisfied.

our custom diffractive elements [26][37]. To validate this approach, we design a Fresnel spot array generator that reconstructs three spots at distance $Z = 10$mm of the diffracting aperture. Figure 3.9 shows calculations of reconstructed field in a plane located at $Z = 10$mm of the diffracting aperture and perpendicular to the axis on Fig. 3.9a and parallel to the axis (i.e. 90degrees tilted with respect to the normal of the axis) on Fig. 3.9b. The focusing and image forming effects in the reconstructed plane (dash line at $Z = 10$mm in Fig. 3.9b) are clearly seen. A closer investigation of Fig. 3.9b reveals a slight shift between the reconstructed plane (red line) and the $Z = 10$mm plane (green line). This is due to the fact that the energy redistributing function adds some focusing power to the quadratic lens phase function which has also been encoded in the DOE phase function.

When implementing this tricky diffraction formulation, we used angular spectrum propagator for near–field validation and Fourier diffraction for far–field validation associated to slit apertures or spherical lens phases. The implementation of the Kirchhoff formulation of diffraction (i.e. Kirchhoff propagator) is not only very accurate but also versatile [25]. Furthermore, in recent works more computing time–efficient variations of the Kirchhoff diffraction formulation have been introduced [24][37][21][38][39]. In chapter 5 the Kirchhoff propagator will be used intensively to analyze performances of DOEs we have realized.

3.4.3 Fresnel propagator

Propagators based on Kirchhoff, Rayleigh–Sommerfeld or angular spectrum diffraction integral are useful to get an accurate idea on what happens in a plane behind the diffracting structure. However, as those propagators involve time–consuming calculations, it is usually advantageous to use more time–efficient (although less accurate) propagators when synthesizing diffractive optical elements. This is particularly true when CGHs are designed with iterative methods (see §3.5 and §4.3.1) since they require many round trips between the diffractive aperture and the reconstructed plane.

The Fresnel formulation of diffraction we have presented in section 3.2.6 relies on the fact that observation plane is far (thousands of wavelength) from the diffracting aperture [11][19]. It was also demonstrated that the Fresnel diffraction integral can be seen as a special case of a Fourier transform (see eq. (3.20) page 33). For this reason, when intensive near–field calculations are required or when computing time is critical, it is advantageous to use the Fresnel integral evaluated with the Fourier transform. It is obvious that we will take part of the efficiency of the FFT algorithm (see §3.3.2) to realize the Fourier transform. Figure 3.10 represents the field diffracted by the spot

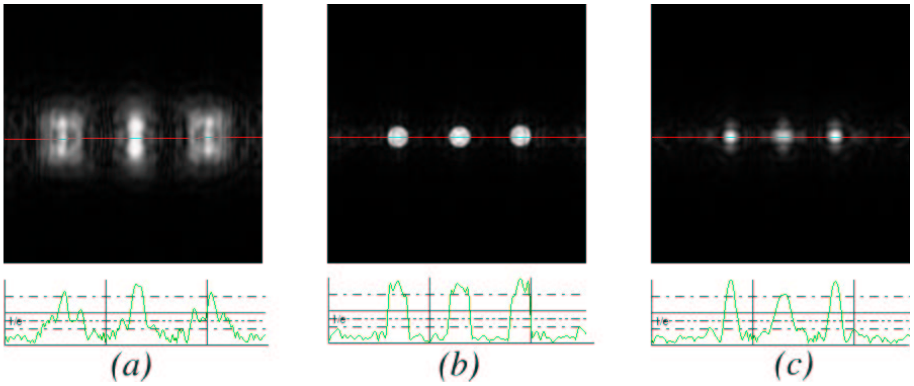

Figure 3.10: Evaluation of field diffracted by the phase function used in Fig. 3.9 with the Fresnel propagator. Reconstruction plane is located at: $Z = 9$mm (a), $Z = 10$mm (b) and $Z = 11$mm (c).

array generator described Fig. 3.9 of the previous section but, evaluated with the Fresnel propagator. Distances between diffracting aperture and evaluation plane are chosen to be: $Z = 9$mm (a), $Z = 10$mm (b) and $Z = 11$mm (c). Examining Fig. 3.9a and b, and Fig. 3.10a, b and c it is obvious that the overall patterns are the same when evaluated with Kirchhoff or Fresnel propagator. Tests realized with other apertures geometry and other phase functions also led to the same conclusion.

The Fresnel formulation of diffraction is very useful to get the optical disturbance in the near field of a diffracting aperture. Since FFT is the cornerstone of calculations, that propagator is very time–efficient and quite simple to implement. Moreover, the computing time efficiency can be further enhanced using the fractional Fourier transform [34][30][35][20]. However, it should be mentioned that this implementation of Fresnel diffraction formulation has severe drawbacks. That propagator can not handle tilted, off–axis neither curved reconstruction surfaces. Dimensions of the reconstructed surface are also limited by the use of the FFT algorithm.

3.4.4 Fourier propagator

Having a look at previous sections leads to a quite pragmatic statement: the simpler a diffraction formulation, the less versatile it is. This is illustrated with the case of Fraunhofer diffraction formulation exposed §3.2.7. In that formulation, the optical disturbance diffracted in the far field of an aperture is just the Fourier transform of the aperture complex transmittance function (see eq.(3.22)). It is obvious that we are also going to use the FFT algo-

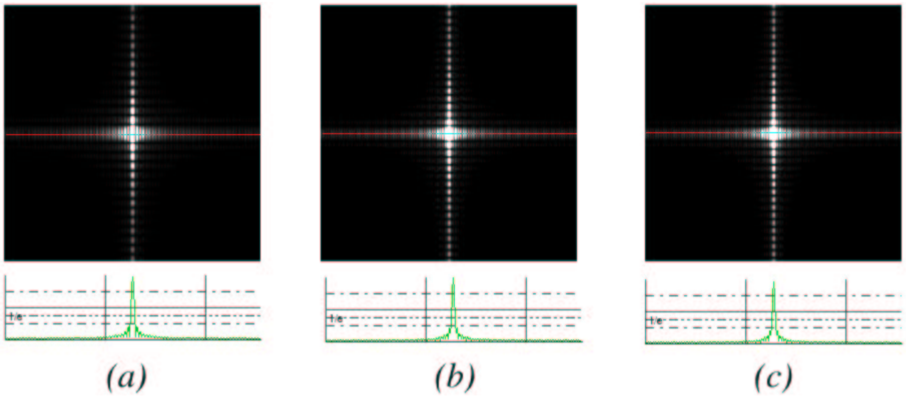

Figure 3.11: Optical disturbance in the far field of a uniformly illuminated slit evaluated with Kirchhoff propagator (a), Fresnel propagator(b) and Fraunhofer propagator (c).

rithm to realize the Fourier transform [32][31][37][34]. The immediate drawback of that extreme simplicity is no versatility at all. When the Fourier propagator is used there is no way to somehow control the geometry of the surface where diffracted optical disturbance is evaluated. Distance between diffracting aperture and observing plane is set to far field, dimensions of those surfaces are limiteds by the use of FFT algorithm [32] and all surfaces are limited to parallel planes.

Figure 3.11 represents optical disturbances in the far field of a uniformly illuminated rectangular slit evaluated with three different formulations of diffraction. As seen on this figure, the three diffracted patterns are the same provided the fact that each of the (a), (b) and (c) picture has its own scale. Having the correct sinus cardinal pattern with all propagators drives to the conclusion that far field calculations are exact with those propagators.

This ends sections dedicated to diffraction formulations and their numerical counterparts: propagators. Diffraction formulations were presented in previous sections because of the nature of our optical blood cells counting application which will rely on diffraction both for the generation of intensity distribution at the measurement point (see chapter 1) and for measuring various optical parameters associated to blood cells (see §2.3.2).

3.5 Design

In the previous section we have introduced numerical propagators which are the basement for computer calculations of optical disturbances generated by diffracting structures. So, now that we are able to evaluate the field generated by any diffracting structure, we have to deal with the much more critical inverse problem: what diffracting structure will give the desired diffracted pattern?

We first have to remind that we are only considering the case of phase diffractive elements (see §3.1) that is, kinoforms. In that case the diffracting structure is formed by surface reliefs that create a specific phase delay function $\varphi(x,y)$ at the diffracting aperture. So the DOE basically acts as a plate that modulates the phase of an incoming beam so that intensity distribution in some plane after the kinoform matches a desired pattern. To design a DOE, we have to determine a phase function $\varphi(x,y)$ that, under specific illumination conditions, will give a diffracting pattern as close as possible to the target one. In this section we are going to briefly review standard phase determination (or optimization) methods. Then we will only retain methods that are especially adapted to the design of our diffractive beam shaping problem presented in section 1.

3.5.1 Analytical methods

It sometimes happens, particularly in diffractive beam shaping applications, that requested intensity distribution in the image plane has a very simple geometrical shape like circle, rectangle or line [40]. In those cases target pattern can obviously be represented with a mathematical function. Furthermore, taking into account mathematical diffraction formulations presented in the previous section, and knowing the mathematical representation of incoming light distribution (a Gaussian function, for example); it is then sometimes possible to analytically derive a mathematical formulation of the DOE phase function $\varphi(x,y)$ [41]. It must be stressed that cases where both target pattern and input intensity are described by a mathematical function are very limited [42][43][44]. However, when analytical design is possible this design method is usually superior to other design methods [45][46].

Since the diffractive beam shaper that will be used in our optical blood cell counting setup typically meets requirements of analytical design, we will further detail this method in section 4.3.2 and we will propose prototypes of analytical beam shapers in chapter 5.

3.5.2 Numerical methods

Although it is sometimes possible to represent target patterns by an analytical mathematical function in beam shaping applications, it is seldom the case in all other applications of diffractive optics like image processing or display. When the phase function $\varphi(x, y)$ can not be analytically derived, numerical methods are then used. Those methods only rely on the numerical values of illumination intensity, phase distribution and target intensity functions at sampling points. At the end of the numerical optimization process we get a serie of $N \times N$ phase delay values each corresponding to a pixel in the DOE aperture. When this numerically determined DOE is illuminated with the right intensity distribution, we get a diffraction pattern close to the target one. Those numerical methods, that will be briefly exposed in the following sections, are based on complex–amplitude transmittance to describe the diffracting structure. This involves that scalar diffraction formulations (see 3.2.2) are used to determine the optical disturbance in the image plane.

3.5.2.0.4 Simulated Annealing The *simulated annealing* method analyses the effects of the change of one pixel of the phase function on the diffracted field [47]. Depending on whether the change improves the similarity with the target pattern or not, this change is accepted or refused. Since the effects of every pixel of the diffracting phase element is individually analyzed, computing time becomes extremely large when DOEs are composed of many pixels in their aperture [36]. Some kind of noise is also introduced in the algorithm so that convergence is not trapped to a local minimum. For that reason, the simulated annealing method is not sensitive to the starting parameters and is very good at avoiding stagnation to a local minimum during the optimization process [47][48]. The algorithm has converged when no pixel change is accepted.

The simulated annealing method is directly derived from the *Direct Binary Search* method [49], both manipulate pixels individually in the diffracting aperture [50][51]. It is worth noting that both simulated annealing and direct binary search only require forward propagator, this can be quite interesting in cases (like the Kirchhoff one) where back propagators are more than tricky to develop [19][11].

3.5.2.0.5 Iterative Method The *Iterative Fourier Transform Algorithm* (or IFTA) method was originally developed by Gerchberg & Saxton for electron–microsscopy [52]. The phase function of the diffracting structure is determined by performing loops between diffracting and image planes and, by replacing amplitude distribution in both planes by their target ones (see 4.5 p.60). Unlike simulated annealing, all pixels are modified at each loop in the iterative method. This is the reason why IFTA converges much more rapidly than other optimization strategy [53][54]. Furthermore, since all pixels are globally (and not individually) manipulated, iterative method is especially adapted to handle huge matrices of large diffracting elements. However the severe drawback of iterative design lies in the fact that one can not ensure the algorithm converges towards the global minimum [55]. That is, the determined solution for the phase function might not be the optimal one. Some other solutions with better performances probably exist. The final optimized phase also strongly depend on starting parameters. If those initial parameters are correctly chosen, IFTA performs as well as simulated annealing and much faster (see [50] p.313).

When iterative optimization is carefully used, it is one of the most efficient method to design diffractive beam shapers [40][55]. Some other algorithms like *Ping–Pong* [56] or *Yang–Gu* [57][58][59] are based on IFTA but slightly differ in the way constraints are applied in both planes.

3.5.2.0.6 Genetic Algorithm *Genetic Algorithm* depends on considerations that radically differ from what we have encountered until now [36]. Optimal solution for the phase function of the diffractive element is found by hybridization of a set of sub–optimal solutions. This method is analogous to the crossing over of chromosomes in biology. This optimization strategy is also very computational intensive, it is then limited to the determination of the phase of small diffractive elements.

3.5.3 Selected optimization methods

Having briefly reviewed standard methods for optimization of the phase of diffractive optical elements, it appears obvious that only two are adapted to the constraints of diffractive beam shapers and to high pixel number: the iterative method and the analytical design. Those two method were reported to be successful in various beam shaping configurations [54][60][55][40] [53][46][41]. For this reason, analytic beam shaping and iterative design of beam shapers will be thoroughly studied in chapter 4. Then both methods will be used in chapter 5 to design diffractive beam shapers that will be integrated in our optical blood cell counting setup.

3.6 Fabrication

Previous sections of this chapter were dedicated to the introduction of diffractive optical elements. We have studied the physics of diffraction by computer generated holograms in sections 3.2 and 3.4. Some methods to synthesize the diffracting structures were also presented in section 3.5. So, now we are able to calculate the diffractive structure that reconstructs a target intensity distribution in some plane after the DOE, the next step is to realize that diffractive structure and to test its performances.

At the beginning of that chapter we mentioned that among all types of diffractive elements, phase only diffractive elements (or kinoforms) give the best performances [50][14]. Phase diffractive elements are a thin plate of transparent material with surface reliefs on one side (see Fig. 3.12 and 3.1). Those surface reliefs add a phase modulation to the impinging beam and so modify the light distribution in some plane after the diffracting plane. Since the material is transparent, kinoforms have very good diffraction efficiency (usually $> 70\%$) [61][62]. Furthermore, by adjusting the maximal relief depth to a 2π phase delay, it is possible to redirect all the energy into the first diffraction order [14][19][50][51][63].

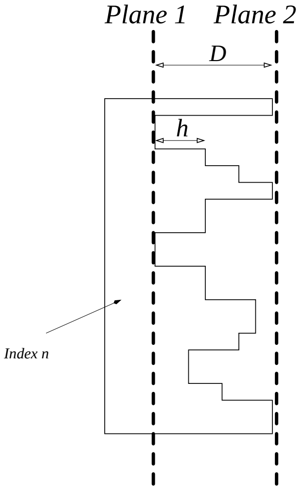

Figure 3.12: Schematic representation of surface reliefs of a phase only diffractive optical element: a kinoform.

Having determined the two dimensional phase function $\varphi(x, y)$ with methods presented in section 3.5, we are going to see how $\varphi(x, y)$ can be converted to a two dimensional depth function $h(x, y)$. Let's consider the setup depicted Fig. 3.12; a wavefront of wavelength λ located in the plane one (where the surface relief depth is h an index n) needs a time interval ΔT to travel to plane two:

$$\Delta T = \frac{h}{c/n} + \frac{D-h}{c} = \frac{h}{c}(n-1) + \frac{D}{c}$$

So the phase of that wavefront is changed of φ from plane one to plane two:

$$\varphi = 2\pi\frac{\Delta T}{T} = \frac{2\pi}{\lambda}C\Delta T = \frac{2\pi h(n-1)}{\lambda} + \frac{2\pi D}{\lambda}$$

The last term of the previous equation is constant and plays no role in the propagation of light, it can safely be omitted. So we have demonstrated that the phase modulation the incoming beam undergoes is proportional to the depth h of the surface relief. In case of variation of depth with location, that is $h = h(x, y)$, we get a two dimensional function for the phase modulation:

$$\varphi(x, y) = \frac{2\pi(n-1)}{\lambda}h(x, y) \tag{3.28}$$

So, the pixelated phase relief depicted Fig. 3.12 directly represents the pixelated phase distribution $\varphi(x, y)$ that was determined by methods described in section 3.5. Furthermore, since an addition or subtraction of 2π to the phase of an optical field has no effect, the phase function can be 2π–wrapped. Figure 3.13a represents the phase profile $\varphi(x)$ of a simple spherical positive lens, once 2π–wrapped one get the phase profile $\varphi_{2\pi}(x)$ represented on Fig. 3.13b. This 2π–wrapped phase function is then sampled with a period x_0 to get

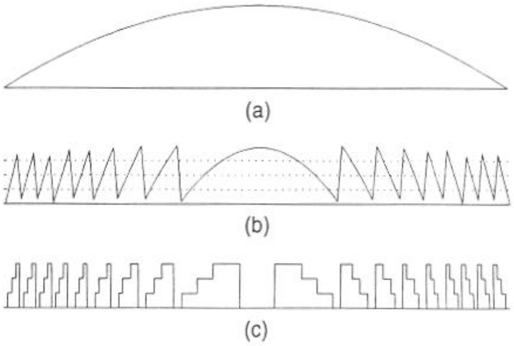

Figure 3.13: Representation of the phase profile of a positive spherical lens: full analog representation(a), 2π–wrapped analog representation(b) and 2π–wrapped and 4–step quantized representation(c).

the final pixelated phase function $\varphi_q = \varphi_{2\pi}(q \times x_0)$ with $q \in \mathbb{Z}$ depicted in Fig. 3.13c.

Sharps edges due to the modulo–2π representation of the phase function are characteristic for the diffractive structures and provide a challenge in the fabrication process. Moreover, the feature size of diffractive element used at visible wavelengths is usually ten wavelengths (about a few microns). As a result we will have to propose very specific fabrication methods to realize prototypes of the diffracting structures that were calculated in section 3.5. Once the diffractive optical element satisfies the target specifications, adapted mass–production fabrication methods have to be considered.

3.6.0.1 Prototyping

Historically, first diffraction gratings were fabricated by ruling engines: high precision mechanical devices that scribe grooves of a grating by ruling diamond. With the invention of diamond turning machines, rotationally symmetric diffractive elements (such as diffracting lenses) could be achieved. It is also possible to use two interfering beams for the production of gratings of various kind. But none of those methods can really take advantage of the versatility of diffractive optical elements. In the late 80's, it has been noted that microelectronics and diffractive optics have common demands: fabrication of micrometer features. So electron–beam (or e–beam) lithographic tools developed for microfabrication of semiconductor devices were adapted with a modified software and resist processing to realize diffractive optical elements with profile analogous to the one depicted Fig. 3.13c [61][62][63].

Electron–beam direct writing is the most sophisticated method for fabrication of diffractive optical elements. It can produce structures with dimensions below 50nm. Furthermore, analog profiles can be generated in a electron sensitive resist by controlling the electron dose per unit area, which eliminates masks alignments errors [64][50][61][62].

Through a collaboration with one of the world leading group in direct e–beam writing: the *Chalmers University of Technology*, Göteborg, Sweden. All prototypes we have designed (see chapter 5) were fabricated at Chalmers University of Technology. The available e–beam has allowed fabrication of diffractive elements made of 2048 × 2048 pixels with 64 phase quantization levels [65]. When those elements were tested, we measured a diffraction efficiency of more than 83% in the first order. This denotes an excellent fidelity between the target surface profile $h(x, y)$ and the realized one. Those fabrication considerations will be further discussed in chapter 5 where testing of all realized prototypes will be achieved.

3.6.0.2 Mass production

Fabrication methods presented in the above section were developed for prototyping purposes only. Cost and time that is necessary to realize a single prototype of DOE are not compatible with mass production for industrial use. Nevertheless, DOEs have excellent abilities for mass production with various replication methods [65][50][51]. Available replication technologies are represented on Fig. 3.14. The realization of a Nickel shim master is common to all replication methods.

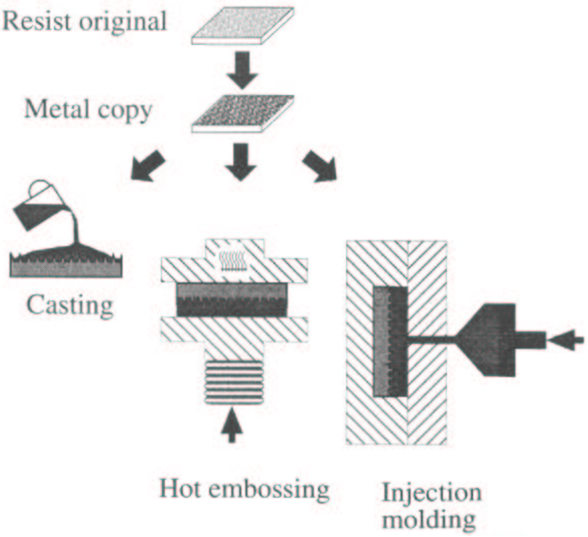

Figure 3.14: Nickel shim realization and replication technologies.

The fabrication of the Ni shim is based on an original structure realized by any of the prototyping methods exposed above. The original resist structure, which is non conducting, is first coated with a thin metallic layer of approximately 50nm. Then a nickel copy is realized by electroplating process. This gives a first generation shim (the master) that can be used to produce replica or other generation of masters.

Once the master is realized, several different replication methods can be used to replicate DOEs depending on desired quantities: UV–casting, hot embossing or injection molding.

3.6.0.2.1 UV-casting A UV–curable liquid (resin or epoxy) is used as replication material. This material is applied onto the Ni shim and exposed to UV radiations. After exposed, the curable material is solid and can be separated from the Ni shim. This method is especially adapted to small number of replica [50][51].

3.6.0.2.2 Hot embossing Using a hot press, the relief surface of the Ni shim can be replicated into a thermoplastic polymer (polycarbonate or

PMMA). This method is rather slow compared to other replication technologies [50][51].

3.6.0.2.3 Injection molding Injection molding is a well established technology for the high speed mass production of plastics components like compact disks. The Ni shim containing microstructures to be replicated is mounted on one side of the mold and pre–heated plastic is injected into the mold. After a rapid cool down, the molded part is extracted with a cycle time of less than five seconds [50][51][65].

The replication technology that will mass produce DOEs for our blood cell counting application has not been retained yet. Considering quantities (a few hundreds DOEs a year) and replica fidelity imposed by the beam shaping function sensitivity, we recommand to use injection molding.

3.7 Conclusion

In that chapter we have introduced a new technology, diffractive optics, that will be used in our blood cell counting application to both enhance measurement accuracy and lower production costs. Now that we are able to handle all processes involved in the design of DOEs (from specifications to fabrication of prototypes), we are going to focus in the next chapter on the optical function the proposed diffractive optical element will perform: beam shaping.

Chapter 4

Laser Beam Shaping

The goal we seek for throughout this work is to realize the uniform laser illumination for our blood cell counting application presented in chapter 1. In this section we are going to see that all problems of laser pattern generation are known as *beam shaping* problems. We are also going to see that very few optical technologies are available to solve the beam shaping problem at reasonable cost, and that diffractive optics introduced in the previous section is the most adapted technology to achieve this work.

4.1 Introduction

Beam shaping is the process of redistributing the irradiance and phase of an optical disturbance. The shape is defined by the irradiance distribution such as the uniform rectangular intensity distribution of our blood cell counting application. In the following sections, we are going to consider *lossless beam shaping* [66]. This means that incident energy is totally redistributed and not absorbed by the shaping optical device. Equivalently, this also means that the beam shaper has an efficiency close to 100%.

Generation of uniform illumination from a laser source is crucial for a wide range of applications like laser welding [18], laser–stimulated etching, laser scanning, laser microfabrication [67] or laser printing. This is the reason why laser beam shaping has become a subject of interest soon after the laser was discovered. The earliest known instance of lossless beam shaping was by Frieden in 1965 (see [66]). He used geometrical methods to determine the curvature of aspheric lenses that would reshape a single mode Gaussian beam into a beam with uniform profile. Since then, many authors have presented solutions based on either aspheric lenses or aspheric mirrors to correct badly shaped laser beams [16][17][68]. Those solutions usually give quite uniform shaped beams with an excellent efficiency like apsheric–lenses based beam shapers used microlithgraphy [67]. However, the typical drawback of those solutions is cost. Aspheric lenses are still difficult to produce and cost remain very high even in bulk quantities. This technology is obviously not adapted to our industrial environment neither to large quantities.

However it is worth to keep in mind that, in our particular case, the measurement point is defined by the intersection of the laser beam and the stream in which blood cells are flowing one after another. Since we know the geometrical limits in which blood cells are enclosed, it is possible for the laser illumination to fulfill some constraints inside those limits and to be arbitrary outside those limits. This is the basic concept of beam shapers actually used in all flow cytometers. As we are going to see, the main advantage of this setup is its simplicity since only spherical (or eventually cylindrical) lenses are used. But this setup also has the severe drawback of very low efficiency.

4.2 Refractive setup efficiency

The very first step to meet the uniformity constraint exposed in chapter 1 is the use of a combination of spherical and cylindrical lenses to enlarge the beam waist [69][36]. By enlarging the waist and restricting to the use of the central part of the beam, it is possible to satisfy to the first beam shaping condition: uniformity. So we are going to study light distribution in the plane of focus of the refractive beam shaper depicted Fig. 4.1. Since we are only considering optical setups based on TEM_{00} lasers and spherical (or eventually cylindrical) lenses, any beam cross–section has at least two axis of symmetry. For this reason we can safely restrict our analysis to the one–dimension case (see Fig. 4.2). Figure 4.2 shows the typical intensity profile of a 1–D Gaussian beam. This profile can be represented by the following

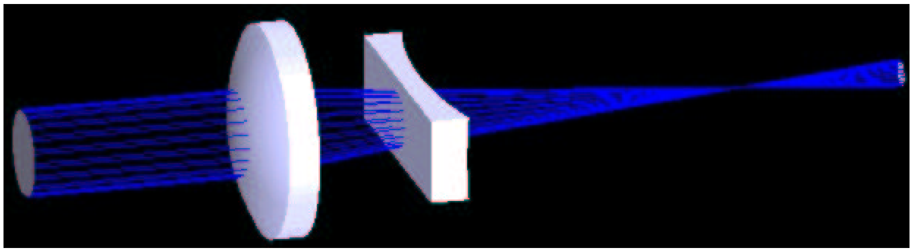

Figure 4.1: Optical setup for a very basic refractive beam shaper.

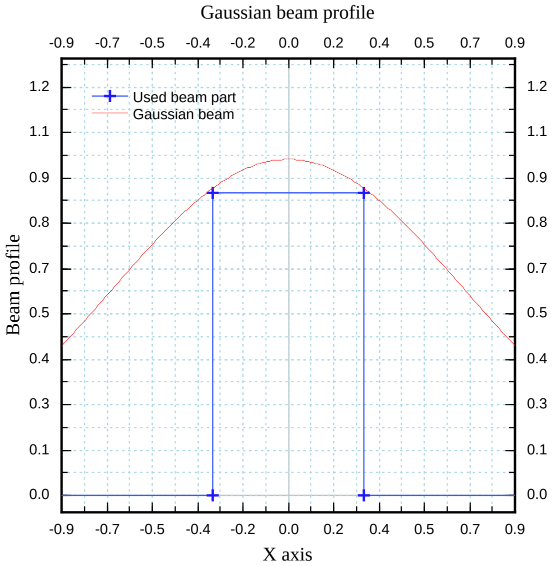

Figure 4.2: One–dimensional Gaussian beam profile.

normalized function:

$$I(x) = \mathrm{e}^{-2x^2/\sigma^2} \tag{4.1}$$

where σ is the beam waist at $1/e^2$. The total power under the normalized Gaussian function can easily be calculated by:

$$\begin{aligned} P_{total} &= \int_{-\infty}^{+\infty} I(t)dt \\ &= 2\int_{0}^{\infty} \mathrm{e}^{-2t^2/\sigma^2} dt \\ &= \sigma\sqrt{\frac{\pi}{2}} \end{aligned}$$

The refractive beam shaping trade–off implies that we only use the central part of the focused beam waist to satisfy to the uniformity constraint [69][36]. So to ensure that intensity variations are less than $n\%$ between $x = 0$ (i.e. the optical axis) and the limits $\pm x_n$ of the used part of the beam, x has to obey:

$$\frac{I(0)-I(x_n)}{I(0)} \leqslant \frac{n}{100} \qquad \text{with} \qquad n \in [0;100]$$

$$\Leftrightarrow$$

$$I(x_n) \geqslant 1 - \frac{n}{100}$$

So, we have intensity variations less than $n\%$ if x_n values are restricted to:

$$x_n \leqslant \sigma\sqrt{-\frac{1}{2}\ln\left(1-\frac{n}{100}\right)} \tag{4.2}$$

Examining Fig. 4.2 it is obvious that, even in the case of pretty bad uniformity (say variations of 10%), a very small part of the total beam is be used. That means a huge amount a power is lost since we have to restrict ourselves to the central part of the beam. To quantify the available amount of energy, we define the refractive beam shaper efficiency η_n as a function of desired uniformity n:

$$\eta_n = \frac{P(x_n)}{P_{total}} \qquad \text{where} \qquad P(x_n) = 2\int_0^{x_n} \mathrm{e}^{-2t^2/\sigma^2}\,dt \tag{4.3}$$

The quantity $\int_0^{x_n} \mathrm{e}^{-2t^2/\sigma^2}\,dt$ can't be evaluated directly. So we introduce the *Generalized Error Function* defined as:

$$\mathrm{Erf}\,(x) = \frac{2}{\sqrt{\pi}}\int_0^{x} \mathrm{e}^{-t^2}\,dt \tag{4.4}$$

If we change the variable of integration in the previous equation according to $t = \frac{\sqrt{2}}{\sigma}u$ we can re–write the integral $P(x_n)$ using the Erf function:

$$P(x_n) = 2\int_0^{x_n} \mathrm{e}^{-2t^2/\sigma^2}\,dt = \sigma\sqrt{\frac{\pi}{2}}\,\mathrm{Erf}\left(x_n\frac{\sqrt{2}}{\sigma}\right)$$

Reporting expressions of $P(x_n)$ and P_{total} = in Eq. 4.3, the efficiency η_n becomes:

$$\eta_n = \mathrm{Erf}\left(x_n\frac{\sqrt{2}}{\sigma}\right)$$

Finally replacing x_n by the relation we found in Eq. 4.2, the final formula of the efficiency of the refractive setup becomes:

$$\eta_n = \mathrm{Erf}\left(\sqrt{\ln\frac{100}{100-n}}\right) \tag{4.5}$$

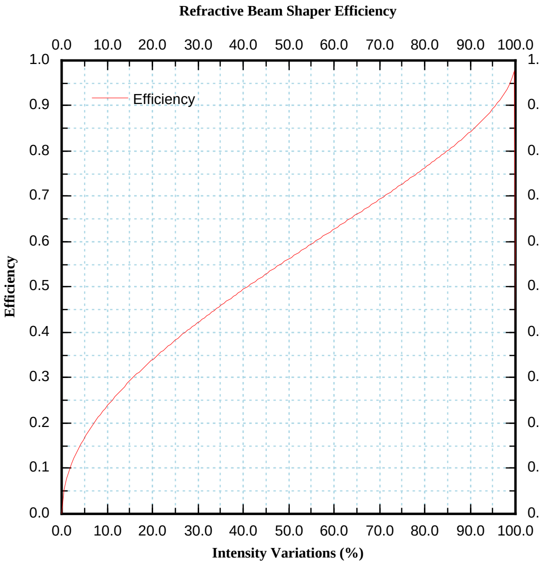

Figure 4.3: Refractive beam shaper efficiency.

Let's consider that we want the uniformity to be less than 10%; this involves that the efficiency η_{10} is less than 24%.

As one might have expected, the final formulation for the efficiency η_n does not depend on beam waist σ. This was easily predictable since the more we enlarge the waist, the more uniform it becomes, and the more x_n boundary value increases. On the contrary if the waist is reduced, the x_n boundary value is also reduced.

It also has to be noticed that a Gaussian laser beam can, of course, not be truncated by the use a rectangular diaphragm. This would inevitably lead to a strong and unwanted diffraction pattern in any image plane.

One should notice that the previous setup is more a beam expander than a real beam shaper. Relation between input and output beams is a scale factor only. The Gaussian profile of the beam is left unchanged. Anyway, this setup can be advantageous for cost–sensitive applications since it only relies on two cheap plano–spherical or plano–cylindrical lenses. It is nevertheless possible to design a real refractive beam shaper that transforms a Gaussian profile into a uniform one [36][70][71]. But this requires lenses with very complex aspheric surfaces (see [69][72]) that are very difficult to produce in bulk quantities. Examples of other refractive or reflective beam shaping devices are given in references [73][74][75][69][72].

4.3 Diffractive beam shapers

In the previous section we have seen that typical refractive beam shapers are either based on high cost aspheric surfaces [69][72][74] that give good efficiency or based on cheap classical spherical surfaces that lead to a very low efficiency. Since it seems impossible to satisfy to the low cost versus high efficiency constraint with classical optical elements, it might be wise to consider the use of Diffractive Optical Elements.

We have seen in section 3.1 that diffractive optical elements are basically wave forming elements that have high diffraction efficiency (about 85%). Diffractive optics is then the ideal technology to solve our beam shaping problem.

Designing a DOE is pretty different from designing a refractive optical system. It is not possible to "pick up" elements in a catalog and combine them to get the desired optical function. Purpose of a DOE has a significant impact on its design that it is impossible to consider multi purpose diffractive elements. Any DOE has to be custom–designed to fulfill constraints of the application. Moreover no commercial software package actually exist to design applied diffractive elements. For instance, neither Code–V nor Zemax can handle the full process of designing a DOE from the definition of constraints to final fabrication data file. For this reason we are going to present the algorithms we had to encode to achieve the goal of synthesizing and fabricating a beam shaping diffractive element adapted to our blood cell counting application.

We have previously mentioned in chapter 3 that DOEs can be synthesized either using non linear optimization loops or using direct analytical determination. Both methods have its advantages and drawbacks and, as we will see in chapter 5, they can sometimes be combined to give excellent results. So we are first going to propose an iterative algorithm for determination of the phase function of a beam shaping diffractive element. Then we will introduce a direct analytical method to determine this phase function.

4.3.1 Proposed iterative design

We have seen in section §3.5 that many algorithms are available [76] to optimize the phase function of diffractive phase optical elements: Direct Binary Search [49], simulated annealing [47][77] and genetic algorithm [76]. In this section we are going to propose our optimization strategies that is especially efficient for our beam shaping problem: iterative optimization algorithm.

4.3.1.1 Presentation

Iterative algorithms have prove, their utility in many scientific applications like electron–beam microscopy, astronomy, wavefront sensing, cristallography and optics. When mathematics fail in determining analytical solutions, it is often advantageous to solve a problem with an iterative method. A typical problem arises when we want the Fourier transform of an object (signal, aperture, antenna array) to have certain properties (such as uniform spectrum) while the object itself must satisfy some other constraints. Furthermore, information are sometimes missing or incomplete in each domain.

4.3.1.2 Iterative Algorithm

The Gerchberg–Saxton [52] algorithm, that we are going to implement was originally developed to solve a problem of electron–microscopy. In this case both modulus of complex valued imaged and modulus of its Fourier transform are measured and the goal is to reconstruct the phase in both domains. This problem of electron–microscopy exactly matches our needs in diffractive optics where the two domains, spatial–coordinates in DOE plane and spatial–frequencies in the reconstruction plane, are linked with a Fourier transform–based[1] relation. Considering the setup depicted Fig. 4.4, it is obvious that the input field $\tilde{u}(x,y) = |\tilde{u}(x,y)|\, \mathrm{e}^{j\varphi(x,y)}$ at the DOE plane and the output

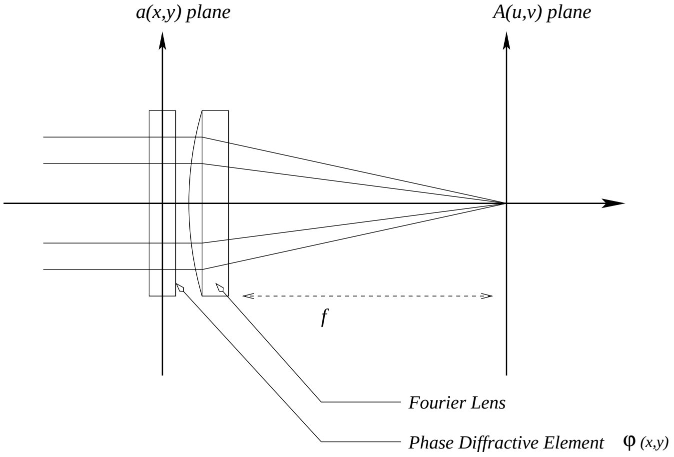

Figure 4.4: Iterative algorithm Fourier setup.

---

[1] the validity of the presented algorithm still remains in case of more complex relations between the two planes. For simplicity reasons, we are going to consider a pure Fourier transform in this presentation.

field $\tilde{U}(u,v) = \left|\tilde{U}(u,v)\right| \mathrm{e}^{j\Phi(u,v)}$ in the focal plane make a Fourier transform pair. In this case intensity is known in both planes (input laser beam and output reconstructed pattern) but phase distribution $\varphi(x,y)$ in the DOE plane is to be determined. So the problem can be summarized in finding a Fourier transform pair that satisfies a set of constraints in both planes.

Iterative optimization is based on complex amplitude representation[2] of optical disturbances. Amplitude $u(x,y)$ of the optical disturbance in the DOE plane is given by the square root (see Fig. 4.5) of the incoming laser distribution $i_{Laser}(x,y)$. In the reconstruction plane, amplitude distribution $U(u,v)$ should be as close as possible to the square root of the desired intensity pattern $I_{Pattern}(u,v)$. The Fourier transform relation between the two domains involves a remark concerning the bandwidth of considered func-

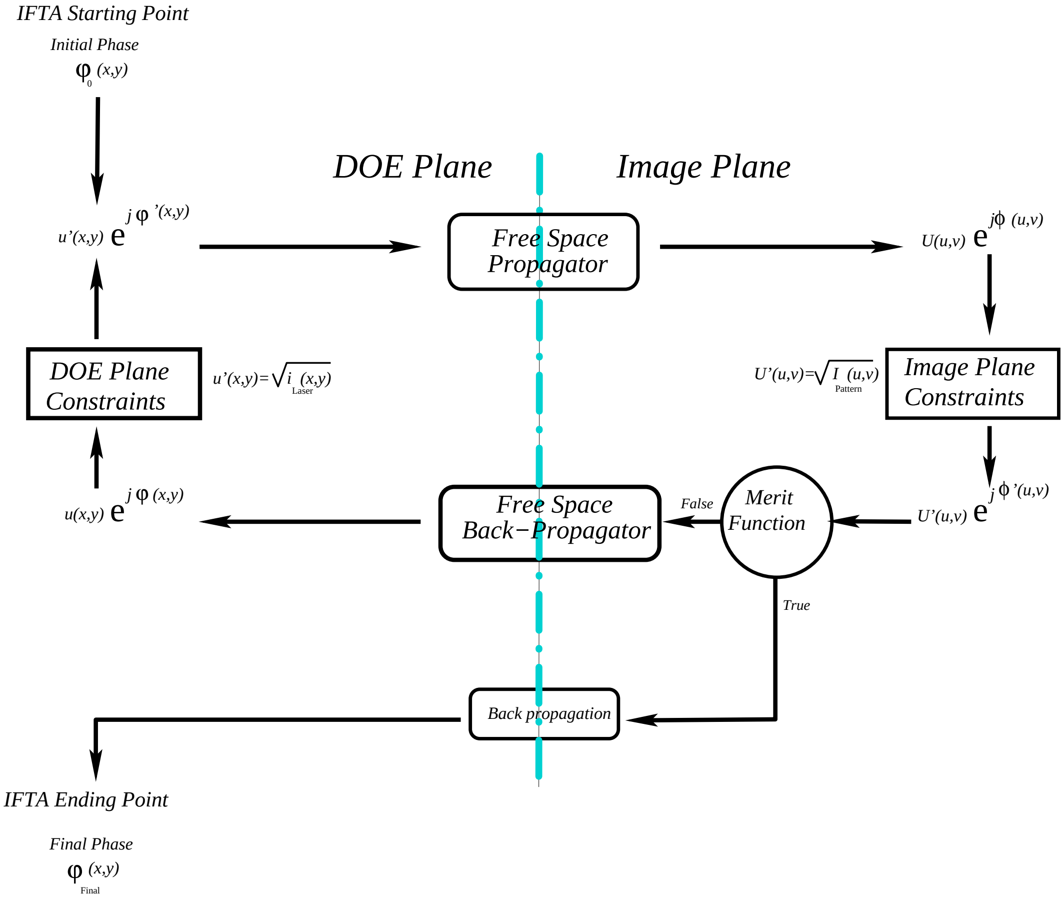

Figure 4.5: Proposed iterative optimization algorithm diagram.

---

[2] That is, geometrical optics approximation.

tions. Let's consider an amplitude distribution with very sharp variations (say a step or Dirac function) in the image plane. This infinitely sharp function in the image plane must have an inverse Fourier transform function in the DOE plane with infinite aperture dimensions. So, in the real case, the finite aperture dimensions of the DOE only allow reconstructed of bandlimited intensity distributions $U_{Pattern}(u, v)$ in the image plane [78][54]. To be very accurate it is to be said that iterative optimization algorithm can, in some cases, reconstruct very high spatial frequencies in the image plane although dimensions of the aperture are finite. During the optimization loop the algorithm can take part of spectrum overlapping to generate high spatial frequencies. This is usually undesirable since it leads to strong Speckle noise in the reconstruction plane.

Propagators used to go back and forth between the two planes are usually based on the Fourier transform, for this reason iterative optimization algorithm is often called *Iterative Fourier Transform Algorithm* or simply IFTA.

Figure 4.5 represents the proposed loop of the iterative optimization algorithm, keeping in mind that we want to determine the phase function $\varphi(x, y)$ of a Fourier transform pair that has to satisfy some constraints in both domains. The algorithm starts with an initial guess $\varphi_0(x, y)$ of the function $\varphi(x, y)$ which is often chosen to be random. As we are going to see below, the choice of the initial phase φ_0 is of primary importance for the quality of the final result. In the DOE plane, the amplitude $u(x, y) = |\tilde{u}(x, y)|$ of our complex function $\tilde{u}(x, y) = u(x, y)\mathrm{e}^{j\varphi(x,y)}$ is, of course, the amplitude of the input laser. That is, the square root of the laser intensity distribution $u(x, y) = \sqrt{i_{Laser}(x, y)}$. The complex optical disturbance $\tilde{u}(x, y)$ is then propagated from DOE plane to the image plane in which the optical disturbance is $\tilde{U}(u, v) = U(u, v)\mathrm{e}^{j\Phi(u,v)}$ with $\left(U(u, v) = \left|\tilde{U}(u, v)\right|\right)$. Since the initial phase distribution $\varphi_0(x, y)$ was chosen random, there is no chance that $U(u, v)^2$ matches the desired output pattern $I_{Pattern}(u, v)$. So the amplitude distribution $U(u, v)$ is replaced by the desired amplitude $U'(u, v) = \sqrt{I_{Pattern}(u, v)}$ whereas the phase distribution $\Phi(u, v)$ is left unchanged. This is the image plane constraint (see Fig. 4.5). The new complex optical disturbance $\tilde{U'}(u, v) = U'(u, v)\mathrm{e}^{j\Phi(u,v)}$ is then propagated back from image plane to DOE plane. Since $U(u, v)$ has been modified in image plane, the modulus $u(x, y)$ of its back–transformed function probably doesn't match $\sqrt{i_{Laser}(x, y)}$ anymore. So $u(x, y)$ distribution is replaced with $u'(x, y) = \sqrt{i_{Laser}(x, y)}$ (DOE plane constraint). We have then performed a whole loop since we are back to the starting point. By performing iterations and applying specifics constraints in both domains,

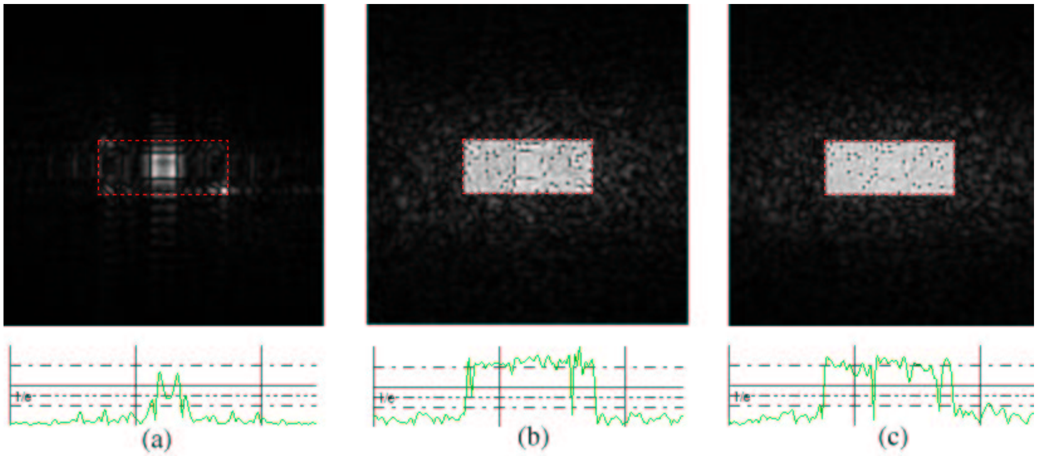

Figure 4.6: Evolution of reconstructed light intensity pattern (upper row) for N=1(a), N=10(b) and N=50(c) iterations. Lower row shows one amplitude profile across the reconstructed plane.

the reconstructed amplitude $U(u,v)$ become closer and closer to the target $\sqrt{I_{Pattern}(u,v)}$ distribution. The question arises: when to stop?

4.3.1.3 Merit function

It seems obvious that we need to quantify how the amplitude distribution $U(u,v)$ matches the desired distribution $\sqrt{I_{Pattern}(u,v)}$. We will then be able to set a threshold beyond which there is no need to perform any optimization loop anymore. for that reason we introduce a *merit function* that will quantify a parameter like diffraction efficiency, reconstruction error or uniformity. Merit functions are evaluated in DOE or image plane depending on the measured parameter. Let's say we want the reconstruction error to be less than 10%. Anytime the loop is in the image plane the reconstruction error [79][50][51] will be evaluated. If it is more than 10% nothing will happen. But if the error is less than 10%, $U(u,v)$ will not be applied constraints anymore but back propagated a last time to the DOE plane. Optimization is then over and the phase distribution $\varphi(x,y)$ is the one we were looking for to solve our Fourier transform pair problem.

One might wonder if $U(u,v)$ distribution really get closer to $\sqrt{I_{Pattern}(u,v)}$ when performing IFTA loops. That is, what ensure that this optimization strategy converges? The answer is given in [80] p.195 and [52] where it is demonstrated that similarity between $U(u,v)$ and $\sqrt{I_{Pattern}(u,v)}$ can only increase from one optimization loop to the next one.

4.3.1.4 Speckle and phase dislocations

In section 3.3.1 we have stressed the importance of phase function $\Phi(u,v)$ in the reconstruction plane. There is a direct relation between smoothness of $\Phi(u,v)$ and fluctuations of $U(u,v)$ sampling points [81]. If $\Phi(u,v)$ is smooth, the amplitude distribution $U(u,v)$ will be stable between sampling points; whereas if $\Phi(u,v)$ has discontinuities (or dislocations) $U(u,v)$ will vary a lot between sampling points (see [54][78][82]). Since beam shaping require the best uniformity in the image plane, that means phase has to be carefully controlled to get a smooth $\Phi(u,v)$ function and then ensures that no Speckle arises between sampling points. Our design problem becomes even more difficult since the phase function $\Phi(u,v)$ can not be used as a free parameter when designing laser beam shapers.

4.3.1.5 Initial phase

It is now obvious that the random function taken as initial guess φ_0 for phase $\varphi(x,y)$ leads to a strong Speckle noise in the image plane. Since random function has both high frequencies and many discontinuities, it tends to generate a $\Phi(u,v)$ distribution with the same discontinuities; moreover IFTA optimization is unable to remove those discontinuities in the image plane (see [83]). For that reason it is highly desirable to find an initial function $\varphi_0(x,y)$ with no discontinuities. It has also been demonstrated in [83] that initial phase has a huge impact in IFTA optimized DOEs (Fig. 4.7). Random and smoothed random phases tend to redistribute the energy uniformly into the whole DOE window, which is desirable, but also contain discontinuities that will remain in the whole optimization loop and give Speckle noise. If the initial phase is chosen to be constant, the energy will be located mainly in the center of the aperture and will slow down the converge rate of IFTA but will introduce much less Speckle. The quadratic phase function of a positive lens is a good compromise between convergence rate and Speckle. Since the function is defined analytically by $\varphi_0(x,y) = \frac{\pi}{\lambda f}(x^2+y^2)$, it is smooth over the whole DOE aperture. More over energy can be accurately redistributed over the plane by adjusting the focal length in the lens equation. As seen in Fig. 4.7 the reconstruction plane of an IFTA optimized DOE started with a quadratic phase contains almost no Speckle since the phase function $\Phi(u,v)$ in the image plane is smooth.

4.3.1.6 Constraints

We have seen above that because IFTA optimization strategy can not remove phase dislocations, it is important to introduce as few phase discontinuities

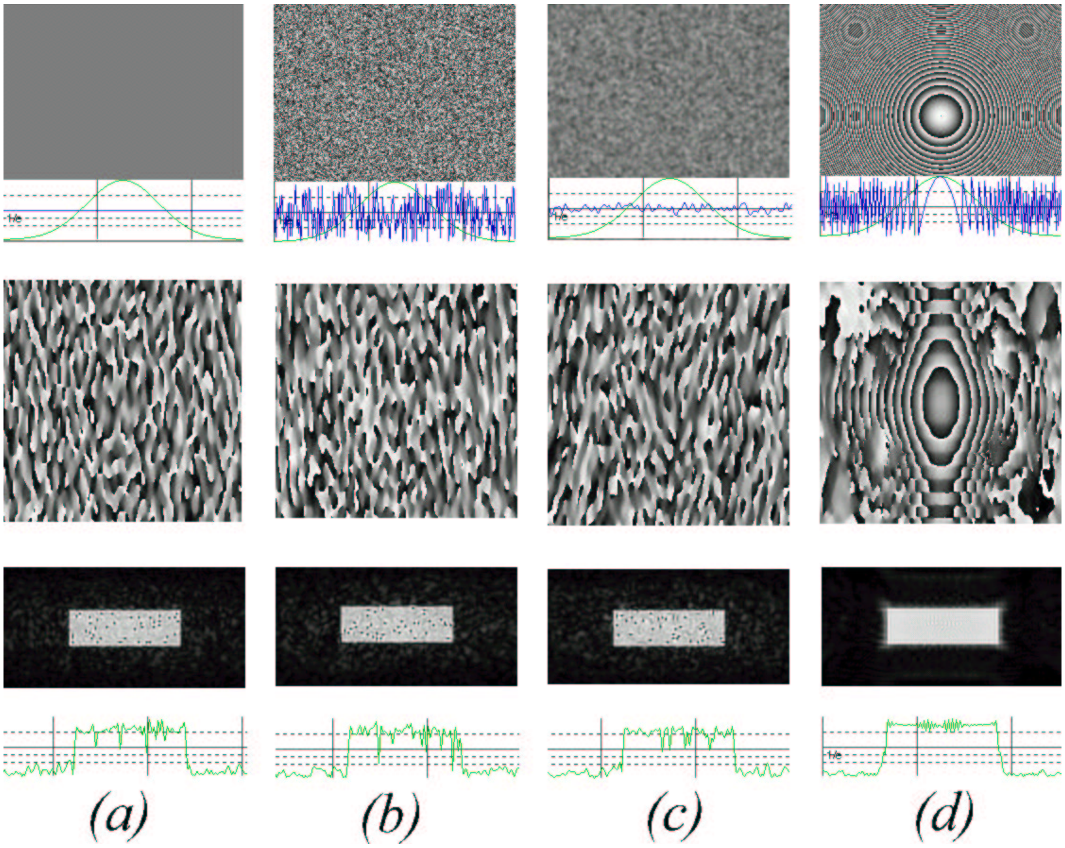

Figure 4.7: Initial phase distributions $\varphi_0(x,y)$ (upper row) and their associated final amplitude distributions $U(u,v)$ in image plane (lower row). Chosen initial phase distributions are: constant (a), random(b), smoothed random(c) and quadratic(d).

as possible in the initial guess of the phase distribution. But although we have taken care not to introduce any dislocations in the initial phase, those discontinuities sometimes occur during the optimization process. As shown in figure 4.5, constraints applied in both planes are total replacement of the function amplitude distribution by the target amplitude distribution in the whole plane. This constraint is pretty hard since it can produce big differences between $\tilde{u}(x,y)$ and $\tilde{u'}(x,y)$ (and also between $\tilde{U}(u,v)$ and $\tilde{U'}(u,v)$): continuity in the optimization process is broken and phase dislocations appear. For that reason it is desirable to find some less severe constraints that ensure continuity of our Fourier transform pair from one iteration to the next one. There are two different methods to somehow relax constraints applied in each domain; it is possible to apply a constraint locally and it is also possible to apply it partially only.

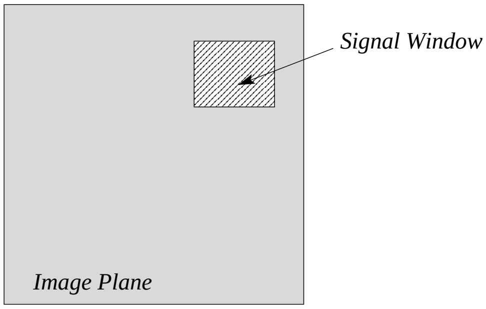

Figure 4.8: Constraint can be apply in an area smaller than the image plane: the signal window.

As depicted Fig. 4.8, the desired reconstructed pattern usually fills only a small region of the image plane defined as signal window. Moreover light distribution out of the signal window is of no interest in many applications. It has been demonstrated [60][83][54] that replacing amplitude by target amplitude in signal window only minimizes modifications applied to $\tilde{U}(u,v)$ function and then leads to a more progressive and smoother optimization. It is also important to note that since the constraint is applied in signal window only and since the rest of the image plane is left unchanged, more degrees of freedom are available for optimization. For this reason image reconstruction errors are usually reduced when a local constraint is used. A drawback of this method is the lower diffraction efficiency it gives. Since the amplitude out of the signal window is left arbitrary, IFTA doesn't try to optimize it to the detriment of signal window amplitude.

Another way to somehow relax constraints in both domains is to apply them partially. This means that, rather than abruptly replacing amplitude with target amplitude, we introduce a *running parameter* α that will ensure progressivity in replacement of amplitude in both planes. Assuming that parameter values are ranging from zero at the beginning of the optimization to one at the end. It is possible to give a more mathematical form to this constraint:

$$u_{n+1}(x,y) = (1-\alpha)u_n(x,y) + \alpha\sqrt{i_{Laser}(x,y)} \tag{4.6}$$

$$U_{n+1}(u,v) = (1-\alpha)U_n(u,v) + \alpha\sqrt{I_{Pattern}(u,v)} \tag{4.7}$$

The running parameter α is used to control the progressivity (i.e. continuity) of the optimization procedure. At the beginning of the optimization $\alpha = 0$ so no change is made in the Fourier transform pair $\left(\tilde{u}(x,y);\tilde{U}(u,v)\right)$. By slightly increasing α, we introduce very little changes that tend to converge to the target pattern without breaking the continuity between iterations of $\tilde{u}$ and $\tilde{U}$ functions. At the end of the optimization $\alpha = 1$ ensures that there are very few differences between the reconstructed pattern and the target pattern. Diffractive optical elements optimized with those constraints typically give excellent reconstruction accuracy and low Speckle noise [80].

Those two methods are not exclusive one with another, this means that a constraint that is both progressive and local can be apply. This method was successfully tested to design Speckle–free diffractive elements [53][83][80].

4.3.1.7 Conclusion

We have seen that iterative optimization is a powerful tool to achieving good compromise between high diffraction efficiency and high SNR [82][83]. It is also a versatile strategy since it allows the use of various free space propagators[3] to go back and forth between the two planes. Moreover, applied constraints are unlimited and can help to solve problems as various as quantization of phase function [60][84] or e–beam point spread function compensation [85][65].

It is also important to note that both input and output intensity distributions can be almost completely freely chosen (unlike analytical method see §4.3.2). Input intensity can be Gaussian, uniform, or arbitrary like the output of a preceding diffractive element. Output intensity can represent continuous geometrical patterns, discrete spots, or even pictures.

However, a drawback of iterative optimization is that it can not ensure a global minimum but only local minima. So when the algorithm is stopped because the merit function has reached the threshold, the determined phase profile is not unique. Other solutions exist depending on initial conditions or applied constraints [52][53].

4.3.2 Analytical design of diffractive beam shapers

We have seen in §4.3.1 that iterative methods can be used to determine the phase distribution $\varphi(x, y)$ of a diffractive beam shaper. This method gives quite satisfying results since it is possible to realize DOEs that shape the Gaussian input beam into a rectangle of desired dimensions with sharp edges [75][51].

Nevertheless, iterative methods generally tend to produce phase dislocations (i.e. π phase jumps) in the reconstruction plane [81][86][78][83][84].

---

[3] Based on complex amplitude transmittance.

Those dislocations are responsible for the strong Speckle effect that dramatically lowers intensity distribution uniformity [87][81][88]. Moreover, we have also seen that DOEs optimized with iterative methods are very sensitive to beam misalignments and variations of input beam amplitude distribution [89][80][53][60][54][90]. Then it might be wise to find a smoother phase distribution $\varphi(x, y)$. We would like to find an infinitely derivable phase function that, when multiplied with the input beam amplitude function $a(x, y)$ and Fourier–transformed according to the setup Fig. 4.9 gives the desired amplitude $A(u, v)$ in the reconstruction plane.

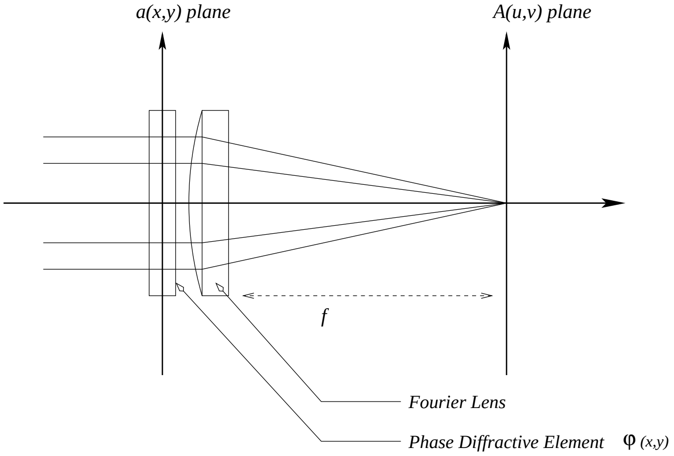

Figure 4.9: Analytical beam shaping Fourier setup.

Since the chosen phase function $\varphi(x, y)$ and the Gaussian laser beam amplitude $a(x, y)$ are infinitely differentiable, one might expect $A(u, v)$ and $\Phi(u, v)$ to be infinitely differentiable too. For this reason there should be no phase dislocations (a much reduced Speckle) in the reconstruction plane, that is, a better intensity uniformity.

4.3.2.1 Fourier setup case

The goal is now to determine analytically the unknown function $\varphi(x, y)$ that realizes the desired amplitude transformation when inserted in the optical setup depicted Fig. 4.9. Determining analytically the phase function of a DOE is not always possible. It has already been done [45][46][43][91][44][41] for simple input beam profiles and reconstructed patterns such as lines, circles, rectangles, … The desired transformation is a re–mapping of a plane into another plane, it is a one–to–one transformation. Any point in the (x, y) plane will be imaged in the (u, v) plane at location $(u(x, y); v(x, y))$. We have

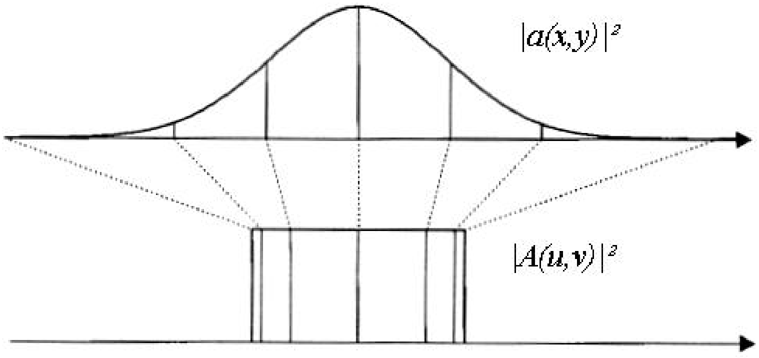

Figure 4.10: Redistribution of a Gaussian beam profile to a uniform one.

seen in §3.2.7 that the relation between the two planes of the setup depicted Fig. 4.9 is basically a Fourier transform [19][46][43]:

$$\tilde{A}(u,v) = \iint_{-\infty}^{+\infty} \left[a(x,y)\mathrm{e}^{j\varphi(x,y)}\right] \mathrm{e}^{-j\frac{2\pi}{\lambda f}(ux+vy)} dxdy \tag{4.8}$$

where $\tilde{A}(u,v) = |A(u,v)|\,\mathrm{e}^{j\Phi(u,v)}$ and f the focal length of the lens.

Before trying to evaluate equation (4.8) 'as is', it is interesting to make a few remarks. We deal here with Fraunhofer diffraction which relies on small wavelengths approximation (see §3.2.7 and [11]). If λ is very small, then $k = \frac{2\pi}{\lambda}$ is very large and we should expect that the phase term of the exponential of eq. (4.8) will vary rapidly. On the contrary, the input amplitude term $a(x,y)$ varies slowly compared to the phase. In that particular case eq. (4.8) can be evaluated with the method of *stationary phase* (see [36] p.36, [11] p.888, [43], [91]). Considering the integral:

$$\iint_{-\infty}^{+\infty} g(x,y)\mathrm{e}^{jk(x,y)} dxdy$$

the stationary phase method allows to write:

$$\frac{\partial h(x,y)}{\partial x} = \frac{\partial h(x,y)}{\partial y} = 0$$

so in our particular case the previous relation becomes:

$$\begin{cases} \dfrac{\partial}{\partial x}\left(\varphi(x,y) - \dfrac{2\pi}{\lambda f}(ux+vy)\right) = 0 \\ \dfrac{\partial}{\partial y}\left(\varphi(x,y) - \dfrac{2\pi}{\lambda f}(ux+vy)\right) = 0 \end{cases}$$

We have found [43][42][44] a relation that gives coordinates of the point $M'(u,v)$ image of $M(x,y)$ by the transformation associated to φ:

$$\begin{cases} \dfrac{\partial\varphi(x,y)}{\partial x} = \dfrac{2\pi}{\lambda f}u \\ \dfrac{\partial\varphi(x,y)}{\partial y} = \dfrac{2\pi}{\lambda f}v \end{cases} \tag{4.9}$$

The next step to determine completely the transformation that will redistribute the energy of a Gaussian beam profile to a uniform profile, is to find relations $u = u(x,y)$ and $v = v(x,y)$. It is worth to notice that both Gaussian input amplitude $a(x,y)$ and uniform output amplitude $A(u,v) = \mathrm{Rect}\left(\frac{u}{\alpha}\right)\mathrm{Rect}\left(\frac{v}{\beta}\right)$ are separable functions[4]. So our case can be reduced to a one dimensional problem as depicted in Fig. 4.10. In particular, since conservation of energy imposes [43][46] that the area under the one–dimensional Gaussian input beam profile must be equal to the area under the uniform output beam profile (see Fig. 4.10):

Input beam intensity profile: $$i(x) = \frac{1}{i_0}\mathrm{e}^{-2\frac{x^2}{\sigma^2}} \tag{4.10}$$

Output beam intensity profile: $$I(u) = \frac{1}{I_0}\mathrm{Rect}\left(\frac{u}{\alpha}\right) \tag{4.11}$$

So conservation of total energy imposes:

$$\int_{-\infty}^{+\infty} i(x)dx = 1 \qquad \text{that is} \qquad i_0 = \sigma\sqrt{\frac{\pi}{2}}$$

$$\int_{-\infty}^{+\infty} I(u)du = 1 \qquad \text{that is} \qquad I_0 = 2\alpha$$

Moreover as we are considering a one–to–one geometrical transformation, energy densities along the path of transformation also have to be equal:

$$\int_0^x |a(s)|^2\, ds = \int_0^{u(x)} |A(s)|^2\, ds$$

$$\frac{1}{i_0}\int_0^x i(t)dt = \frac{1}{I_0}\int_0^{u(x)} I(t)dt$$

---

[4] The Rect function is defined as $\mathrm{Rect}\left(\frac{x}{\alpha}\right)\begin{cases} = 1 & \text{if } |x| \leqslant \alpha \\ = 0 & \text{anywhere else} \end{cases}$

To evaluate the left part of previous relation, we use the Generalized Error Function that has already been introduced in §4.2:

$$\frac{1}{i_0}\int_0^x \mathrm{e}^{-2t^2/\sigma^2}dt = \frac{1}{2i_0}\sigma\,\mathrm{Erf}\left(x\frac{\sqrt{2}}{\sigma}\right)$$

The right term is much easier to evaluate:

$$\int_0^{u(x)} \mathrm{Rect}\left(\frac{s}{\alpha}\right)ds = \frac{1}{I_0}u(x) = \frac{1}{2\alpha}u(x)$$

So, we have found the relation between coordinates in the two planes of our transformation that redistributes a Gaussian profile into a uniform one:

$$u(x) = \alpha\,\mathrm{Erf}\left(x\frac{\sqrt{2}}{\sigma}\right) \tag{4.12}$$

where σ is the waist of the Gaussian input beam, and α is the dimension of the uniform rectangle output.

To get an overview of the situation: we reached the point where on the one hand conservation of energy gave us the relation $u = u(x)$; and on the other hand stationary phase allowed us to analytically determine $\varphi(x)$ as a function of u:

$$\begin{cases} \dfrac{\partial\varphi}{\partial x}(x) = \dfrac{2\pi}{\lambda f}u \\ u(x) = \alpha\,\mathrm{Erf}\left(x\dfrac{\sqrt{2}}{\sigma}\right) \end{cases}$$

Using the previous two equations, we are going to completely determine the function $\varphi(x)$ associated to our reshaping transformation.

$$\frac{\partial\varphi}{\partial x}(x) = \frac{2\pi}{\lambda f}\alpha\,\mathrm{Erf}\left(x\frac{\sqrt{2}}{\sigma}\right)$$

that is:

$$\varphi(x) = \int_0^x \frac{2\pi}{\lambda f}\alpha\,\mathrm{Erf}\left(t\frac{\sqrt{2}}{\sigma}\right)dt \tag{4.13}$$

Evaluating integral (4.13) requires some calculations. Let's consider the simpler form:

$$\int_0^x \mathrm{Erf}\,(s)\,ds \tag{4.14}$$

Integrating (4.14) by parts gives:

$$\begin{aligned}\int_0^x \mathrm{Erf}\,(s)\,ds &= \int_0^x 1\ .\ \mathrm{Erf}\,(s)\,ds\\ &= [s.\,\mathrm{Erf}\,(s)]_0^x - \int_0^x s\ .\ \frac{\partial}{\partial s}\,\mathrm{Erf}\,(s)\,ds\\ &= x.\,\mathrm{Erf}\,(x) + \frac{1}{\sqrt{\pi}}\left[\mathrm{e}^{-x^2} - 1\right]\end{aligned}$$

Reporting that result in eq.(4.13) that determines φ gives:

$$\begin{aligned}\varphi(x) &= \frac{2\pi\sigma\alpha}{\lambda f\sqrt{2}}\int_0^{x\frac{\sqrt{2}}{\sigma}} \mathrm{Erf}\,(s)\,ds\\ &= \frac{2\pi\sigma\alpha}{\lambda f\sqrt{2}}\left[x\frac{\sqrt{2}}{\sigma}\,\mathrm{Erf}\left(x\frac{\sqrt{2}}{\sigma}\right) - \frac{1}{\sqrt{\pi}}\left(\mathrm{e}^{-2\frac{x^2}{\sigma^2}} - 1\right)\right]\end{aligned}$$

Keeping in mind that $\varphi(x,y) = \varphi_x(x)\varphi_y(y)$ the final 2D–phase distribution is given by [46][42]:

$$\begin{aligned}\varphi_{Fourier}(x,y) = \left(\frac{2\pi}{\lambda f}\right)^2 \alpha\beta &\left[x\,\mathrm{Erf}\left(x\frac{\sqrt{2}}{\sigma}\right) - \frac{\sigma}{\sqrt{2\pi}}\left(\mathrm{e}^{-2\frac{x^2}{\sigma^2}} - 1\right)\right] \times\\ &\left[y\,\mathrm{Erf}\left(y\frac{\sqrt{2}}{\sigma}\right) - \frac{\sigma}{\sqrt{2\pi}}\left(\mathrm{e}^{-2\frac{y^2}{\sigma^2}} - 1\right)\right]\end{aligned} \tag{4.15}$$

where λ is the laser wavelength, σ the input laser beam waist, f the focal length and (α, β) are dimensions of the reconstructed rectangular output intensity distribution. So far, we have analytically determined a phase function that, when inserted in the optical setup depicted Fig. 4.9, redistributes the Gaussian–beam input amplitude of a TEM_{00} laser into a uniform rectangular intensity distribution in the output plane. It can be clearly seen on figure 4.13 that the function φ is continuous over the full aperture of the DOE; there are no dislocations. We are going to see that DOEs we have designed with this analytical phase function give much better results than IFTA–optimized DOEs [45][80]. Analytical design radically suppresses Speckle and gives smoother (so much more uniform) intensity patterns. However because of the smoothness of that distribution it is impossible to get a rectangle with very sharp edges in the reconstruction plane. This little drawback is definitely no trouble for our application to blood cells counting.

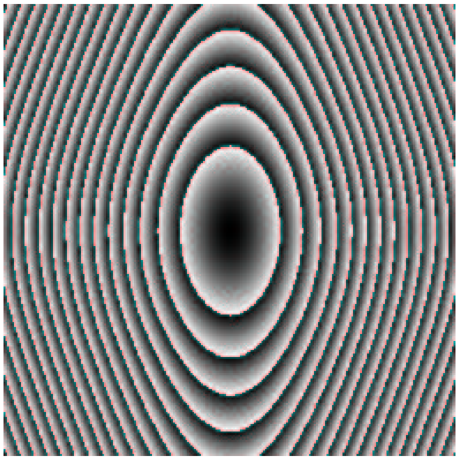

Figure 4.11: Modulo 2π two–dimensional plot of the analytically determined $\varphi_{Fourier}(x, y)$ phase function. With focal $f' = 10$mm, beam waist $\sigma = 0.65$mm, wavelength $\lambda = 488$nm, rectangle dimensions $\alpha = 100\mu$m and $\beta = 30\mu$m.

4.3.2.2 Fresnel case

The analytical phase function defined by eq. (4.15) is based on the Fourier optical setup depicted Fig. 4.9. However the lens of that setup is nothing more than an optical element that adds a quadratic[5] phase term to an incoming beam [19]. It is then certainly possible to combine this focusing function with

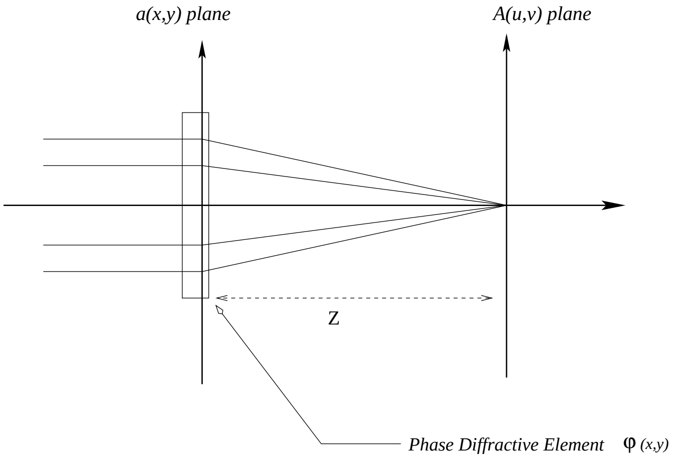

Figure 4.12: Fresnel analytical beam shaping setup.

---

[5] In the geometrical optics approximation.

the reshaping function to get the even simpler optical setup of Fig. 4.12. Considering Fresnel near–field diffraction, the relation between (x, y) and (u, v) planes is now a Fresnel transform (see §3.2.6). The stationary phase method applied to the Fresnel integral gives[6] [43][42][44]:

$$\frac{\partial \varphi_x}{\partial x}(x) = \frac{2\pi}{\lambda Z}(u - x)$$

where Z is the reconstruction plane distance. The conservation of energy gives the same relation in the Fresnel case. So we still have:

$$u(x) = \alpha \,\mathrm{Erf}\left(x\frac{\sqrt{2}}{\sigma}\right)$$

The analytical phase function in the Fresnel case is then given by:

$$\varphi_x(x) = \frac{2\pi}{\lambda Z}\left[\alpha \int_0^{x\frac{\sqrt{2}}{\sigma}} \mathrm{Erf}\,(s)\,ds - \int_0^x s ds\right]$$

That is:

$$\varphi_x(x) = \frac{2\pi}{\lambda Z}\left[\alpha x \,\mathrm{Erf}\left(x\frac{\sqrt{2}}{\sigma}\right) - \alpha\frac{\sigma}{\sqrt{2\pi}}\left(\mathrm{e}^{-2\frac{x^2}{\sigma^2}} - 1\right) - \frac{1}{2}x^2\right] \tag{4.16}$$

As one might have expected, the analytical phase function $\varphi_{Fresnel}(x, y)$ in the Fresnel case can be obtained simply by addition of a quadratic term to $\varphi_{Fourier}(x, y)$, that is [43][42][46]:

$$\varphi_{Fresnel}(x, y) = \varphi_{Fourier}(x, y) - \frac{\pi}{\lambda Z}\left(x^2 + y^2\right)$$

We have already stressed that analytical determination of DOE phase function $\varphi(x, y)$ is only possible when both input and output beams are rather simple (i.e. Gaussian laser beam and simple geometrical output patterns) [45][44][41][92]. For those simple cases, transformation of a beam of one irradiance into a beam with another irradiance is possible provided the fact that the energy of incoming and outgoing beams are the same (see [36] p.88). It is however possible to get slightly more complex reconstructed patterns by splitting the aperture on the DOE. Each sub–aperture reconstructs a sub–pattern which is a piece of a more complex one [40]. On have to stress that, in this latest case, the DOE sensitivity to input beam variations is increased [89].

---

[6] Input and output functions are still separable in the Fresnel case.

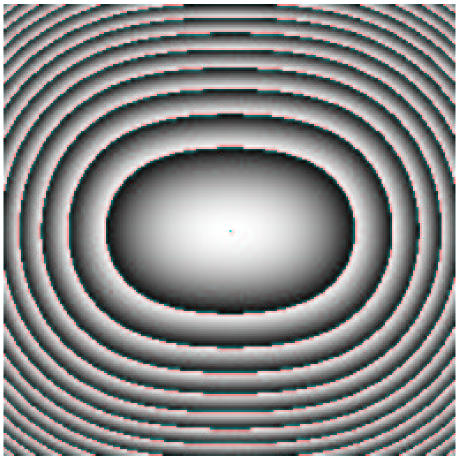

Figure 4.13: Modulo 2π two–dimensional plot of the analytically determined $\varphi_{Fresnel}(x, y)$ phase function. With reconstruction distance $Z = 10$mm, beam waist $\sigma = 0.65$mm, wavelength $\lambda = 488$nm, rectangle dimensions $\alpha = 100\mu$m and $\beta = 30\mu$m.

We have mentioned in §4.1 that the presentation of iterative and analytical methods to synthesize the phase function $\varphi(x, y)$ was driven by the fact that we had to develop a full software package for generation of diffractive elements. In the next section we are going to see how previous algorithms have been implemented.

4.4 Implemented algorithms

We have already stressed in sections §4.1 and §4.3 that any diffractive element has to be custom design to meet the application constraints. It is impossible to pick up and combine several 'multi–purposes' diffractive elements to get the desired optical function has it is done with refractive lenses. We have also mentioned that actually no software package can handle the full synthesis of a DOE from specifications to e–beam fabrication input file. Those are reasons why we had to develop our own software package. So, to be able to synthesize the diffractive beam shaper that will be integrated in our optical blood cell counting application, we had to study and implement algorithms we have selected in the previous two sections.

We have seen in section 4.1 that iterative and analytic design are the most adapted methods to determine the phase function of a diffractive beam shaper. We are then going to present encoded functionalities and some basic examples for each methods.

4.4.1 Iterative algorithm

It has already been explained in section 4.3.1 that iterative optimization algorithm basically relies on: initial phase guess, constraints in both planes and, of course, propagators. Since propagators have already been presented in section 3.4, we are going to focus on IFTA loop only. The iterative algorithm was encoded according to the block diagram represented on figure 4.5 page 60. However, the encoded algorithm is much more general than the one depicted Fig. 4.5 since the way each block perform its function can be freely chosen among a list of possibilities. This allows the design of beam shapers but also of a wide range of diffractive elements (near or far field, arbitrary reconstructed patterns, arbitrary merit functions, . . .). We are now going to briefly list functionalities with each block of the IFTA process.

4.4.1.1 Available initial phase functions

We have already stressed in section 4.3.1 the importance of initial phase function in iterative design. For this reason a wide choice of initial phase functions was encoded (see fig. 4.14). The random, pseudo–random and quadratic phase functions mentioned in reference [83] have been encoded. We furthermore have taken into account the case of off–axis diffractive elements by adding a parametrable linear phase term along each direction (see Fig. 4.14).

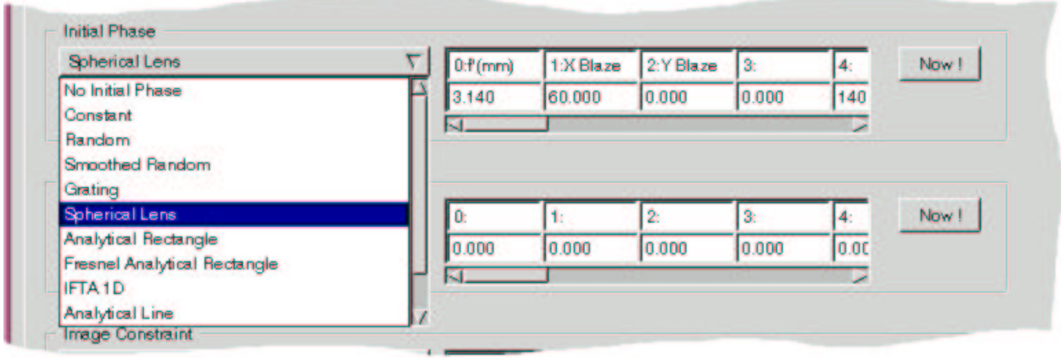

0:f'(mm)	1:X Blaze	2:Y Blaze	3:	4:
3.140	60.000	0.000	0.000	140

0:	1:	2:	3:	4:
0.000	0.000	0.000	0.000	0.0

Figure 4.14: Initial phase functions implemented in the realized diffractive elements CAD software.

4.4.1.2 Available image constraints

We have seen in the previous section that many different constraints can be considered in the image plane: replacement of amplitude [54], progressive replacement [83] or local replacement [60]. We moreover have add a very local constraint that allows to manually smooth pixels where phase dislocations appear during the optimization process. We also have to note that the selected constraint can be changed at any time during the synthesizing process.

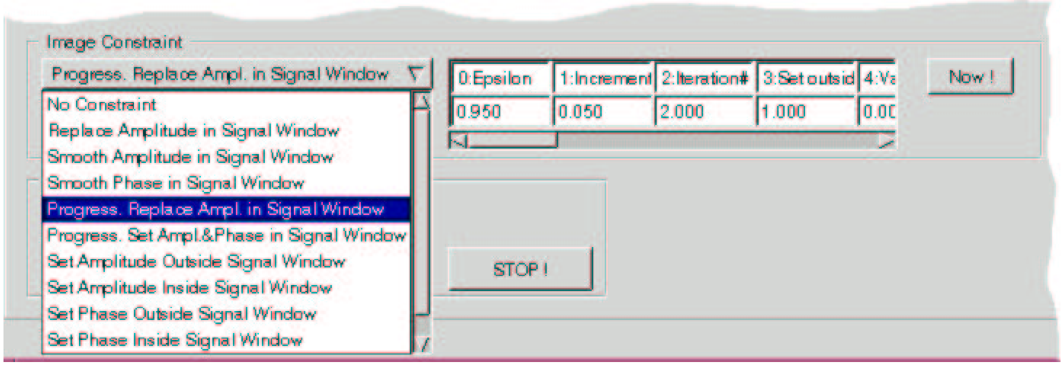
Image Constraint: Progress. Replace Ampl. in Signal Window

0:Epsilon	1:Increment	2:Iteration#	3:Set outsid	4:V
0.950	0.050	2.000	1.000	0.0

Figure 4.15: Image constraints implemented in the realized diffractive elements CAD software.

4.4.1.3 Available merit functions

Depending on the application, it is necessary to quantify diffraction efficiency, reconstruction accuracy or reconstructed pattern uniformity. Any of those functions can be selected to stop the optimization loop.

4.4.1.4 Validation

For validation purpose, we are going to synthesize the phase function of a diffractive beam shaper with the iterative optimization algorithm. We choose the Gaussian beam of a 488nm Argon ion laser as input intensity distribution. The beam shaper is made of 256 × 256 square pixels of 6μm and should reconstruct a uniform rectangle of 100μm×30μm in the Fourier plane. We also choose the random initial phase and progressive replacement constraint. After $N = 40$ iterations, uniformity has reached 0.81 and stagnates[7]. The

---

[7] It is the right place to check the convergence of iterative optimization between each loop as exposed in [80] page 195.

Merit Functions

☐ Uniformity 0.65

☐ Convergence Rate off

☐ Diffraction Efficiency 0.81

Figure 4.16: Merit functions implemented in the realized diffractive elements CAD software.

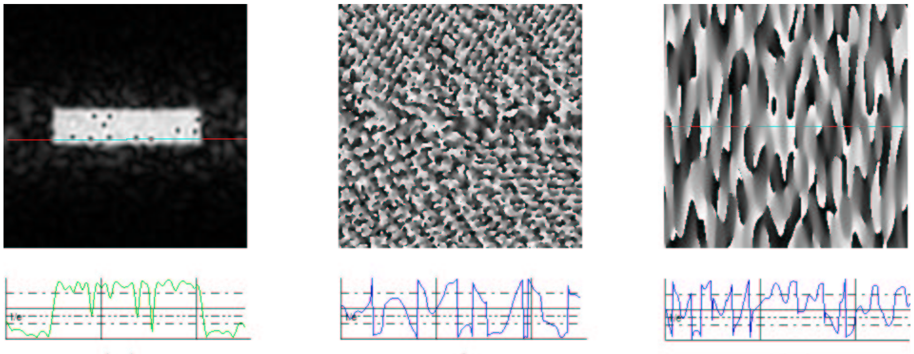

(a) (b) (c)

Figure 4.17: The phase function (c) was determined by the iterative algorithm. Reconstructed retangular intensity pattern (a) shows Speckle noise due to phase dislocations in image plane (b).

optimization loop is stopped. The reconstructed rectangle can clearly be seen on Fig. 4.17. If we oversample the image plane by embedding the DOE plane matrix in a larger matrix, we would see that amplitude fluctuations along a profile line (Fig. 4.17 in green) are obviously linked to phase dislocations (Fig. 4.17 in blue). This Speckle effect was expected and explained above.

4.4.2 Analytical design

The analytical design of diffractive beam shapers has already been introduced in section 4.3.2. We are now going to check that the analytically–determined phase function gives the expected result once propagated in the image plane

[40][46][43]. For consistency reasons, calculation of analytical phase was inserted in the initial phase selection box of our software (see Fig. 4.14).

Keeping the same conditions as those presented in the previous example, we are going to determine analytically the phase function of our test beam shaper. Once propagated in the image plane, the amplitude profile measurement tool shows a perfect uniformity for the reconstructed rectangle (see Fig. 4.18a and green profile of Fig. 4.18d). We are sure that no Speckle arises since the phase profile in the image plane (see Fig. 4.18d in blue) is also very smooth [81][88][93].

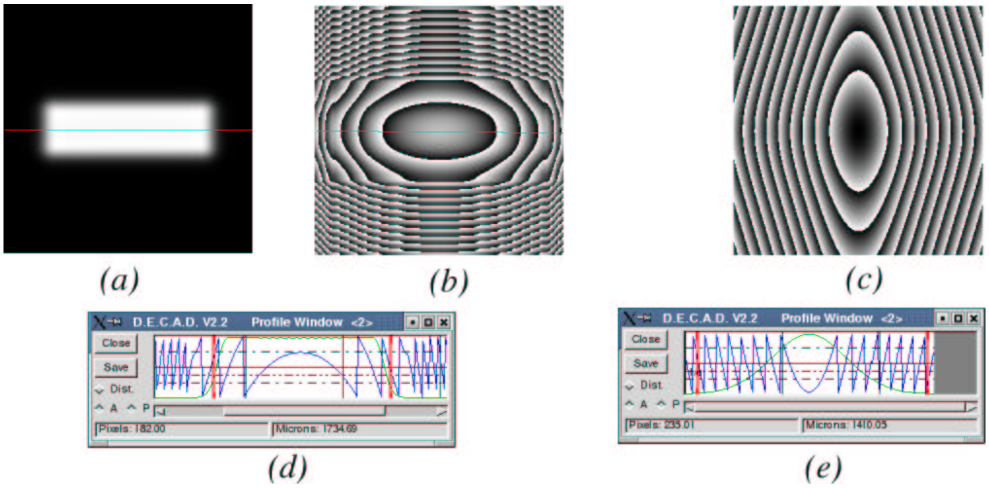

Pixels: 182.00
Microns: 1734.69

Pixels: 235.01
Microns: 1410.05

(a) (b) (c)

(d) (e)

Figure 4.18: The analytically determined phase function (c) shows a very smooth modulo–2π profile (e) in blue. In the reconstruction plane both amplitude (a) in green and phase (d) in blue are smooth, Speckle noise is then very limited.

4.5 Conclusion

In section 2 we have presented the working environment we have to deal with: blood cells. We have then briefly exposed basis of diffractive optics technology in section 3.1. In the previous chapter we have seen that, considering all constraints, diffractive beam shapers only can meet all the requirements of our blood cell counting setup.

Everything has now been put in place to synthesize diffractive optical elements: propagators, algorithms and software package. But those tools were presented in a quite general way in previous chapters. In the next sections we are going to list all the constraints that are specific to our blood cell counting application. Then, we are going to bring together and adapt tools that have already been presented. The goal is to determine a synthesizing method especially adapted to our application. So that we will be able to design a diffractive beam shaper that fulfills all the constraints associated to optical blood cells differentiation.

Chapter 5

Design of a DOE adapted to blood cell characterization

The goal of the present work is to design a new blood cells optical characterization system that should enhance performances of existing setups at lower costs. We have seen in previous chapters that diffractive optics is the most adapted technology to realize the required beam shaping optical function at reasonable cost.

This chapter will be dedicated to the synthesis, fabrication and testing of the top hat diffractive beam shaper we propose to integrate in Abx Diagnostics analyzers.

5.1 Introduction

We have now put in place the whole environment of our optical blood cell counting application. Chapters 1 and 2 introduced the context of our work: hematology. Blood cells and their standard characterization methods have also been presented. From this, it has followed that a very particular light distribution was required at measurement point to ensure accurate and stable characterization of blood cells. In chapter 3 we introduced diffractive optics that enable realization of complex optical functions (like the desired one) at low cost. We have so presented insights of diffractive optics from design methods to prototyping.

So, now all the working environment has been set, this chapter will be dedicated to the design, fabrication and test of final diffractive optical elements that will realize the targeted beam shaping function. Furthermore, in that chapter, the diffractive beam shaper will no more be considered as a stand alone optical component but as a part of an optical system that should fulfil defined specifications and deals with various constraints.

The beginning of that chapter will be dedicated to the presentation of specifications and constraints that we will have to deal with. Next, we will check that whether that desired diffractive beam shaper is physically realizable; that is whether required performances are compatible with laws of diffraction introduced in chapter 3. We will then calculate the phase function $\varphi(x, y)$ of our diffractive beam shaper, fabricate prototypes and test performances of those prototypes.

5.2 Constraints

Up to now we have only considered diffractive elements as isolated optical components. This was driven by the fact we were only introducing diffractive optics technology. But we have to keep in mind that our diffractive beam shaper will only be one optical component among the others. That is, we have to consider our optical blood cells counting setup globally and carefully study what kind of constraints it involves for this diffractive beam shaper to consider a global optimization.

5.2.1 Optical constraints

5.2.1.1 Geometrical specifications of intensity distribution

The first constraint obviously comes from specifications of the intensity distribution our diffractive beam shaper should realize at the measurement point. We have already mentioned in chapter 1 that the ideal light distribution is a *flat top* one. Considering Fig. 5.1a it is obvious that the intensity of the light–blood cell interaction will vary depending on the position of the cell when it crosses the laser beam. Whereas, as depicted in Fig. 5.1b, a deviation of the blood cell trajectory has no effect on the intensity of light cell interaction if light distribution is a flat top one at measurement point.

A fluidic system [1][2] based on two concentric flowing sheaths ensures that blood cells are transported inside a flow of 40μm of cross section (see Fig. 2.10). Since this flow can somehow deviate from its central position, the total width of the rectangular intensity distribution is chosen to be 100μm. The height is chosen to be 30μm. One might wonder why choosing a rectangle where a simple line would be much easier[1] to realize with diffractive optics? The velocity of blood cells inside the flow cell is about 8ms^{-1} and the diameter of a cell can be as low as one micron. This means that electronics bandwidth

---

[1] Because of the phase freedom in the image plane.

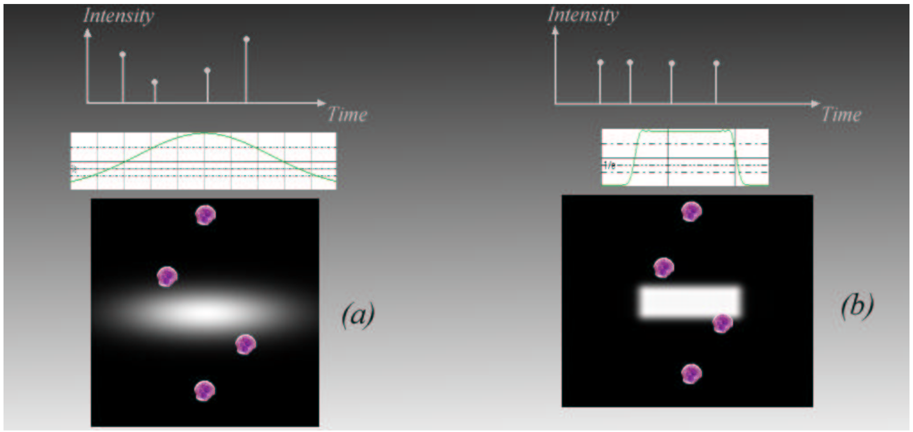

Figure 5.1: Simulated intensity distribution at the measurement plane without beam shaper (a), with the Flat Top diffractive beam shaper (b).

would have to handle events as fast as a few tens of microseconds, which is not possible with standard electronics. By choosing a height of 30μm we are sure that any event will last at least four microseconds.

It also has to be noted that the flat top profile has to be maintained over a distance of ±20μm from the measurement plane. This constraint comes from the fact that, position of a blood cell inside its transporting flow sheath can vary both transversally and longitudinally with respect to the laser beam. This constraint is of primary importance when designing the phase function $\varphi(x, y)$ of the diffractive beam shaper. We have seen in section 3.5 that phase influences propagation of light [36]. So to get a large depth of field, phase has to be as constant as possible in the reconstruction plane. Furthermore, it has also been mentioned (see §3.5 and §4) that the reconstructed phase in the image plane strongly depends on the method used to optimize the phase function $\varphi(x, y)$ encoded in the DOE surface reliefs.

Uniformity of the flat top also definitely matters. The more uniform the flat top, the more accurate blood cell characterization will be. If the optically measured parameter is the blood cell light transmittance (see 2.3.2), experiment has proven that uniformity has to be less than 6%. In the case of measurement of forward or side scatter (see 2.3.2), the impact of uniformity is less critical although quite difficult to quantify accurately .

5.2.1.2 Laser type

We have seen in section 3.5 that the input laser intensity profile has to be accurately known when designing diffractive optical elements. In our case, the laser wavelength is imposed by the use of a specific dye (Thiazole Orange) to stain reticulocytes for measurement of their fluorescence (see §2.3.2). Thiazole orange has its excitation peak at 488nm and fluorescence is detected around 530nm. For that reason, the light source of our optical blood cell differentiation setup will be the 488nm ray of an Argon ion laser. Fortunately, that kind of laser have excellent stability and very good geometrical beam parameters. The output beam is circular, Gaussian fundamental (spatial mode $\mathrm{TEM}_{00} \geqslant 99\%$) and has a very low divergence (0.95mrad). Since geometrical characteristics of the beam are excellent, we will use the raw beam (no telescope neither filtering optics) to illuminate our diffractive beam shaper. So the input constraint of our beam shaper is the Gaussian profile of the Argon laser.

We have now defined the overall specifications of our diffractive beam shaper; the input will be the Gaussian beam of a 488nm Argon laser whilst the output should be a $100\mu\mathrm{m}\times 30\mu\mathrm{m}$ flat top distribution with a depth of field of $40\mu\mathrm{m}$. It has to be noticed that those specifications proceed from theoretical considerations only. We are going to see that fabrication–related constraints also have a significant impact on final specifications.

5.2.2 Fabrication constraints

When designing diffractive optical elements, it is important to keep in mind that fabrication methods are not perfect. That is, we often have to modify initial specifications to take into account the fact that fabrication always lowers expected performances.

We have already mentioned that our prototypes of diffractive beam shapers will be fabricated by the e–beam direct write method (see §3.6) available at Chalmers University. Surface reliefs that are produced have 64 quantization levels which leads to a theoretical diffraction efficiency of more than 99% [14][50]. In practice, etching errors limit the diffraction efficiency to 85% in the first order [64][65][94][95]. Energy that is not diffracted in the first order is mainly found[2] in the central spot (order zero) and in higher orders (see Fig. 5.2). So, as represented Fig. 5.2a, the central spot and interferences between orders will dramatically decrease the light distribution uniformity. To overcome this problem, it is possible to shift the +1 order along both directions so that neither central spot nor higher orders are superimposed

---

[2] Considering a Fourier diffractive element.

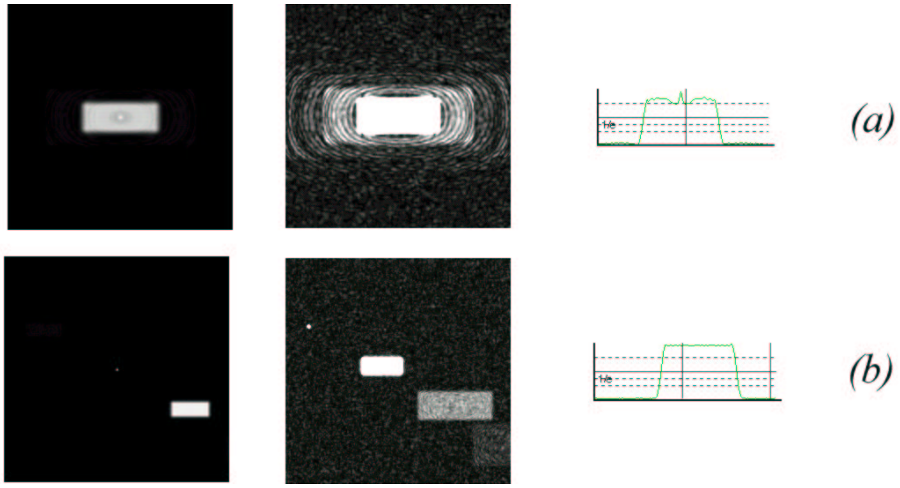

Figure 5.2: Simulated intensity distribution reconstructed by a Fourier Top Hat diffractive beam. On–axis case (row a), and off–axis case (row b).

onto the flat top distribution (see Fig. 5.2b). This shift is simply obtained by adding a modulo–2π linear phase term along both directions.

However, the off–axis coefficient can not be arbitrarily chosen if overlapping of higher orders onto the first one is to be avoided. As represented Fig. 5.2 and Fig. 5.3, dimensions of the pattern diffracted in the order N is N times dimensions of the +1 order pattern. So, to make sure there is

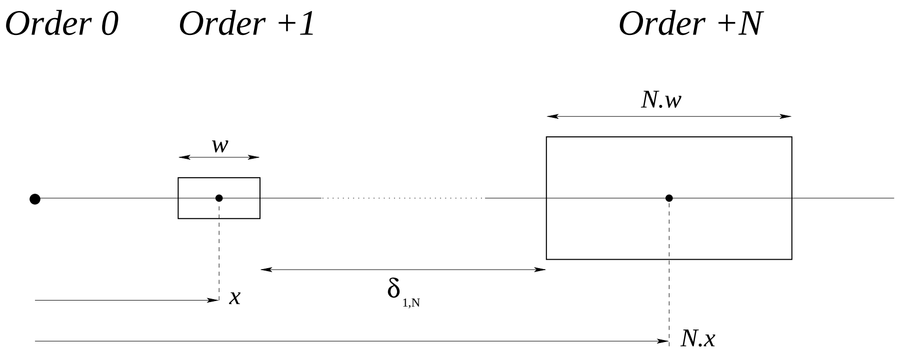

Figure 5.3: Overlapping of higher diffraction orders onto the first one.

no overlapping of the order N over the first one, distance $\delta_{1,N}$ has then to satisfy:

$$\delta_{1,N} = \left(Nx - N\frac{w}{2}\right) - \left(x + \frac{w}{2}\right) > 0$$

where w is the rectangle dimension (either width or height) and x its off-axis position. So we get:

$$x > \frac{N+1}{N-1} \cdot \frac{w}{2} \qquad N \in \mathbb{N}^* - \{1\}$$

The highest value of $\frac{N+1}{N-1}$ in the range $\mathbb{N}^* - \{1\}$ is three. So to ensure that no overlapping occures, the off–axis position x has to satisfy:

$$x > \frac{3}{2}w$$

where w is the rectangle linear dimension. On the practical point of view, we are going to exceed this criterion to allow more efficient filtering of high diffraction orders (see next section).

5.2.3 Measurement of forward scatter

This third kind of constraints comes from the complex optical environment our beam shaper will be integrated in. We have to make sure that performances of the beam shaper are compatible with specifications of the overall optical system.

We have seen in chapter 1 that our optical blood cells characterization setup should allow detection of light diffracted in the forward scatter direction (see §2.3.2 p. 15). Typical angle range for measurement of forward scatter is from less that 1deg to 9deg (see Fig. 5.4). We first have to choose the focusing lens focal length f so that emerging rays are tilted of less than 1deg. Since focal length of the focusing lens imposes dimensions of the reconstructing plane of the DOE, we will have to adapt the phase function scale factor to the focal length f to get the desired $100\mu\text{m}\times 30\mu\text{m}$ rectangle in the image plane.

Furthermore, we have seen in section §3.6 that whatever the fabrication method of out kinoform is, surface reliefs can not be perfectly generated. That is, reconstruction of higher diffraction orders like those depicted on Fig. 5.2 is unavoidable. Since dimensions of the pattern reconstructed in order N is N times dimensions of pattern of order $+1$, it is obvious that rays emerging from higher orders can eventually be tilted of more than one degree and then introduce stray light when detecting forward scatter. Fortunately, it is possible to suppress almost all higher orders if we insert a pinhole at some distance behind the focusing lens. Diameter of the pinhole is chosen so

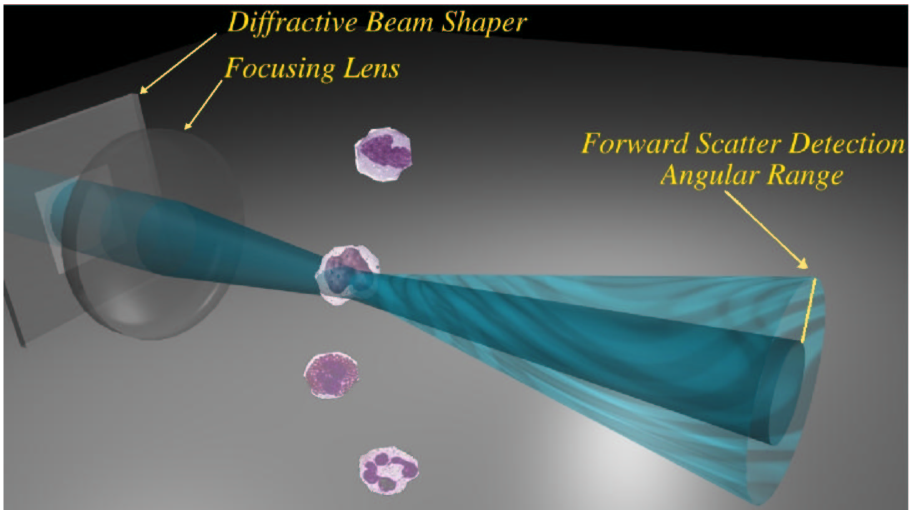

Figure 5.4: Schematic representation of the geometrical constraint imposed by measurement of light diffracted by white blood cells in the forward scatter direction (1deg to 9deg).

that 100% of the energy of the +1 order is transmitted whereas other orders are either suppressed or strongly attenuated.

5.2.4 Tolerancing

Tolerancing is usually a subject of little concern in laboratories optical setups. It is, however, the cornerstone of any industrial mass–produced optical system. The optical system we propose will be produced at more than four hundred units per year. It is obvious that complex and long alignment process for our diffractive beam shaper can not be considered. The overall system has to be rugged enough to handle small deviations of specifications without any severe drop of performances.

Parameters that are eventually subject to drift are input beam diameter and centering of the DOE with respect to the optical axis. We have seen in §3.5 that some design methods are more sensitive than others to variation of input beam profile and to misalignments. This will be taken into account when selecting the final optimization method to generate the phase profile $\varphi(x, y)$ of our diffractive beam shaper.

5.2.5 Diffractive beam shaper specifications

In previous sections we have considered the overall optical blood cell characterization system and from this, we have listed constraints imposed to our diffractive beam shaper. It is now possible to sum up all those constraints and define specifications the DOE will have to fulfil for optimal performances of the whole optical blood cell characterization system.

Now that all specifications of out diffractive beam shaper have been defined we are going, in the next section, to check whether this quite heavy list is compatible with physics of diffraction.

Input laser	
Wavelength	488nm
Type	Circular TEM_{00}
Beam diameter at $1/e^2$	0.65 mm
Output intensity distribution	
Type	Flat Top
Dimensions	$100\mu\mathrm{m}\times 30\mu\mathrm{m}$
Depth of field	$\pm 20\mu\mathrm{m}$
Uniformity	as good as possible
Off–axis with no overlapping of higher orders over the +1 order.	
Emerging rays are tilted less than 1deg.	
Sensitivity to misalignments as low as possible	

Table 5.1: Specifications of a diffractive beam shaper adapted to blood cells optical characterization.

5.3 Preliminary calculations

5.3.1 Preliminary calculations

Previous sections of that chapter were dedicated to the definition of specifications our diffractive beam shaper will have to fulfil. We have seen that specifications listed in table 5.1 come either from the beam shaping function or from the overall optical system.

We now have to make sure those specifications are not irrelevant but really compatible with physics of diffraction we introduced in section 3.2.

So, we are going to carry out some preliminary calculations to make sure that desired performances can really be achieved.

5.3.2 Pixel number and pixel size

One of the very first step in diffractive optics design is the choice of the pixel number and pixel size in DOE plane. When sampling the two dimensional phase function $\varphi(x, y)$ (see §3.3 and §3.6), the smaller and more numerous pixels are, the closer from the analog function we get. The number of pixel is however limited by the capacity of computers to handle huge amount of data. We choose a matrix size of 2048 × 2048 pixels to represent the phase function $\varphi(x, y)$ of our diffractive element. This number of pixel is large enough to get a high SBWP number (see §3.3) and leads to reasonable delay when computing FFT (see §3.3.2).

Now the matrix dimensions[3] have been chosen, dimensions of pixels have to be defined. The overall dimensions of the DOE aperture D are given by the product of the pixel number N by the pixel size in hologram plane p, that is: $D = Np$. This aperture D has to be large enough to transmit the input laser beam without any truncation effect. If the laser beam were truncated by the aperture, ripple oscillations would appear in the near filed whilst intensity would be reduced in the far field. To make sure that no truncations effects occure, we define the DOE aperture D according to the "$d \approx 4.6\sigma$" criterion. This criterion ensures that oscillations due to diffraction by the aperture are less than 1% [96]. Thus, the aperture diameter has satisfy $D = 4.6\sigma$ where σ is the laser beam radius at $1/e^2$ of intensity. So the aperture has to be $D = Np = 4.6\sigma$. Therefore, dimension p of our square pixel in the DOE plane has to be at least:

$$p = \frac{4.6\sigma}{N} = 0.73\mu\text{m}$$

We are going to retain the value of 0.75μm to take into account fluctuations of the waist from one laser head to another.

Square pixels of 0.75μm can easily be realized with the e–beam direct write method (see §3.6) [61][62][63]. Since the feature size of that prototyping technology can be as low as hundrendths of microns, no complex considerations such as proximity errors compensation has to be introduced [85][65]. Furthermore, dimensions of 0.75μm for pixel size ensures that we are in the validity domain of scalar diffraction. Scalar diffraction requires that the diffracting structure feature size to be at least ten wavelengths (see 3.2.2

---

[3] In that work we are only considering the case of square DOE aperture.

and [19]). Since one single pixel is about a wavelength, the only requirement in our case is the smallest feature size to be about ten pixels, which is obviously always the case. Nevertheless this will be checked later when generating the phase function $\varphi(x, y)$.

5.3.3 Image plane calculations

Whatever the type of our DOE will be (near or far field), we first have to choose either the focal length or the reconstructing distance of our setup. We have also seen in the previous section that detection of forward scatter measurement has to be kept in mind when defining the numerical aperture of our DOE. In particular, rays emerging from the DOE have to be tilted less than one degree with respect to the optical axis otherwise stray light could be introduced in the forward scatter measurement. So if θ is the maximum tilt angle, σ is the laser beam radius; the reconstructing distance z has to be chosen so that:

$$\theta = \arctan \frac{\sigma}{z} \leqslant 1\text{deg}$$

that is:

$$z \geqslant \frac{\sigma}{\tan(1\text{deg})} = 18.6\text{mm}$$

We are going to choose $z = 20$mm both to keep a safety margin and because $f' = 20.0$mm correspond to catalog standard lenses. Considering the setup of our blood cells counting application depicted Fig. 5.4 and Fig. 2.12, the distance between the flow cell and the focusing element (either lens or DOE) will be about 15mm which is a good value that allows a pretty compact setup.

Now that the reconstructing distance has been defined, it is time to turn our attention to the image plane. We have seen in section 3.3 that dimensions p' of a pixel in image plane is given by [31][19][94][51]:

$$p' = \frac{\lambda f}{Np}$$

So considering choices that were made above, the pixel size in image plane in our case is $p' = 6.35\mu$m. To be really accurate, it has to be mentioned that p' is the distance between two adjacent spots in the image plane, that is, the sampling grid in the image plane. When comparing $p' = 6.35\mu$m with the desired dimensions $100\mu\text{m}\times 30\mu\text{m}$ of the uniform rectangle, it is obvious that the resolution is more than enough along the wide axis whilst it is more tightened along the small one.

Now we have seen that the sampling distance p' in the image plane is enough to get accurate reconstruction of the desired rectangle, one might wonder what is the minimal spot size in that plane? Considering a simple lens of focal length f, the focused spot diameter d_0 is given by (see [96] p. 676):

$$d_0 \approx 2\frac{\lambda f}{\pi \sigma} \tag{5.1}$$

where σ is the incoming laser beam radius at $1/e^2$ of intensity (see [96] p. 676). So the diameter of the smallest spot in the image plane is $d_0 = 19\mu$m. When comparing the value $d_0 = 19\mu$m to the value $p' = 6.35\mu$m, one might wonder if something would not be wrong. In fact, those two quantities are quite different as p' is the sampling grid spacing in image plane whereas d_0 represents diameter of the smallest spot that can be generated with this optical setup. One question arises, does the fact we have $d_0 > p'$ really matter? It of course does, but it does definitely not bother in our very special case. The fact we have $d_0 > p'$ involves that the field amplitude can not vary strongly from one pixel to the next one. This means neither sharp edges nor accurate details can be reconstructed with that setup. Our application does not require sharp edges but high uniformity so the fact that we have $d_0 > p'$ does not bother. Moreover, as the field can not vary strongly from one pixel to the next one, intensity variations due to Speckle should be very limited which is highly desirable to get a good uniformity. So, although the fact $d_0 > p'$ does have an impact on the field in reconstruction plane, the effect is a rather good one for our beam shaping application.

5.3.4 Beam shaping coefficient β

We have seen in section 3.3.2.4.1 that the accuracy of the beam shaping optical function can be estimated by the value of the parameter β:

$$\beta = \frac{2\sqrt{2\pi} r_0 y_0}{\lambda f}$$

Where r_0 is the input laser beam radius at $1/e^2$ of intensity and y_0 is the reconstructed pattern half–width. Choices that were made in previous sections involve a value of $\beta_{Horizontal} = 8.3$ for the horizontal axis and $\beta_{Vertical} = 2.5$ along the vertical axis. According to [36] p.13 and p.136, the value $\beta_{Horizontal} = 8.3$, although a bit low, should be enough to achieve good beam shaping. Vertical axis is more tricky as dimensions are one third of the horizontal axis. The value $\beta_{Vertical} = 2.5$ can not lead to good results along vertical axis. Examining figures 5.5a and (b), it is obvious that edges of the

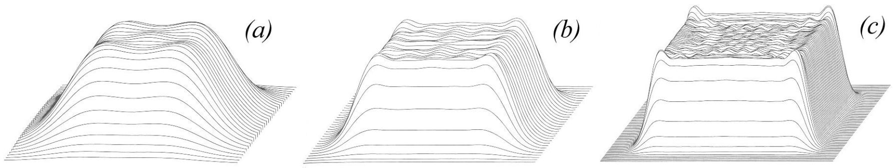

Figure 5.5: Simulated profiles of square spots obtained with increasing values of β parameter: β=4(a); β=8(b) and β=16(c).

reconstructed pattern will be quite smooth especially along the vertical direction. However, our application does not require particularly sharp edges along the vertical direction. Having a look at Fig. 5.2, we see that the most critical parameter is uniformity along the horizontal direction.

5.3.5 Sampling

In the previous paragraphs DOE aperture dimensions and image plane scaling calculations were performed with no or little concern to sampling rate. We are now going to check that the Nyquist theorem is satisfied in both planes.

Concerning the image plane, we have seen that the reconstructed pattern will have rather smooth edges and intensity variations should be as small as possible inside the rectangle. As a consequence, a pretty low sampling rate will be enough to reproduce that pattern [19][31]. The sampling grid spacing in the image plane $p' = 6.35\mu$m should be enough to accurately sample the 100μm$\times 30\mu$m pattern at least along the horizontal direction.

5.3.6 Remarks

We have seen in previous sections that specifications of the diffractive beam shaper defined in §5.2 are compatible with physics of diffraction. However, we have also seen that the beam shaping function will be much more difficult to consider along the vertical axis. So, we probably can not expect very good performances along that axis. It was furthermore mentioned in chapter 4 that realizing a uniform rectangular light distribution in the reconstruction plane is one of the most tricky task with diffractive optical elements. One solution to enhance resolution along the vertical axis is to use a beam expander to increase radius of the input laser beam. This would lead to a higher β coefficient and to a smaller spot size d_0. This is definitely possible but would require at least two additional lenses and would therefore increase both costs and alignment time.

So, we prefer to concentrate our effort on the beam shaping optical function. The focusing function will be realized by a classical refractive lens. This means we are only going to consider Fourier type diffractive optical elements. All available degrees of freedom will be used to achieve the best possible beam shaping function.

The choice of a Fourier type diffractive optical element is not really a limiting one. Standard BK7 plano–convex lens will be used so the cost increase will be rather low. Furthermore this setup also have some advantages. First it is possible, if needed, to scale dimensions of the reconstructing plane by adjusting the focal length of the focusing lens. This feature, which of course does not exist with Fresnel type DOEs, can be valuable to adapt the reconstructed light distribution to slightly different optical setups. Moreover the BK7 focusing lens will also protect the final plastic injected replica of DOE from scratches, dusts and solvents that are frequently encountered in industrial environment.

5.4 Design and simulation

5.4.1 Design

In the previous section we have taken care to check that the overall specifications of our diffractive beam shaper defined in §5.2 are compatible with the physics of diffraction. It appeared that, although those specifications are a bit tight, this beam shaper should be realizable with diffractive optics technology.

So, this section will be dedicated to the determination of the best possible phase function $\varphi(x, y)$ with methods presented in §3.5 and chapter 4. We are first going to generate this phase function $\varphi(x, y)$ using an hybrid analytical/iterative method then, we will discuss the obtained result and check its sensitivity to various parameters such as misalignments or laser beam waist fluctuations.

5.4.2 Phase function synthesis

It was mentioned in sections §3.5 and §4 that generation of the two dimensional phase function $\varphi(x, y)$ can be achieved either using analytical or numerical methods. Analytical method usually leads to very smooth intensity and phase distribution in the reconstruction plane [45][51][82], whilst numerical methods can take into account various parameters during the optimization loop [85][53][55][51][50][65].

According to the values of $\beta_{Horizontal}$ and $\beta_{Vertical}$ parameters calculated in the previous section, we can expect the phase optimization to be rather tricky in our case. For that reason, we propose to combine both analytical and iterative optimization methods into a single one hybrid optimization method. So we are going to take part of the smoothness of analytical method and of the versatility of the iterative one. We are first going to analytically determine the phase function of our diffractive top hat beam shaper then, this phase function will be considered as the starting point $\varphi_0(x, y)$ (see Fig. 4.5) of the iterative algorithm. This latest algorithm will be used the complete the phase function determination as well as to include some other constraints. So we are first going to analytically determine the phase function $\varphi(x, y)$ according to the specifications of table 5.1. We, of course, are going to use the formulation of equation (4.15) derived in section 4.3.2 page 71. But a linear phase term will also be added along each direction to take into account the required off–axis behavior. So the final mathematical formulation is:

$$\varphi_{Fourier}(x, y) = \left(\frac{2\pi}{\lambda f}\right)^2 \alpha\beta \left[x\,\mathrm{Erf}\left(x\frac{\sqrt{2}}{\sigma}\right) - \frac{\sigma}{\sqrt{2\pi}}\left(\mathrm{e}^{-2\frac{x^2}{\sigma^2}} - 1\right)\right] \times \\ \left[y\,\mathrm{Erf}\left(y\frac{\sqrt{2}}{\sigma}\right) - \frac{\sigma}{\sqrt{2\pi}}\left(\mathrm{e}^{-2\frac{y^2}{\sigma^2}} - 1\right)\right] + 2\pi\left(xX_0 + yY_0\right) \quad (5.2)$$

Where (α, β) are dimensions of the reconstructed rectangle, f the Fourier lens focal length, σ the input laser beam waist, and (X_0, Y_0) the off–axis coefficients. This formulation was implemented as one of the available initial phase functions (see Fig.4.14 page 75) our design software can generate. If parameters of table 5.1 of p. 87 are used in the formulation of eq. (5.2), it leads to the phase distribution represented Fig. 5.6a. Once Fourier–propagated, one get the reconstructed plane of Fig. 5.6b. If fabrication errors (either linear or random) are added, it becomes obvious examining Fig. 5.6c that we have an off–axis beam shaper with no overlapping of higher orders onto the +1 diffraction order.

Horizontal and vertical profiles of Fig. 5.6b can be compared with values $\beta_{Horizontal} = 8.3$ and $\beta_{Vertical} = 2.5$ calculated in the previous section. As expected, shaping is good along the horizontal direction whereas it is rather rough vertically. This phenomenon, that has already been explained in section 5.3, comes both from the quite large sampling grid p' and spot size d_0 in the image plane and from the fact that analytical determination can not reconstruct very sharp edges.

To overcome that problem, we propose to use the phase function we have just determined as the initial phase function $\varphi_0(x, y)$ of iterative optimization

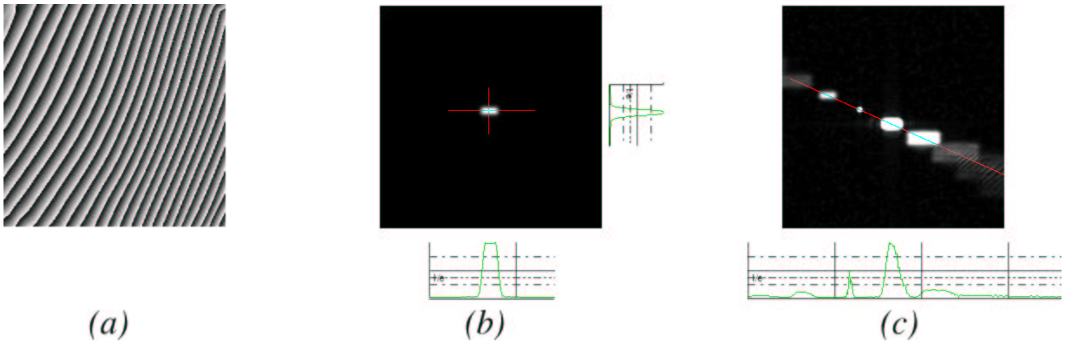

Figure 5.6: Analytically determined phase function (a). Reconstructed intensity distribution (b). Over–exposed reconstructed intensity distribution (c).

algorithm (see Fig. 4.5). This has two main advantages: first we are going to somehow sharpen the edges of the reconstructed rectangle by performing a few IFTA loops over a carefully chosen signal window. Second we are also going to reduce effects of quantization by including the quantization process in the optimization loop.

So the first step is to sharpen edges of the reconstructed rectangle as well as keeping the excellent uniformity provided by the analytical design. We are then going to use a local constraint by defining a signal window as the area surrounding the rectangular light distribution. This applied constraint will furthermore be a progressive one to make sure that no Speckle occurs during the optimization. Concepts of signal window and progressive constraints were introduced in section 4.3.1. So, by locally and progressively manipulating the amplitude in the image plane, we are going to slightly sharpen edges of the rectangular light distribution.

Now that both uniformity and edges of the reconstructed rectangular light distribution are achieved[4], we have to perform the last step in the design of our diffractive beam shaper: quantization. We have seen in section 3.6 that, although we will use the e–beam direct write method to realize our prototypes, this method still requires a quantization of phase levels. The e–beam available at Chalmers University of Technology allows 64 quantization levels which leads to a theoretical diffraction efficiency of almost 100%.

However, unless particular precautions are taken, quantization will unavoidably introduce stray light whatever quantization levels are. To reduce those effects we propose to use the *step wise* quantization algorithm exposed in reference [84]. This algorithm allows quantization to be progressively intro-

---

[4] This will be more accurately tested in the next section

duced. This algorithm was furthermore inserted in the IFTA loop to ensure that quantization has no effect over the uniformity of the reconstructed light distribution. We have now reached the point where we have fully determined

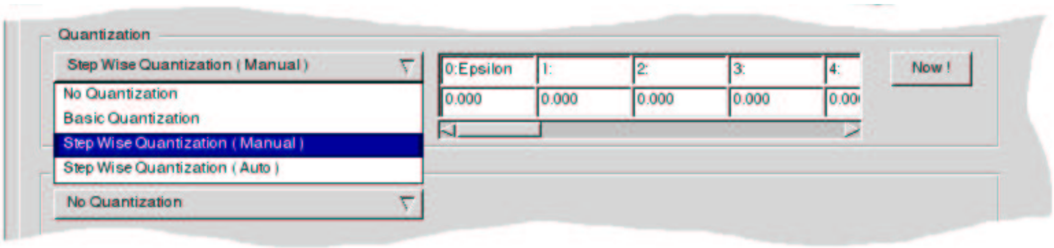

0:Epsilon	1:	2:	3:	4:
0.000	0.000	0.000	0.000	0.00

Figure 5.7: Quantization algorithms implemented in the realized diffractive elements CAD software.

the phase function $\varphi(x, y)$ the input wave undergoes. This means that we have a two dimensional array of quantized values representing phase delay to be realized. We are now going to analyze performances of this diffractive beam shaper using simulation tools presented in section 3.4.

5.4.3 Simulation of performances

Simulation of performances is definitely the cornerstone of diffractive optics design. Simulation tools allow to foresee what light distribution behind the DOE plane will be. Thanks to simulation it is possible to know where stray light will be localized, how much off–axis will be necessary or exactly adjust dimensions of the reconstructed pattern. It is then possible to realize less DOEs prototypes since we already have a good idea of what is going on in the image plane. So, a thorough examination of simulated results will lead to a faster and cheaper design process by decreasing the number of prototypes.

For those reasons we have developed our own design and simulation software. This software was designed to handle the synthesis of the phase function $\varphi(x, y)$ (either analytical or iterative methods are supported), simulation of performances by the use of various propagators (see section 3.4), tolerancing analysis (beam waist diameter, alignment sensitivity, ...) and finally generation of the very specific files required by the e–beam machine.

In that section we are going to thoroughly analyze the light distribution generated by the phase function $\varphi(x, y)$ determined in the previous section. We are going to use propagators presented §3.4 to check various parameters as depth of field, minimum feature size or misalignment sensitivity.

5.4.3.1 Depth of field

We have seen, when presenting constraints our DOE has to fulfil, that the flat top profile has to be maintained over ±20μm from the reconstruction plane. This depth of field is required by the stream that transports blood cells. Since depth of field is a distance measured along the optical axis, it is no more possible to use the Fourier propagator. It was mentioned in §3.4 that almost all propagators require the reconstruction plane to be perpendicular to the optical axis. Only the Kirchhoff formulation of diffraction can handle tilted surfaces (see §3.2.4). We propose to use that propagator to analyze the light distribution in a plane behind the DOE and parallel to the optical axis. In fact, we only need to $\frac{\pi}{2}$–rotate the reconstructed plane $\mathcal{R}$ along the U axis (see Fig. 5.8b) to get a plane $\mathcal{K}$ parallel to the optical axis and centered at the target distance $Z = f$. The strength of the Kirchhoff propagator also comes from the fact that dimensions and resolution of the reconstruction plane can be freely chosen. We propose to adjust those parameters to get an enlarged picture of the profile. Determination of the profile type (Gaussian or flat top) will be visually obvious. Once all the Kirchhoff propagators parameters are selected (vertical and horizontal pixel size, vertical and horizontal pixel number, reconstruction distance, . . .) this propagator leads to the reconstruction plane represented Fig. 5.8a. Profile number 2 is taken at

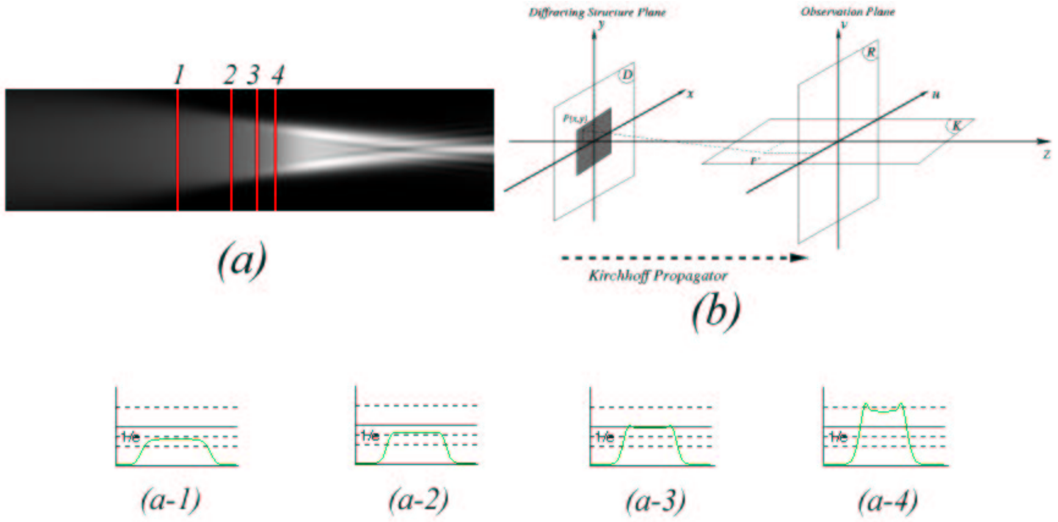

(a) (b)

(a-1) (a-2) (a-3) (a-4)

Figure 5.8: Simulated depth of field measurement. Picture (a) represents light amplitude in a plane parallel to the optical axis (plane $\mathcal{K}$ of sketch (b)). Profiles (a-1) to (a-4) taken in the plane $\mathcal{K}$ are perpendicular to the optical axis.

the perfect reconstruction distance $Z = f$. To get an estimated value of the depth of field, we examine the shape of profiles located in front and behind the distance $Z = f$. As long as the shape is still top hat, we are inside the depth of field range along the Z axis. Profile number 1 and 3 are limits beyond which any profile will show a rather rounded top. So from the pixel size specified as parameter to the Kirchhoff propagator, it is easy to convert the distance in pixel measured from profile one to profile two in the image plane into a distance in microns. So, simulation gives a depth of field of 0.5mm. It is quite interesting to note that left and right limits are not symmetrical with respect to the point $Z = f$. This phenomenon, which does not come from the diffractive behavior of our system, is encountered in any refractive optical system and is perfectly explained with geometrical optics.

5.4.3.2 Minimum feature size

We have mentioned in chapter 3.2 that only scalar diffraction will be considered in this work (see §3.2.2 p.23). From this consideration it follows that we are limited to large apertures and to diffracting structures with feature size about ten wavelengths. Remembering that feature size is defined as the length of a 0 to 2π phase delay structure, we now have to check that the diffracting structure $\varphi(x, y)$ synthesized in the previous section fulfils this requirement. Considering Fig. 5.9a, the minimum feature size is to be searched

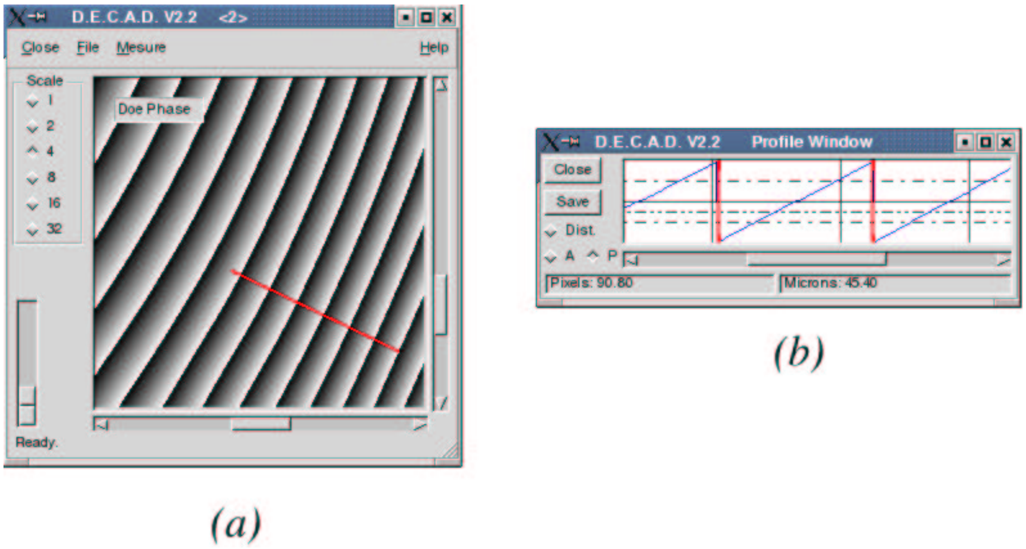

Pixels: 90.80

Microns: 45.40

(b)

(a)

Figure 5.9: Generated phase function minimum feature size measurement.

in areas where fringes have the highest spatial frequency. So by taking several profiles perpendicular to the fringes direction, we are manually looking for the narrowest 0 to 2π transition. The profile represented Fig. 5.9b was taken along the red line of Fig. 5.9a. Although it is probably not exactly the lowest 0 to 2π transition, it is enough to get an experimental validation. In Fig. 5.9b red cursors are positioned to select one transition. Distance between cursors are is shown in the lower part of Fig. 5.9b. We have $\Delta_{min} = 45\mu$m that is, about one hundred times the illuminating wavelength. We are in the validity domain of scalar diffraction.

5.4.3.3 Misalignment sensitivity

We have got to keep in mind that the diffractive optical element we are now analyzing is intended to be replicated in large quantities for integration in an industrial environment. As with any other mass–produced item, tolerancing will play here a major role. Since we can not spend much time to align this single optical component, we have to design an overall system that can not only ensure an automated and accurate positioning of the DOE[5], but also handle small misalignments without any severe consequences. We have seen in §3.5 that analytically synthesized diffractive elements are usually less sensitive to misalignments than IFTA–designed DOEs [51][50][89][82]. So in that section we are going to quantify how parameters like waist diameter or position can drift. This will again be realized with the software we have developed. Once the input laser type is defined, all geometrical parameters can freely be modified: laser beam position and tilt, beam diameter, beam quality, . . . So taking the final phase function $\varphi(x, y)$ defined earlier, we are going to check what happens in the reconstruction plane when beam parameters are fluctuating. We are first going to determine alignment tolerances along both directions by progressively shifting the waist along one direction. As

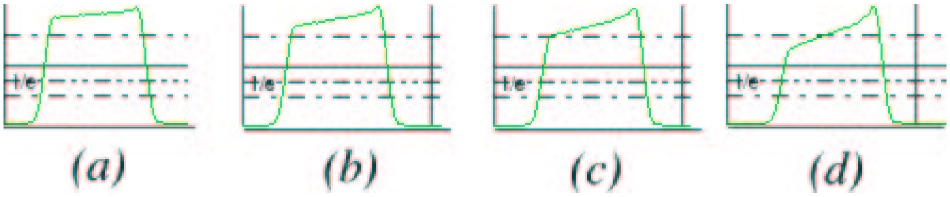

Figure 5.10: Simulated horizontal profile of the reconstructed intensity patterns. Input laser beam has been horizontally shifted of 10μm (a), 20μm (b), 30μm (c) and 50μm (d).

---

[5] This will be further detailed in section 5.6.

seen on Fig. 5.10, the reconstructed profile is still rather uniform as long as the beam waist is shifted less than 20μm. If the waist is further shifted, the profile is no more horizontal but falls in the opposite direction the waist has been displaced. Since laser illumination is symmetrical with respect to its center, it is obvious that horizontal profile would fall on the other edge if the beam waist were displaced on the left. Although not represented there, this was tested by simulation. The fact that our diffractive element is off–axis seems not to influence tolerancing to the left or to the right. So tolerancing along the horizontal position of the beam waist is $\pm 20\mu$m.

Vertical position tolerancing is also determined using that setup. Examining Fig. 5.11, vertical profiles are modified exactly on the same way than above. Examining Fig. 5.11 it appears that the laser beam can not be shifted more than 20μm vertically. This means that the position of the input laser beam can drift of $\pm 20\mu$m horizontally and vertically. We will see in section 5.6 how to handle those severe tolerancing constraints.

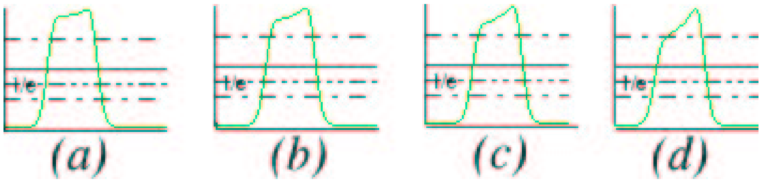

Figure 5.11: Simulated vertical profile of the reconstructed intensity patterns. Input laser beam has been vertically shifted of 10μm (a), 20μm (b), 30μm (c) and 50μm (d).

The last geometrical beam parameter that is subject to drift is the beam waist. The laser manufacturer gives a tolerancing of ±5% for the beam diameter. This means the beam diameter can range from 0.62mm to 0.68mm. Our diffractive beam shaper was, of course, designed for the standard value of 0.65mm for beam diameter. Just as it was done above, we propose to analyze the effects of a drift of beam diameter in the reconstructed plane with the simulation software we have designed. Figure 5.12 represents the reconstructed amplitude in case of lower limit (a), nominal value (b) and upper limit (c) of the laser beam diameter. If we carefully study profiles (a) to (c), it is possible to see that the rectangle is slightly overshaped if beam diameter is decreased whilst it is slightly undershaped if it is increased. Those effects are however rather weak and should not bother.

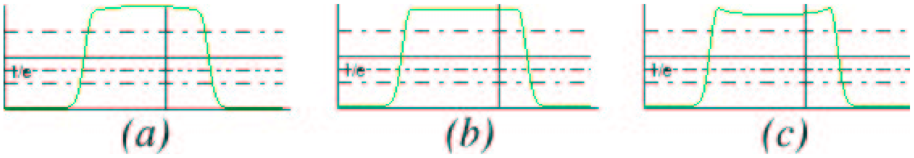

Figure 5.12: Simulated horizontal profile of the reconstructed intensity patterns. The beam shaper was designed for a target laser beam of diameter 0.65 mm (b). If the beam diameter is reduced to 0.62mm profile (a) is reconstructed, whereas if the beam is enlarged to 0.68mm profile (c) is obtained.

5.4.3.4 Uniformity

When specifications of our diffractive beam shaper were defined in §5.2 we stated that uniformity should be as good as possible. Although the analytically designed final phase function $\varphi(x, y)$ should lead to a very good uniformity [45][46][51], this parameter has never been analyzed up to now. We are first going to check if Speckle noise could arise and then analyze the effects of fabrication errors on uniformity.

The importance of Speckle noise in the image plane has already been stressed in §4.3.1. It was mentioned that Speckle noise is linked to phase dislocations in the reconstruction plane [78][81][84][87]. So we are going to thoroughly examine the phase $\Phi(u, v)$ associated with the amplitude $U(u, v)$ of the rectangular light distribution. Using the Kirchhoff propagator, we are going to zoom over the reconstructed rectangle by choosing a small recon-

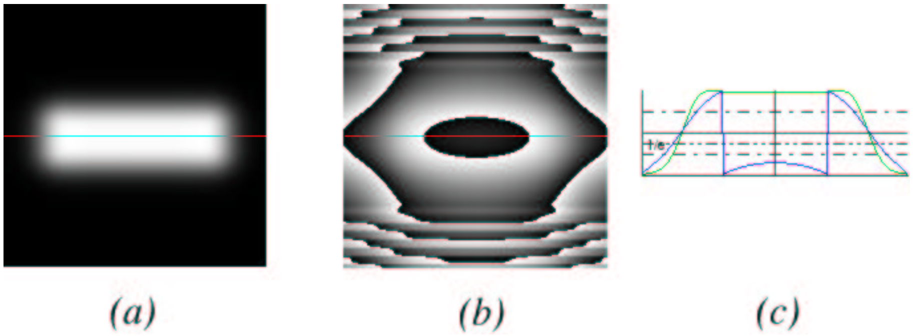

Figure 5.13: Simulated field amplitude (a) and phase (b) generated by the analytically determined beam shaper phase function. Figure (c) shows the amplitude (green line) and phase (blue line) profiles taken along the red line. Fabrication errors are not taken into account.

structed window but a high resolution (much higher than the grid spacing p' defined in section 5.3). Figure 5.13 represents both amplitude and phase of the reconstructed rectangle. Pixel size was chosen to be 1μm to make sure that potential amplitude fluctuations between sampling points are visible. Examining Fig. 5.13a and amplitude profile of Fig. 5.13c (green line), it is obvious that amplitude is very stable between sampling points. Furthermore, the phase profile of Fig. 5.13c (blue line) shows no dislocations but a smooth modulo–2π profile which should lead to a limited Speckle noise.

Although all precautions have been taken not to introduce any Speckle noise, we have seen in section 3.6 that fabrication will inevitably introduce errors that will lead to stray light in the reconstruction plane. Two types of errors are distinguishable; random and linear errors. Random errors appear in the e–beam writing process. Linear errors are due to the resist development step. Those errors are rather simple to represent mathematically. Random errors are represented by adding a white noise to the phase function $\varphi(x, y)$ whilst linear errors are represented by scaling the range $[0, 2\pi[$ to $[0, \epsilon 2\pi[$. We of course, have integrated those fabrication errors in the simulation software so it will be quite easy to study their consequences in the reconstruction plane. Figure 5.14 represents the image plane when 7% of random fluctuation

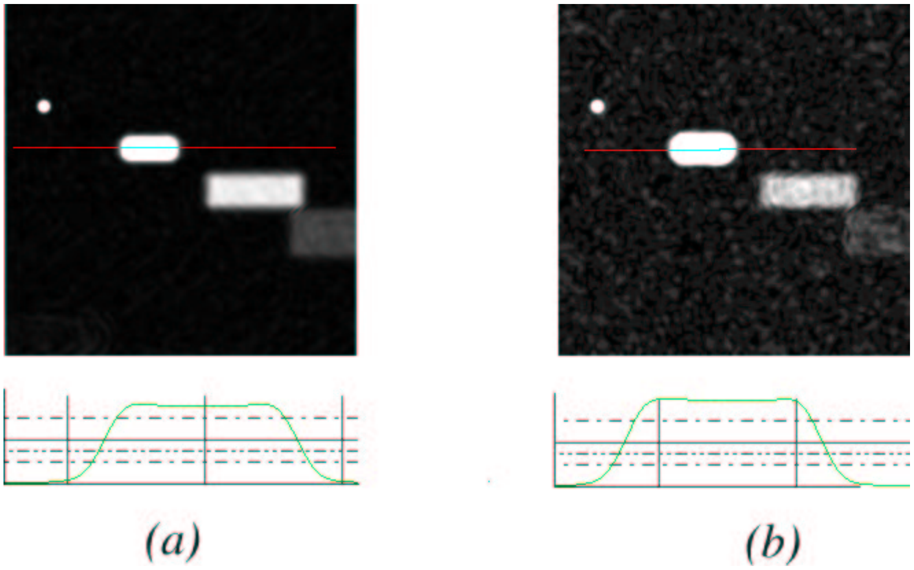

Figure 5.14: Simulation of effects of linear fabrication errors (a) and random fabrication errors (b) over the reconstructed pattern. Pictures are over–exposed.

are added to the phase function $\varphi(x, y)$. This leads to a strong spot in the order zero. As we have chosen off–axis design with no overlapping of higher orders onto the first one, this first diffraction order is located pretty far from the center. Therefore, the first diffraction order is only weakly influenced by random fabrication errors. As represented Fig. 5.14a, the horizontal profile is still smooth and uniform.

Now let's consider the case where development time has been exceeded introducing a linear scale factor of 1.2 onto the phase function $\varphi(x, y)$. The corresponding image plane is represented Fig. 5.14b. Horizontal profile of Fig. 5.14b shows no significant noise but diffraction efficiency has also dramatically dropped.

In that section we have used our design and simulation software to analyze performances of the phase function $\varphi(x, y)$ determined in section 5.4. According to the simulated results, our diffractive beam shaper will fulfil all specifications defined in table 5.1. This simulation step is of primary importance since it allows to estimate performances of the diffractive component decreasing the need for expensive prototypes.

However, it is of course not possible to skip the prototyping step in diffractive optics design. Although simulation tools are accurate, fabrication and test of prototypes is still necessary for the final validation of the component.

5.5 Fabrication

Previous sections were dedicated to the design and simulation of performances of the diffractive beam shaper we will integrate in our optical blood cells characterization setup. Now that the final phase function $\varphi(x, y)$ has been determined and performances have thoroughly been simulated, we are going to physically realize that phase function using the prototyping method exposed in section 3.6.

As mentioned in §3.6 we had the opportunity to work with the Chalmers University of Technology (Sweden) to realize our prototypes. The Chalmers University diffractive elements prototyping facility relies on e–beam microlithography. This method, that has already been detailed in section 3.6, allows realization of 64 level–quantized diffractive elements with direct write method (i.e. one single pass writing, no mask alignments).

In that section we are first going to expose the necessary data processing wortk that leads to the e–beam input files from the phase function $\varphi(x, y)$. We are next going to analyze this prototype and check how the fabricated surface relief function $h(x, y)$ matches the desired phase function.

5.5.1 Data processing

From section 5.4 we get the quantized phase distribution $\varphi_q(x, y)$. That is, a two dimensional array of 2048 × 2048 float values such as $\varphi_q(x, y) = k\frac{2\pi}{64}$ with $k \in \{0, 1, 2, \ldots, 63\}$. The constant factor $\frac{2\pi}{64}$ is not really useful since it does not carry any information. For that reason, only the quantization step number k is retained in the e–beam file format. Although 64 levels requires 6 bits to be represented, the e–beam uses a full byte for simplicity and memory alignment reasons. So our phase distribution $\varphi_q(x, y)$ will finally be represented with an array of 2048 × 2048 bytes. It should be noted that the e–beam file format also requires an offset value of +128 to be added to each value. Moreover data should be arrange in a pretty strange way: lines of 48 bytes separated by a carriage return code.

Some other information such as array dimensions or resist type (negative or positive) should also be stored in the e–beam input file header. All this data processing work has, of course, be implemented in our design and simulation software. So, once the final phase distribution is determined, all we have to do is to specify the Chalmers file format before saving to disk the distribution $\varphi_q(x, y)$.

It should be noted that the fact we have omitted the factor $\frac{2\pi}{64}$ means we have to deal with one byte integer numbers only. This leads to a pretty compact file format since our 2048 × 2048 pixels phase function is represented by a 4.2Mb long file only.

5.5.2 Fabrication

Once the data processing work has been done, this file is the starting point for the e–beam exposure step. During that process, the resist coated side of a quartz plate (see Fig. 3.1 p. 20) is scanned by the electron beam. The electron beam power (or dose) is modulated according to quantization value read in the input file data. As a result, the resist coated area is divided into 2048 × 2048 pixels, each exposed proportionally to the quantization number k of the phase function $\varphi_q(x, y)$. This process requires a few hours to be completed. It should be noted that random errors (see §5.4.3) sometimes occur in this step. Those errors can come from stepping motor precision or electron beam dose fluctuations. As mentioned earlier the chosen pixel size is large in our case, so e–beam point spread function compensation is not considered here.

The step that follows resist exposure is development. In that process, exposed areas are chemically etched. The etching strength is proportional to the e–beam dosage of exposure process and development time. So the surface relief function $h(x, y)$ gradually appear during the development step. Since that process is a chemical one, it is much less accurately controlled than the exposure. For that reason, it is usually realized in several steps. The resist is first etched for a short while, then the maximum depth is checked with an atomic force microscope. Since maximum depth is proportional to the etching time, it can be accurately controled. So by splitting the development process it is possible to get really close to the ideal depth, i.e. the ideal 2π phase delay. Although the maximum etching depth can be well controlled, it is never possible to exactly match the ideal depth. This means that DOEs are always either over or under exposed. This introduces linear errors since the phase delay range is scaled from $[0, 2\pi[$ to $[0, \epsilon 2\pi[$ so diffraction efficiency is decreased. However those fabrication errors a rather limited; random errors are then than 5% and maximum etching depth is about 95% of the target one (see Fig. 5.15). Examining Fig. 5.15 one can notice that t transition from one e–beam dose level to another is not sharp but rather smooth. As a consequence, the overall depth profile is also smooth and stray light will mainly be localized around the order zero [90][51][61][64][65].

Figure 5.15: Atomic force microscope picture of the surface relief profile of one prototype realized by e–beam direct write at Chalmers University.

Picture 5.16 represents our diffractive beam shaper prototype examined with a standard ×20 optical microscope. The pixelated–oriented fabrication method clearly appears there. Moreover, the scanning scheme of the e–beam machine can easily be guessed from Fig. 5.16. The total area to be exposed is divided into matrices of 64 smaller pixels. This has a consequence over the reconstructed pattern in the image plane. We have already stressed that the pixelated fabrication method leads to a convolution of the diffracted pattern with a *sinc* function [51][50][13]. Since we now have two grids (matrices and pixels) we should expect the final light distribution to be convoluted with two sinc functions. However misalignments of one matrix with respect to the other are very limited: less than 100nm along both directions. So this second convolution effect should not be too severe. Now that the diffracting phase function $\varphi(x, y)$ was determined and the corresponding surface reliefs function $h(x, y)$ was fabricated, we have reach the most exciting step of diffractive optics design: testing.

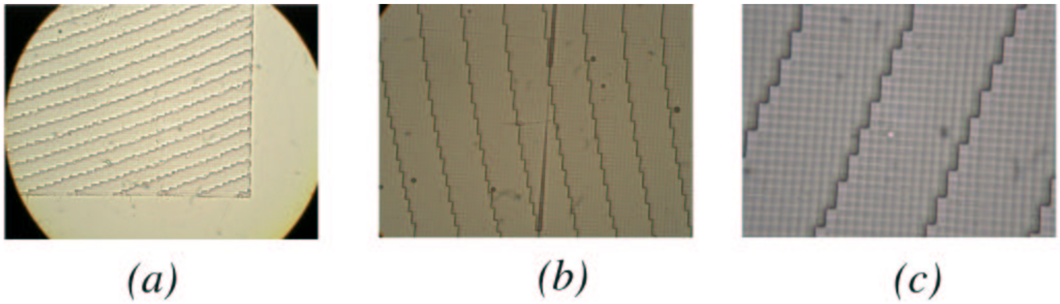

Figure 5.16: Microscope photographs of one of the realized prototypes taken with magnifications: ×10 (a), ×20 (b) and ×40 (c).

5.6 Test of performances

Previous sections of that chapter were dedicated to design and fabrication of our flat top diffractive beam shaper prototype. We have extensively used simulation tools to try to estimate performances and typical behavior of that diffractive component. Now that the DOE is realized, we are going to check that we get the expected behavior and compare real performances with the simulated ones.

It has to be stressed that we are not going to test the overall optical blood cells counting system in that chapter. We are only going to test the diffractive beam shaper as a single, isolated optical component. Validation of the entire optical system will be realized in the following chapter.

5.6.1 Mechanical integration

We have seen in section 5.4.3.3 that diffractive optical elements are quite sensitive to input beam misalignments. Moreover, even for prototypes testing purposes, we can not spend time to align or re–align the beam shaper every morning before experiments are started. So we propose a mechanical design that ensures, once the DOE has carefully been aligned, neither vibrations nor chocks will influence the alignment. This mechanical setup should be simple and rugged enough so that both laser and DOE can be swapped from one optical bench to another one. We propose to lock the DOE to the Argon laser head front plate (see 5.17). So we no more consider the laser and the DOE individually, but the overall as a shaped laser light source. The mechanical setup represented Fig. 5.17 is very simple and definitely efficient since the DOE holder is directly tightened onto the laser head front plate. This front plate is a good and stable mechanical basis, it was designed by the laser manufacturer to handle heavy fiber optics coupling mechanics. This shaped light source can be swapped from an optical setup to another with no adjustments of the DOE, this exactly matches our needs.

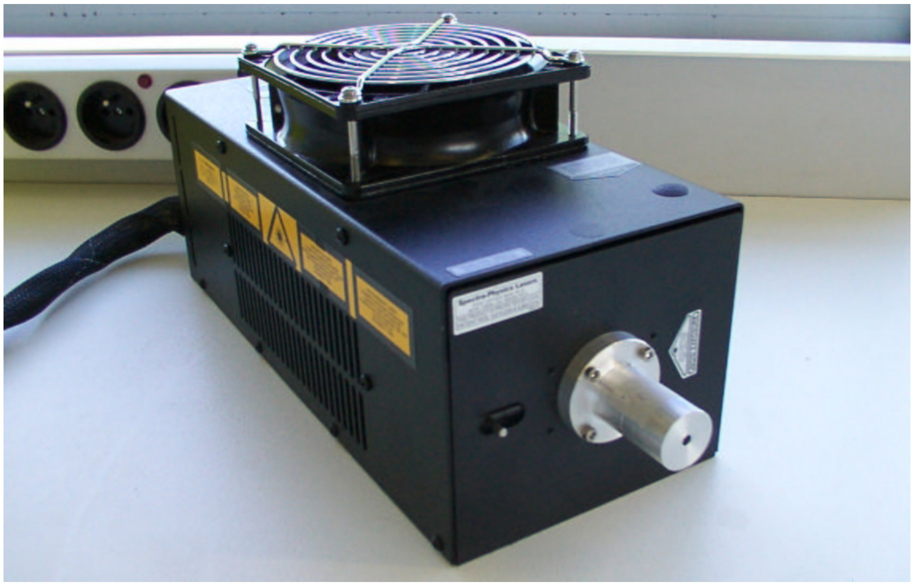

Figure 5.17: Mechanical integration of the diffractive beam shaper onto the laser head package.

Before this shaped light source can be used, we of course have to align the DOE with respect to the laser beam. At the first glance it would be tempting to use edges of the quartz plate as assembly marks. However, edges of the quartz plate are neither sharp nor regular and even not straight. This comes from the quartz substrate that was used: it is so hard that dicing or cutting it accurately is impossible. Neither it is possible to realize centering holes or marks with the required precision. To overcome this problem we are going to use UV–curable glue combined with a special DOE holder. Let's first consider the DOE holder represented Fig. 5.18. This part was home

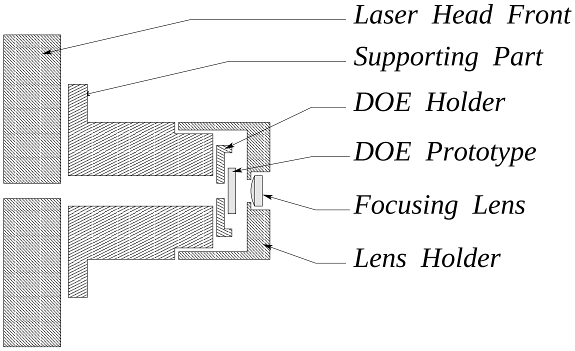

Figure 5.18: Schematic representation of the diffractive element holding mechanics.

designed and machined with good tolerances to hold the DOE quartz plate. The diffractive component is then glued onto that mechanical part. So, even if the quartz plate has been badly cut, we are only going to rely on the DOE holder package. In a second step, the DOE holder is encased into an alignment tool (see Fig. 5.18 and Fig. 5.19). This proposed alignment tool

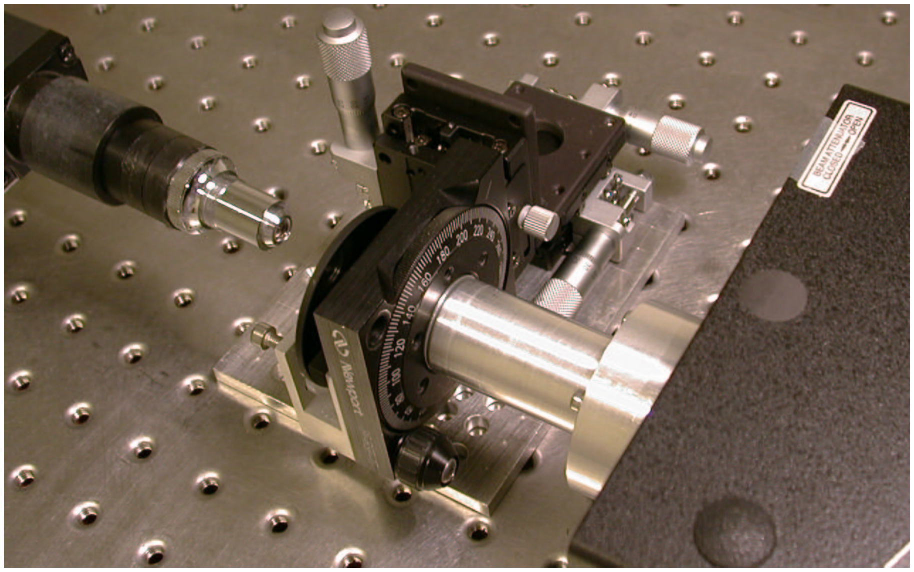

Figure 5.19: Mechanical and optical setups used to center the DOE prototype with respect to the laser beam.

was designed to allow four degrees of freedom: translation along X, Y and

Z axis (with high precision translation stages) and rotation θ along the Z axis (high precision rotation stage). As a result, the diffractive element can be shifted with respect to the laser beam using those degrees of freedom. The alignment tool was furthermore designed to include the DOE focusing lens, so the light distribution generated by the beam shaper can be checked in a plane localized at $Z = f'$ behind the focusing lens. To get a real time image of the reconstructed pattern, we have used a CCD camera that gives a magnified view of the reconstructed pattern (see Fig. 5.19). The camera is connected to a computer via a frame grabbing system; it is then possible to get a real time intensity profile of the reconstructed pattern. This alignment tool is quite efficient since it is directly possible to visualize the effects of a shift or rotation of the DOE over the reconstructed pattern profile. We are going to use that alignment setup to align the beam shaper in the assembly step as well as to check its sensitivity to input laser beam misalignments.

To complete the assembly step all we have to do is to adjust the four micrometer screws corresponding to the four degrees of freedom to get the best possible reconstructed pattern on the computer screen (see Fig. 5.20). Once the best reconstructed profile has been obtained, we have to lock the DOE onto its supporting part (see Fig. 5.18) without any mispositioning. This will be realized with UV–curing glue. Some liquid glue is dropped between the

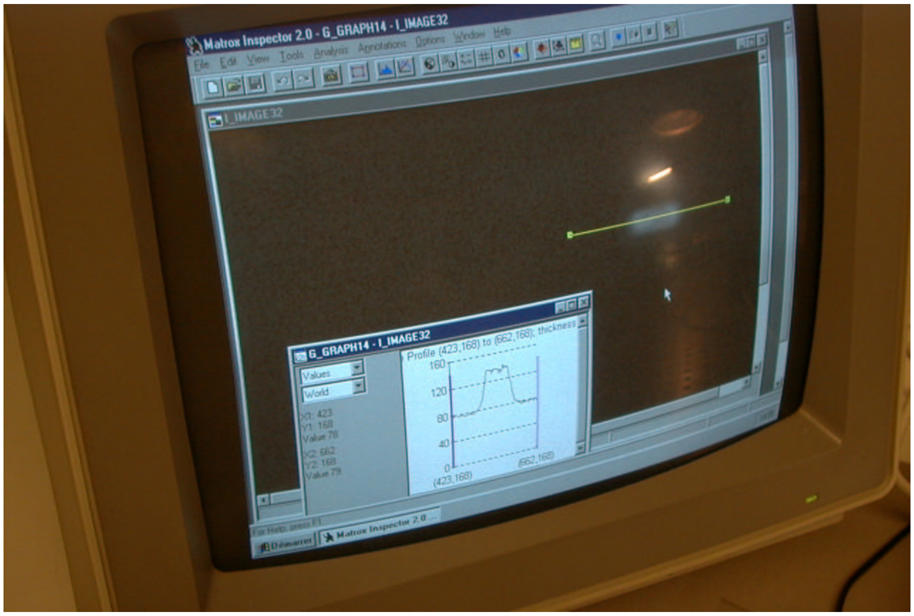

Figure 5.20: Frame grabbing system allowing real time analysis of the light intensity distribution in the image plane.

DOE holder and the positioning part and immediately UV exposed. Unlike the use of tightening screws, this introduce no drift in the position of the DOE holder.

So we have now realized our shaped laser light source of figure 5.18. The diffractive beam shaper and its focusing lens are locked onto the laser head package; it can easily be transported from a setup to another one without any alignment problems.

5.6.2 Measured performances

Now that the diffractive beam shaper is realized and that we have designed a specific alignment and testing mechanical setup, it is possible to compare simulated DOE performances of section 5.4.3 to the real ones.

5.6.2.1 Diffraction efficiency

Diffraction efficiency is defined as the energy ratio in the desired diffraction order (usually the first one) over the total energy (i.e. the input beam power). In this case we are not going to use any focusing lens since it would lead to a reconstructed plane with dimensions too small to be able to use the power meter detector. So we are going to observe diffraction orders in the far field

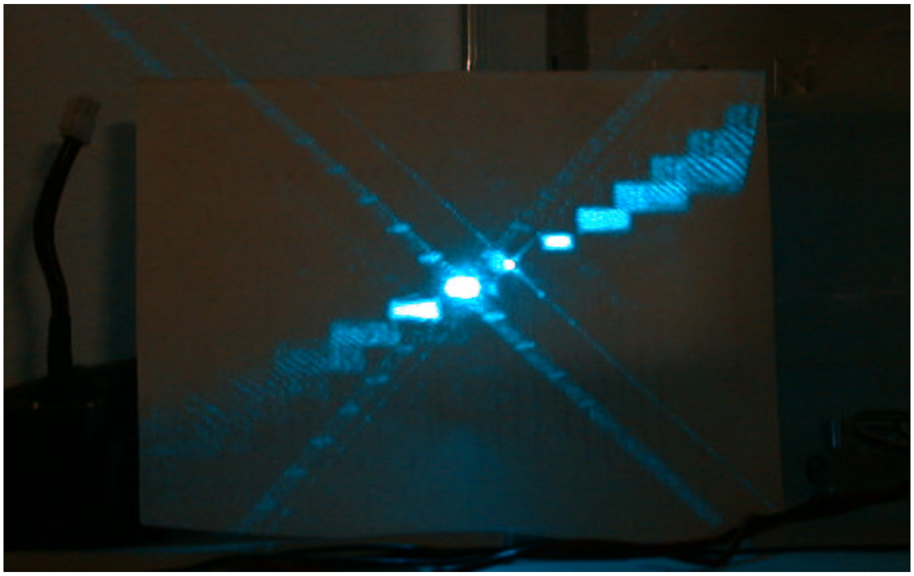

Figure 5.21: Far field (i.e. no focusing lens) observation of light diffracted by the beam shaper for diffraction efficiency measurement.

by projection onto a laboratory wall (see Fig. 5.21). In that case dimensions of the rectangle reconstructed in the first order (about 17mm×6mm) are enough to use the power meter detector. This leads to results of table 5.2.

The measured high diffraction efficiency of 82.5% in the first order means that the theoretical maximum depth of $h_{max} = \frac{\lambda}{n-1}$ was well realized during the development step (see section 5.5). All other orders are weak, stray light should therefore be very limited. The remaining 9.2% of energy that are missing in the table above are due to higer orders, stray light and Fresnel losses.

Diffraction order	Diffraction efficiency
-2	1.3%
-1	2.2%
0	3.5%
+1	**82.5%**
+2	1.3%

Table 5.2: Measured diffraction efficiency.

This very enlarged image of the reconstruction plane is also useful to check that no overlapping of higher orders onto the first one occurs. Examining Fig. 5.21 p. 109 and Fig. 5.6 p. 94, it can be noted that interferences between high diffraction orders (4, 5, 6...) that are experimentally seen on Fig. 5.21 were also predicted by simulation of Fig. 5.6.

5.6.2.2 Dimensions

Dimensions of the rectangular reconstructed intensity distribution depend both on sampling grid spacing in image plane $p' = \frac{\lambda f}{Np}$ (see §3.3), and on (α, β) parameters of the analytical phase function formulation derived in section 4.3.2. Although it has already been checked using the available propagators of our simulation software (see §5.4.3), it is still necessary to get a real measured value. This can easily be done using the mechanical alignment setup depicted Fig. 5.20 and Fig. 5.19). Knowing the magnification (×8.4) of the microscope objective used with the camera and the camera pixel size (11μm×11μm), it is possible to get the real length of profiles measured in the reconstruction plane. As represented Fig. 5.20, the frame grabber image processing software allows measurement of length in pixels; 80 pixels for the vertical profile and 27 pixels for the horizontal one. Once calibrated to the real dimensions we get 107μm horizontally and 35μm vertically. This exactly matches specifications of the beam shaper defined in table 5.1 of page 87.

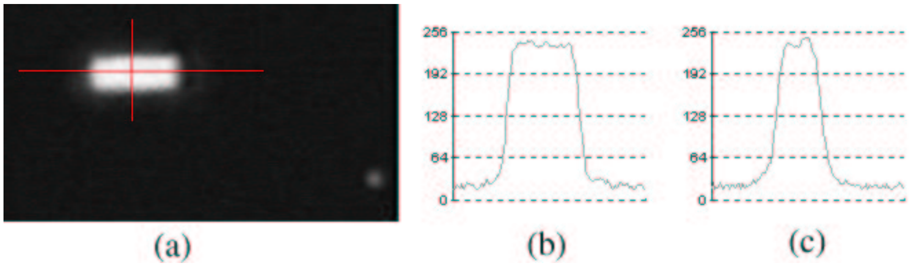

(a) (b) (c)

Figure 5.22: Magnified image of the measured light distribution in the image plane (a) taken by the mechanical and optical setup represented Fig. 5.19. Measured horizontal profile (b) shows a good uniformity whilst measured vertical profile (c) is rather rough.

5.6.2.3 Uniformity

We have seen in §5.2 that the beam shaper specifications require uniformity to be as good as possible. Throughout the whole design process we have taken care to use smooth analytical functions only and, not to introduce any dislocation which could lead to Speckle noise. So, we are now going to check and quantify the uniformity of the reconstructed intensity distribution. This will be done along the horizontal axis which is the most critical for our application. Using the setup represented Fig. 5.20, we take several horizontal profiles (see Fig. 5.23) to evaluate the uniformity along the horizontal axis. We measure a uniformity between 4% and 7.3% depending on the selected profile. This result is a really satisfying one and should be enough to allow accurate characteriztion of white blood cells.

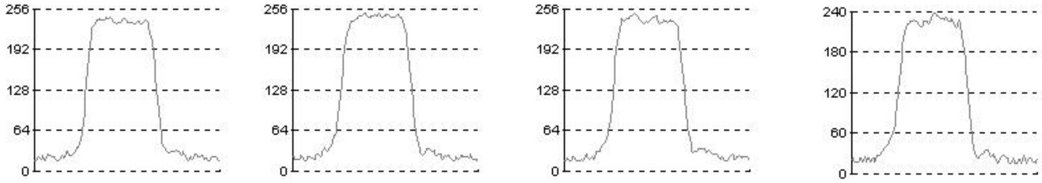

Figure 5.23: Horizontal profiles taken for measurement of the reconstructed intensity distribution uniformity.

5.6.2.4 Depth of field

We have also seen in section 5.2 that our blood cell counting application requires the depth of field to be at least ±20μm. According to the simulated results of section 5.4.3, that constraint should be satisfied. This is what we are going to check.

This parameter will also be measured using the mechanical setup represented figures 5.19 and 5.20. As seen on Fig. 5.19, the camera is mounted on high precision translation stage along the Z axis. It is then possible to accurately shift the camera along that axis. This is all we need to get the depth of field.

So the depth of field is determined by slightly shifting the camera along the Z axis and observing the effects on horizontal and vertical profiles flatness. As already stated in section 5.4.3, we try to find extreme positions where the horizontal profile still has an acceptable uniformity. This leads to the value of 550μm.

It is interesting to note that the experimentally measured depth of field of 550μm is very close to the simulated value of 500μm determined by the simulation software (see §5.4.3).

5.6.2.5 Misalignments sensitivity

The last parameter that has to be checked is DOE sensitivity to input laser beam misalignments. We already have a rough idea of this parameter value thanks to the simulated results of section 5.4.3. It is however necessary to measure the real sensitivity since, as stressed in §5.4.3, tolerancing is the cornerstone of any mass produced system.

We are going to use the mechanical alignment setup represented Fig. 5.19 and 5.20 to measure misalignment sensitivity. This mechanical setup was designed to shift the DOE along the X and Y as well as for real time monitoring of the reconstructed plane. So it will be quite easy to measure and quantify misalignment sensitivity using this setup. From the position that gives the best reconstructed rectangular intensity distribution, we are going to shift the DOE with the high precision translation stages (see Fig. 5.19). Observing the corresponding profiles with the frame grabber system (see Fig. 5.20), we stop shifting the DOE when the reconstructed profile uniformity drops. So se find that our beam shaper can handle horizontal misalignments of 50μm and vertical misalignments of 60μm with no severe changes in the uniformity of the reconstructed light distribution. Comparing those measured results to the simulated ones, it appears that real tolerances are much more relaxed than the simulated ones.

This ends the section dedicated to the test of the diffractive beam shaper prototype fabricated by Chalmers University from data we have generated. Thanks to the specific mechanical alignment setup we have designed, we have seen that real performances of our beam shaper match the expected ones.

5.7 Conclusion

In that chapter we have first analyzed constraints associated to our optical blood cell counting setup. From those constraints we have defined specifications the beam shaper will have to fulfil. We have then used diffractive optics design methods proposed in earlier chapters to synthesize the flat top diffractive beam shaper according to specifications mentioned above. We have then extensively used the simulation software we have designed to get an overview of our beam shaper performances, and then track potential problems before the diffractive component is realized. Simulated results were found to match the required specifications, so beam shaper prototypes were realized. Those prototypes have thoroughly been tested and measured performances were found to match the expected ones.

We, however, have to stress that the real way we have designed our diffractive beam shaper is not exactly the one presented above. What has been presented could lead to the thought that only one prototype was realized. In fact, five series each containing two to four prototypes were fabricated at Chalmers University. Between those series the proposed design methods and specifications were modified to take into account problems encountered during the test of previous prototypes. For instance, when the first prototype was tested, we realized that the off–axis, although enough to avoid order overlapping, was too low to clearly separate the reconstructed pattern from noise. Other design parameters such as rectangle dimensions or synthesis method have been adjusted between fabrication of series of prototypes. We have also realized that fabrication–related parameters had to be modified. The first two series of prototypes had 1024×1024 pixels whereas the next ones had 2048×2048 pixels so a much smoother phase function. Moreover the development step was also much more carefully controlled for the latest series than for the first once.

At the beginning of this chapter we have stressed that only performances of the single, isolated, diffractive beam shaper optical component will be considered. Now that we have thoroughly analyzed our diffractive beam shaper behavior, we are going to insert this optical component in the overall optical blood cells characterization setup described in chapter 1. So, unlike this one, the next chapter will be dedicated to the study of the entire optical system performances.

Chapter 6

Integration and validation

In the present work we have proposed a design for a diffractive beam shaper especially adapted to blood cell differentiation. As explained in chapter 1, this diffractive beam shaper will a part of an optical blood cell characterization system integrated in future blood cell analyzers.

In previous chapters 3 and 4 we have introduced physics of diffraction and diffractive optics technology. We have proposed a design for this beam shaper according to specifications required by the application. The beam shaper was then realized and tested as an isolated optical component. In that chapter we are going to check performances of the overall optical blood cell characterization system.

6.1 Introduction

In chapter 5 we have synthesized and realized our diffractive beam shaper prototypes. Performances of that beam shaper have thoroughly been analyzed in section 5.6. However the beam shaper was considered as a stand alone optical component, only intrinsic performances of the DOE were analyzed.

In that chapter we are going to consider the overall optical blood cell characterization system represented Fig. 6.1. We are first going to analyze problems raised by the integration and alignment of the beam shaper in the final optical system. We are next going to examine performances of this optical system, that is, its abilities to distinguish between white blood cells sub–populations. Finally, those results will be analyzed and compared with other analyzer results.

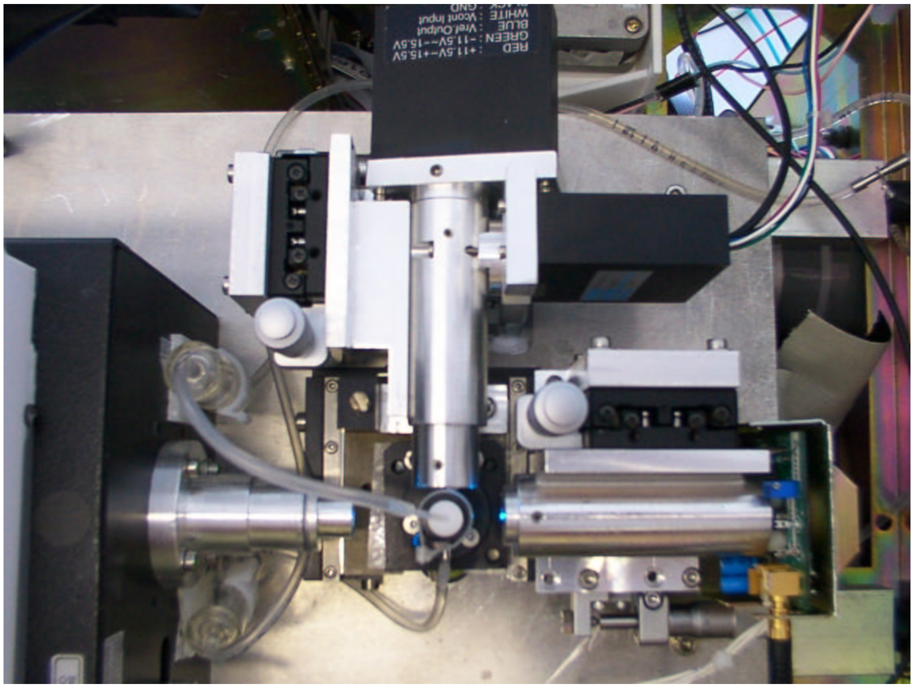

Figure 6.1: Overview of the blood cell differentiation final optical system.

6.2 Integration of the DOE in the final optical system

Mechanical integration of DOE prototypes in larger optical setups has already been discussed in section 5.6. We have seen that the best way to keep a rugged laser–DOE alignment and a versatile laser source is to lock the DOE to the laser head package (see Fig. 5.17). Since this mechanical arrangement has proven its utility when DOE performances were tested, we are going to keep it in the final setup.

The final optical setup depicted Fig. 6.1 also requires another critical alignment operation. We have already mentioned in chapter 1 and in section 5.2 that blood cells are transported by a water stream of 40μm cross section. To take part of the DOE flat top profile, the stream has to be positioned in the depth of field range of the reconstructed plane. This operation is much more tricky as it could seem at the first glance. The problem comes from the fact that energy density is not maximum at the reconstructed plane (see Fig. 5.8 p. 96). So it is not possible to shift the stream (i.e. the flowcell) until we get the highest signal amplitude onto the detector: this would lead to an alignment of the stream at the focus of the Fourier lens but not onto the DOE reconstructed plane (see Fig. 5.8).

The most accurate way to align the stream onto the reconstructed plane would be to use an optical system that images both the reconstructed rectangular intensity distribution and the stream with a very short depth of focus. Therefore, we propose to use a ×20 microscope objective to visualize the stream on a screen. This provides both the required high magnification and small depth of focus. If rectangle and stream are both seen at the focus on the screen of figure 6.2, we are then sure that they are also in the same object plane: the DOE reconstructed one.

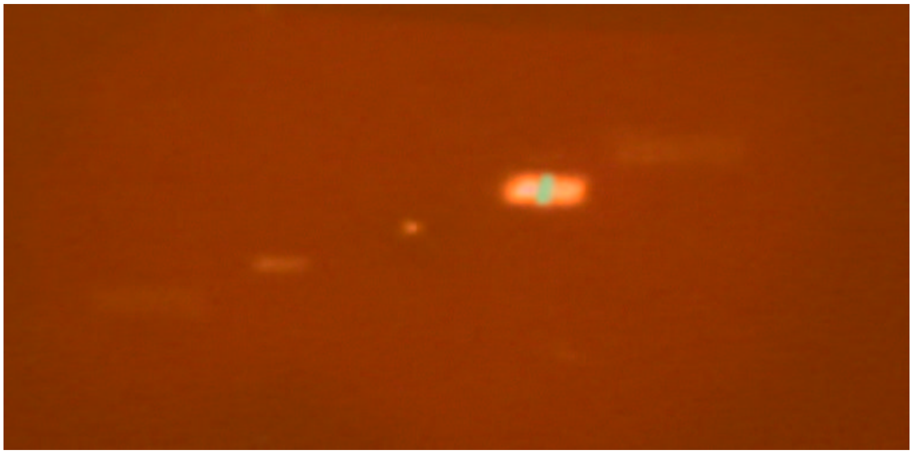

Figure 6.2: The water stream is dyed with Fluoresceine that emits strong green radiations when excited with the 488nm ray of an Argon laser. A magnified image of the measurement point is used to adjust the water stream onto the rectangular light distribution.

This is however not that simple: the stream as well as the surrounding sheath that are flowing in the flow cell are composed of salt water (see Fig. 2.11 and Fig. 2.12). It is therefore impossible to visualize it. To overcome that problem we propose to dilute either alcohol or Fluoresceine in the stream to visualize it. If alcohol is diluted in the stream salt water, the index will be changed and the circular stream cross section will create a lens effect deviating incoming light. This method is very efficient to get a rough alignment in cases where stream is very far (either transversally or longitudinally) from the reconstructed rectangle. It is obvious that this method can not lead to accurate positioning of the flow since it only relies on the way incoming light is deviated. To get an exact alignment, we propose to dilute a specific dye (fluoresceine) in the stream. When excited by the 488nm ray of an Argon laser, fluoresceine emits a strong green fluorescent radiation. All we have to do is to fine–adjust the previous alignment so that both blue rectangle and green line are in focus at the screen (see Fig. 6.2). If those two images are in focus at the screen plane, it involves they are also in the same object plane since the depth of focus of our alignment system was chosen to be very short.

Once the stream that transports blood cells has been aligned onto the DOE reconstructed rectangle, the microscope objective of Fig. 6.2 is removed. We also propose the use fluoresceine to align forward scatter and side scatter detection optics. In that case we adjust detection optics to be able to see an image of the stream onto the detector plane.

6.3 Validation

Throughout this work we have proposed a globally optimized optical system dedicated to blood cell differentiation. In chapter 1 we have mentioned that two optical functions are realized in the global setup: blood cell illumination and light–blood cell interaction detection. We have stressed that our work will focus on the first optical function. Detection of light–blood cell interactions is actually realized using standard optical systems, enhancements will be considered in future work.

We have seen in chapter 5.2 that the light intensity distribution has to fulfil all constraints defined in table 5.1 to allow differentiation of blood cells. The light intensity distribution at measurement point should be rectangular ($100\mu m \times 30\mu m$) and as uniform as possible; in that case drift of particle position inside the stream will have no more effect on the light–blood cell interaction intensity. Table 5.1 furthermore specifies that rays at measurement point have to be tilted of less than 1 deg to allow measurement of diffraction in the forward scatter direction (see §5.2.5).

The above constraints have been validated in section 5.6 where our diffractive beam shaper has been tested as a stand alone optical component. Now the beam shaper has been integrated in the overall optical system and aligned with respect to the other optical components, we are going to validate the behavior of the whole system.

6.3.1 Validation based on calibrated latex beads

In order to validate the stability and accuracy of the overall optical system, we propose to use calibrated latex beads. Those latex beads are opaque spheres with calibrated diameters (diameter CV is less than 0.1%). We propose to measure the light diffracted by those beads in forward scatter direction (see §2.3.2). This parameter is linked to the diameter of the diffracting particle [2][1][11].

In a first step, we are going to measure the forward scatter signal using the optical setup we proposed and using standard optical system. In this case the flowcell has perfectly been aligned at the center of the flowing stream. Observing figure 6.3a-1 and a-2, it appear that results given by the two setups are very close. Now, keeping the same setup, we are going to introduce a small misalignment of the flowcell on both optical systems. Those misalignments can not be avoided in standard operating conditions of those analyzers. It corresponds to vibrations or chocks we always encounter in industrial environment. Figures 6.3b, c and d were obtained for progressive transversal misalignments (5μm, 20μm and 35μm) of the flowing stream with respect to the rectangular intensity distribution. Results obtained with the proposed optical setup show no variation of the detected forward scatter intensity (see Fig. 6.3b-1 to d-1), whereas intensity clearly falls when shifting the flowcell on the standard optical system (see Fig. 6.3b-2 to d-2).

Those results have demonstrated that the optical setup we have proposed allows the measurement of diffraction by a particle in the forward scatter direction (1deg to 9deg, see §2.3.2). Moreover, unlike with the standard system, the proposed setup shows no sensitivity to flowcell misalignments or particle position fluctuations inside the flowing stream.

6.3.2 Validation based on human blood

The validation realized above is the most critical case. Latex beads are identical one to each other (diameter CV is less than 0.1%), so any lack of uniformity in the illumination setup would immediately lead to a broadening of curves represented Fig. 6.3. The situation will be quite different in the last validation step that relies on tests performed with human blood. Blood cells have a so complex shape (considering both cytoplasm and nucleus) that we can not expect results to be as obvious as those obtained with latex beads. However, we are going to measure forward scatter, side scatter and fluorescence of a blood sample as represented Fig. 6.4. Examining Fig. 6.4, it is obvious that all blood cell sub–populations differentiated by the standard optical system (see Fig. 6.4b) are also distinguished by the setup we propose (see Fig. 6.4a). Tests performed over large number of human bloods have confirmed that the proposed setup is adapted to blood cell differentiation. Furthermore, we have also checked using human bloods that the proposed system has no sensitivity to small transversal misalignments of the flowcell.

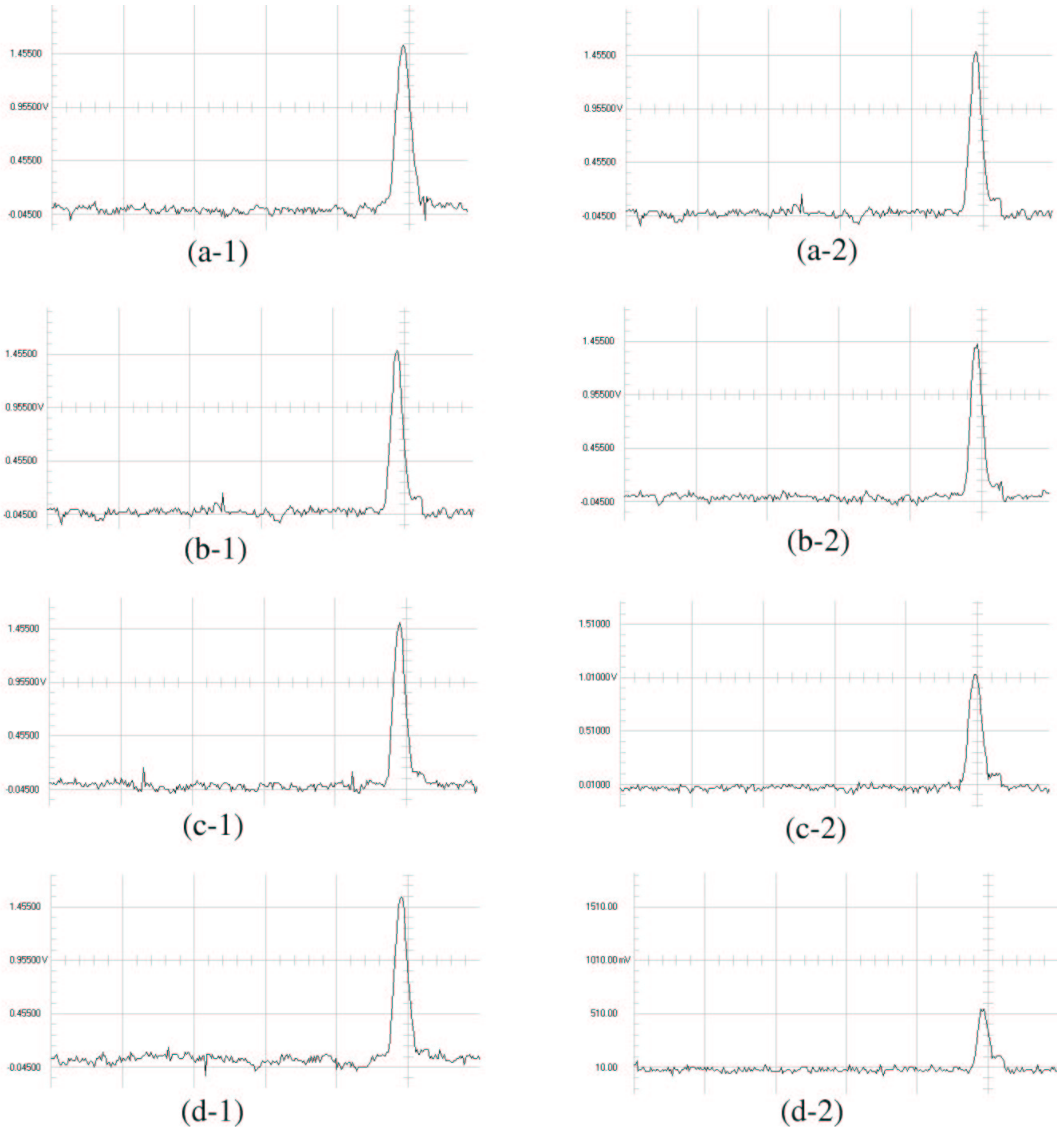

(a-1) (a-2)

(b-1) (b-2)

(c-1) (c-2)

(d-1) (d-2)

Figure 6.3: Measured effects of flow cell misalignments onto the detected forward scatter signal amplitude with the proposed system (left column) and with a standard setup (right column). Flowcell is: centered with respect to the incoming laser beam (row a); 5μm transversally shifted (row b); 20μm shifted (row c) and 30μm shifted (row d).

6.4 Conclusion

This chapter was dedicated to validation of performances of the overall optical blood cell differentiation system. The beam shaper we have proposed in

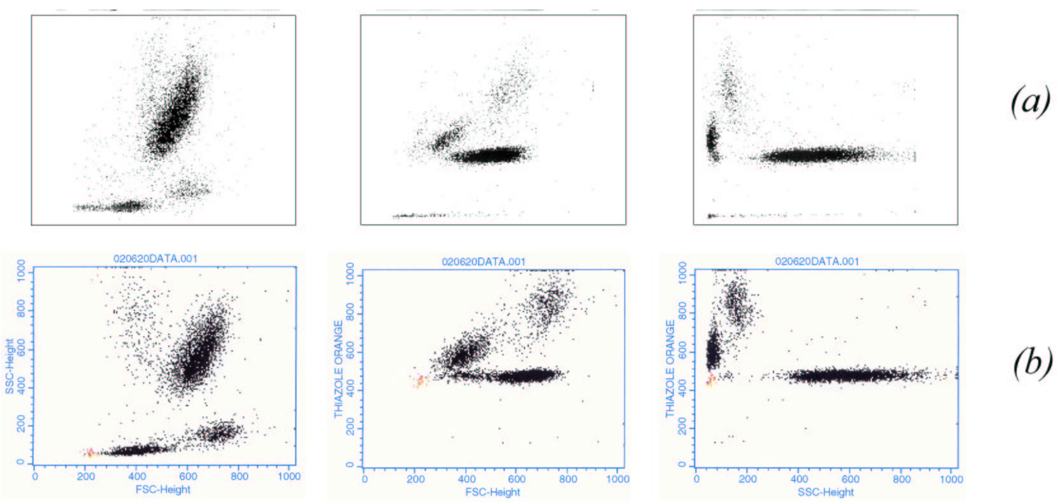

Figure 6.4: Results of human white blood cell optical characterization by the proposed system (a), by a standard setup (b).

previous sections is no more considered as a stand alone optical component but as a part of the more complex optical system we have to test.

We have first proposed an optical method to align the diffractive beam shaper with respect to the other optical components. We have then tested performances of the whole optical system using calibrated latex beads and human blood. As expected, we found that alignment tolerances of the flowcell with respect to the incoming laser beam were relaxed thanks to the use of the proposed diffractive beam shaper. Furthermore, comparing with standard optical system, we have demonstrated that the proposed system is adapted to blood cell differentiation.

It is however important to stress that, unlike in the previous chapters, results obtained in this chapter reflect the behavior of the full system. Other parameters like detection optics, electronics and data processing do have a strong influence on results represented Fig. 6.4. Throughout the following chapter we are going to highlight the fact that enhancements we have proposed are the first step toward more accurate optical blood cell characterization setups.

Chapter 7

Conclusion

The goal of the present work is to enhance performances of optical blood cells differentiation systems embedded in future blood cell analyzers. Differentiation between blood cell sub–populations relies on their interaction with light. As described in chapter 1 and in section 2.3.2, two different optical functions can be distinguished in those systems: blood cell illumination and light–cell interaction detection. Throughout that work we have focused on the illumination, that is, the light intensity distribution at measurement point. We have seen that the light intensity distribution is not optimal in standard optical setups since any drift in the blood cell position leads to a loss of precision in measured parameters (see chapter 1 and section 2.3.2).

We have therefore proposed an innovating design that ensures accurate and stable measurements whatever blood cells position are. This design relies on a diffractive beam shaper that has been globally optimized taking into account specific constraint of blood cell counting. This diffractive beam shaper generates a flat top intensity pattern at the measurement point which is the optimal light distribution for our application.

We have then analyzed optical constraints associated to blood cell differentiation and diffractive optics design. Taking into account and retaining compromises between those two kind of constraints, we have designed a diffractive beam shaper especially adapted to blood cell differentiation. Prototypes have been realized and integrated in an overall optical blood cell characterization system. As expected, validation steps have proven particle position inside the flowing stream have no more impact onto the detected signal amplitude.

In section 5.4 we have considered the possibility of using a telescope to enlarge the laser beam waist. This solution was not retained because of the extra costs (lenses, alignments) it would involve. However, the use of a telescope would lead to a better resolution and uniformity in the DOE reconstructed plane. This would also relax alignment sensitivity of the diffractive beam shaper. Although the actual setup is satisfying for actual applications, the use of a telescope would furthermore enhance measurement stability and accuracy. This could be useful to characterize finer blood cell details in very high range analyzers.

As explained in chapter 1, the overall optical blood cells differentiation system is composed of two functions: blood cell illumination and light–blood cell interaction detection. The beam shaper we have proposed enhance performances of the first function. But the second one still has to be improved (optics, electronics, signal processing, ...). This will be our working theme for the next years.

By synthesizing a diffractive element especially adapted to hematology, we have facilitated measurement of optical parameters used in standard blood cell characterization. Those parameters, presented in section 2.3.2, have been known for a long time since the required technology is rather basic. It would be interesting to wonder if other parameters such as non–elastic scattering (Raman) or multi-wavelength excitation wouldn't lead to a more accurate characterization of blood cells.

Appendix A

Helmholtz–Kirchhoff integral theorem

As exposed in section 3.2.4, the Helmholtz–Kirchhoff diffraction integral is the basement of any scalar diffraction calculations. All propagators we have studied and implemented in that work rely on the Helmholtz–Kirchhoff diffraction integral. This relation will be presented here to give an overview of approximations that are made when deriving diffraction equations.

The following calculations might appear pretty theoretical and somehow out of the scope of that work. However we think that diffraction formulations can not be considered as "recipes" applied to diffractive optics design. For that reason, before studying diffraction integrals and their associated propagators, we have thoroughly examined the Helmholtz–Kirchhoff integral to get a better understanding of diffraction integrals insights.

The basement of Kirchhoff–Fresnel and Rayleigh–Sommerfeld diffraction theory is the Green's theorem that expresses the optical disturbance U at a point P_0 in terms of its values on a surface S.

Green's theorem 1 *If U and G are continuous and if their first and second derivatives are single–valued over the surface S bounding the volume V*

$$\iiint_V \left(U\nabla^2 G - G\nabla^2 U\right) dv = \iint_S \left(U\frac{\partial G}{\partial n} - G\frac{\partial U}{\partial n}\right) ds$$

where n is the outward normal of surface S.

According to Huygens principle, the chosen auxiliary Green's function[1] is

$$G(P_1) = \frac{1}{r_{01}} \mathrm{e}^{-j\vec{k}\overrightarrow{r_{01}}}$$

---

[1] It can be shown (with consirable difficulties) that the final result is independant of the choice of the Green's function G.

where $\overrightarrow{r_{01}} = \overrightarrow{P_0P_1}$. The auxiliary function G represents a spherical wave expanding from P_0. Since all functions mentionned in Green's theorem are supposed to be continuous, the P_0 singularity (i.e. $r_{01} = 0$) of G has to be removed from integration domain. The new surface S' is the same as S (see Fig. A.1) except we remove the sphere S_ϵ of radius ϵ so $S' = S + S_\epsilon$. Keeping in mind that both U and G have to obey to the Helmholtz equation

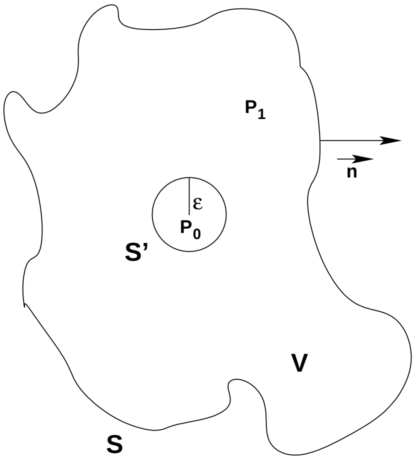

Figure A.1: Surfaces of integration for Green's theorem $S = S' + S_\epsilon$.

$$\begin{cases} (\nabla^2 + k^2)\, U = 0 \\ (\nabla^2 + k^2)\, G = 0 \end{cases} \qquad \begin{cases} \nabla^2 U = -k^2 U \\ \nabla^2 G = -k^2 G \end{cases}$$

the first integral term of Green's theorem 1 can be re–written

$$\iiint_{V'} \left(U \left(-k^2 G\right) - G \left(-k^2 U\right) \right) dv = \iiint_{V'} \left(UG - GU \right) dv = 0$$

which means that the second term of Green's theorem 1 also has to be zero.

$$\begin{align} &\iint_{S'} \left(U\frac{\partial G}{\partial n} - G\frac{\partial U}{\partial n} \right) ds \tag{A.1} \\ &= \iint_{S} \left(U\frac{\partial G}{\partial n} - G\frac{\partial U}{\partial n} \right) ds \quad + \iint_{S_\epsilon} \left(U\frac{\partial G}{\partial n} - G\frac{\partial U}{\partial n} \right) ds \tag{A.2} \\ &= A \qquad\qquad\qquad\qquad\qquad\qquad + B \tag{A.3} \\ &= 0 \tag{A.4} \end{align}$$

Now let's evaluate the second member (i.e. B) of the previous equation (A.1). Since surface S_ϵ is a sphere it's then obvious (see Fig. A.1) that vectors $\vec{n}$ and $\overrightarrow{r_{01}}$ are colinear. Moreover G represents a spherical expanding wave, the wave vector $\vec{k}$ is colinear to the normal vector $\vec{n}$ of the sphere so

$$\begin{aligned}
\frac{\partial G}{\partial n} &= \frac{\partial G}{\partial r_{01}} \cdot \frac{\partial r_{01}}{\partial n} \\
&= \frac{\partial}{\partial r_{01}} \left(\frac{1}{r_{01}} \mathrm{e}^{jkr_{01}} \right) \cdot \frac{\partial r_{01}}{\partial n} \\
&= \left[\frac{1}{r_{01}} \frac{\partial}{\partial r_{01}} \left(\mathrm{e}^{jkr_{01}} \right) + \mathrm{e}^{jkr_{01}} \frac{\partial}{\partial r_{01}} \left(\frac{1}{r_{01}} \right) \right] \cdot \frac{\partial r_{01}}{\partial n} \\
&= \left[\frac{1}{r_{01}} jk\mathrm{e}^{jkr_{01}} + \frac{1}{r_{01}^2} \mathrm{e}^{jkr_{01}} \right] \cdot 1 \\
&= \frac{1}{r_{01}} \mathrm{e}^{jkr_{01}} \left(jk - \frac{1}{r_{01}} \right)
\end{aligned}$$

so replacing $\frac{\partial G}{\partial n}$ by its value in the second member (i.e. B) of Eq. (A.1) gives

$$\mathrm{B} = \iint_{S_\epsilon} \left[U \frac{1}{r_{01}} \mathrm{e}^{jkr_{01}} \left(jk - \frac{1}{r_{01}} \right) - \frac{1}{r_{01}} \mathrm{e}^{jkr_{01}} \frac{\partial U}{\partial n} \right] ds$$

where ds represents the elementary surface of the sphere S_ϵ of radius ϵ. Using the solid angle $\Omega = \frac{S}{\epsilon^2}$ which value is, by definition, 4π over the full surface S, previous equation ca be re–written

$$\mathrm{B} = \int_0^{4\pi} \left[U \frac{1}{r_{01}} \mathrm{e}^{jkr_{01}} \left(jk - \frac{1}{r_{01}} \right) - \frac{1}{r_{01}} \mathrm{e}^{jkr_{01}} \frac{\partial U}{\partial n} \right] \epsilon^2 d\Omega$$

The radius ϵ of the sphere S_ϵ can be taken infinitely small, so taking the zero–limit of the previous relation gives

$$\begin{aligned}
\lim_{\epsilon \to 0} \mathrm{B} &= \lim_{\epsilon \to 0} \int_0^{4\pi} \left[U \frac{1}{\epsilon} \mathrm{e}^{jk\epsilon} \left(jk - \frac{1}{\epsilon} \right) - \frac{1}{\epsilon} \mathrm{e}^{jk\epsilon} \frac{\partial U}{\partial n} \right] \epsilon^2 d\Omega \\
&= \int_0^{4\pi} \left[\lim_{\epsilon \to 0} jk\epsilon U \mathrm{e}^{jk\epsilon} - \lim_{\epsilon \to 0} U \mathrm{e}^{jk\epsilon} + \lim_{\epsilon \to 0} \epsilon \mathrm{e}^{jk\epsilon} \frac{\partial U}{\partial n} \right] d\Omega \\
&= \int_0^{4\pi} \left[0 - U(P_0) + 0 \right] d\Omega \\
&= 4\pi U(P_0)
\end{aligned}$$

Reporting the result $\mathrm{B} = 4\pi U(P_0)$ in equation (A.1) gives the final form of *the integral theorem of Kirchhoff* that express the optical disturbance at point P_0 in terms of its values over the surface S

$$U(P_0) = \frac{1}{4\pi} \iint_S \left[U \frac{\partial}{\partial n} \left(\frac{1}{r_{01}} \mathrm{e}^{jkr_{01}} \right) - \frac{1}{r_{01}} \mathrm{e}^{jkr_{01}} \frac{\partial U}{\partial n} \right] ds \tag{A.5}$$

$$U(P_0) = \frac{1}{4\pi} \iint_S \frac{1}{r_{01}} \mathrm{e}^{jkr_{01}} \left[U \left(jk - \frac{1}{r_{01}} \right) - \frac{\partial U}{\partial n} \right] ds \tag{A.6}$$

Bibliography

[1] H.M. Shapiro. *Practical Flow Cytometry.* Wiley–Liss, third edition.

[2] M.R. Melamed. *Flow Cytometry and Cell Sorting.* Wiley–Liss, second edition, 1990.

[3] G.C. Salzman and J.M. Crowell. Cell classification by light scattering: identification and separation of unstained leukocytes. *Acta Cytologica*, 19(4):374–377, 1975.

[4] C.F. Mattern, F.S. Brackett, and B.J. Olson. Determination of number and size of particles by electrical gating: blood cells. *J. Appl. Physiol.*, 10:56, 1957.

[5] W. Coulter. High speed automatic blood cell counter and cell size analyzer. *Proc. Natl. Electronics Conf.*, 12:1034, 1956.

[6] M. Bartholdi and G.C. Salzman. Differential light scattering photometer for rapid analysis of single particle in flow. *Appl. Opt.*, 19(10):1573–1581, 1980.

[7] G. Brecher, M. Schneiderman, and C.Z. William. Evaluation of electronic red blood cell counter. *Am. J. Cli. Path.*, 26:1034, 1956.

[8] R. Drezek, A. Dunn, and R. Richards-Kotum. Light scattering from cells: finite difference time–domain simulations and goniometric measurements. *Appl. Opt.*, 38(16):3651–3661, 1999.

[9] M. Hammer and D. Schweitzer. Single scattering by red blood cells. *Appl. Opt.*, 37(31):7410–7418, 1998.

[10] T. Sharpless and F. Traganos. Flow cytometry: discrimation between single cells and cell aggregates by direct size measurements. *Acta Cytologica*, 19(6):577–581, 1975.

[11] Max Born and Emil Wolf. *Principles of Optics.* Cambridge University Press, seventh edition, 1999.

[12] B.R. Brown and A.W. Lohmann. Complex spatial filtering with binary masks. *Appl. Opt.*, 5:967, 1966.

[13] G. Tricoles. Computer generated holograms: an historical review. *Appl. Opt.*, 26(20):4351–4360, 1987.

[14] L.B. Lesem, P.M. Hirsh, and J.R. Jordan. The kinoform: a new wavefront reconstruction device. *IBM J. Res. Dev.*, 13:150–155, 1969.

[15] H. Dammann. Blazed synthetic phase–only holograms. *Optik*, 31:95–105, 1970.

[16] B. Veldkamp. Laser beam profile shaping with diffraction gratings. *Opt. Comm.*, 38(5):381–386, 1981.

[17] B. Veldkamp. Laser beam profile shaping with interlaced binary diffraction gratings. *Appl. Opt.*, 21(5):3209–3212, 1982.

[18] W. Chen. Design approachs for laser–diodes material processing using fibers and micro–optics. *Opt. Eng.*, 33:3662–3669, 1994.

[19] Jospeh W. Goodman. *Introduction to Fourier Optics.* McGraw–Hill, second edition, 1996.

[20] I. Raveh, E. Marom, and D. Mendlovic. Phase retrieval algorithm in the Fresnel domain. In SPIE, editor, *Congress of the International Commision for Optics*, volume 3749.

[21] N. Delen and B. Hooker. Verification and comparison of fast Fourier transformed–based full diffraction method for tilted and offset planes. *Appl. Opt.*, 40(21):3525–3531, 2001.

[22] E.W. Marchand and E. Wolf. *J. Opt. Soc. Am.*, 56:1712, 1966.

[23] A. Sommerfeld. *Optics.* New York, Academic Press, 1954.

[24] P.G. Rudolf, J.J. Tollet, and R.R. McGowan. Computer modeling wave propagation with a variation of the Helmholtz–Kirchhoff relation. *Appl. Opt.*, 29(7):998–1003, 1990.

[25] M. Totzeck. Validity of the scalar scalar Kirchhoff and Rayleigh–Sommerfeld diffraction theories in the near field of small phase objects. *J. Opt. Soc. Am.*, 8(1):27–32, 1991.

[26] J.A. Hudson. Fresnel–Kirchhoff diffraction in optical systems: an approximate computational algorithm. *Appl. Opt.*, 23(14):2292–2295, 1984.

[27] J.C. Heurtley. Scalar Rayleigh–Sommerfeld and Kirchhoff diffraction integrals: a comparison of exact evaluations for axial points. *J. Opt. Soc. Am.*, 63:1003, 1973.

[28] E.W. Marchand and E. Wolf. Comparison of the Kirchhoff and Rayleigh–Sommerfeld theories of diffraction at an aperture. *J. Opt. Soc. Am.*, 54:587, 1964.

[29] A. VanderLugt. Sampling of Fresnel transforms. In SPIE, editor, *Congress of the International Commision for Optics IV*, volume 1296.

[30] H. Hamam and J.L. de Brougrenet de la Tocnaye. Efficient Fresnel–transform algorithm based on fractional Fresnel diffraction. *J. Opt. Soc. Am. A*, 12(9):1920–1931, 1995.

[31] A.E. Sziklas and A.E. Siegman. Diffraction calculations using fast Fourier transform methods. *Proc. of the IEEE*, pages 410–412, 1974.

[32] R.N. Bracewell. *The Fourier Transform and its Applications.* McGraw–Hill, second edition, 1986.

[33] L. Onural. Sampling of the diffraction field. *Appl. Opt.*, 39(32):5929–5935, 2000.

[34] H.M. Ozaktas and D. Mendlovic. Fractional Fourier optics. *J. Opt. Soc. Am. A*, 12(4):743–751, 1995.

[35] Y. Zhang, B. Dong, B. GU, and G. Yang. Beam shaping in the fractional Fourier transform domain. *J. Opt. Soc. Am. A*, 15(5):1114–1120, 1998.

[36] F.M. Dickey and S.C. Holswade. *Laser Beam Shaping: Theory and Techniques.* Dekker, 2000.

[37] N. Delen and B. Hooker. Free–space beam propagation between arbitrarily oriented planes based on full diffraction theory: a fast Fourier approch. *J. Opt. Soc. Am. A*, 15(4):857–867, 1998.

[38] E. Nichelatti and G. Pozzi. Improved beam propagation method equation. *Appl. Opt.*, 37(1), 1998.

[39] J.J. Gribble and J.M. Arnold. Beam–propagation method ray equation. *Opt. Lett.*, 13(8):611–613, 1988.

[40] T. Dresel, M. Beyerlein, and J. Schweider. Design and fabrication of computer–generated beam–shaping holograms. *Appl. Opt.*, 35(23):4615–4621, 1996.

[41] H. Aagedal and F. Wyrowski. Analytical beam shaping with application to laser–diode arrays. *J. Opt. Soc. Am. A*, 14(7):1549–1553, 1997.

[42] N.C. Roberts. Beam shaping by holographic filters. *Appl. Opt.*, 28(1):31–32, 1989.

[43] O. Bryngdahl. Geometrical transformations in optics. *J. Opt. Soc. Am. A*, 64(8):1092–1099, 1974.

[44] J.N. Cederquist and A.M. Tai. Computer–generated holograms for geometric transformations. *Appl. Opt.*, 23:3099–3104, 1984.

[45] M. Duparré and M. A. Golub. Investigation of computer–generated diffractive beam shaper for flattening of single-modal CO_2 laser beams. *Appl. Opt.*, 34(14):2489–2497, 1995.

[46] M.A. Golub and M. Duparré. New diffractive beam shaper generated with the aid of e–beam lithography. *Opt. Eng.*, 35(5):1400–1405, 1995.

[47] N. Yoshikawa and T. Yatagai. Phase optimization of a kinoform by simulated annealing. *Appl. Opt.*, 33(5):863–868, 1994.

[48] M.S. Kim and C.C. Guest. Simulated annealing algorithm for binary phase only filters in pattern classification. *Appl. Opt.*, 29(8):1203–1208, 1990.

[49] M.A. Seldowitz, J.P. Allebach, and D.W.Sweeney. Synthesis of digital holograms by direct binary search. *Appl. Opt.*, 26(14):2788–2798, 1987.

[50] H.P. Herzig. *Micro–Optics.* Taylor&Francis, 1997.

[51] J. Turunen and F. Wyrowski. *Diffractive Optics for Industrial and Commercial Applications.* Akademie Verlag, 1997.

[52] R.W. Gerchberg and W.O. Saxton. A practical algorithm for the determination of phase from image and diffraction plane pictures. *Optik*, 35(2):237–246, 1972.

[53] J.R. Fienup. Iterative method applied to image reconstruction and to computer–generated holograms. *Opt. Eng.*, 19(3):297–305, 1980.

[54] F. Wyrowski and O. Bryngdahl. Iterative Fourier–transform algorithm applied to computer holography. *J. Opt. Soc. Am. A*, 5(7):1058–1065, 1988.

[55] M.T. Eismann, A.M. Tai, and J.N. Cederquist. Iterative design of a holographic beamformer. *Appl. Opt.*, 28(13):2641–2650, 1989.

[56] R.G. Dorch. Ping–Pong algrorithm for two–plane computer generated hologram display. *Appl. Opt.*, 33(5):869–875, 1994.

[57] G. Yang, B. Dong, B. Gu, and J. Zhuang. Gerchberg–Saxton and Yang–Gu algorithms for phase retrieval in nonunitary transform systems: a comparison. *Appl. Opt.*, 33(2):209–218, 1994.

[58] X. Tan, B. Gu, G. Yang, and B. Dong. Diffractive phase elements for beam shaping: a new design method. *Appl. Opt.*, 34(8):1314–1320, 1995.

[59] W.X. Cong, N.X. Chen, and B.Y. Gu. Beam shaping and its solution with the use of an optimized method. *Appl. Opt.*, 37(20):4500–4503, 1998.

[60] F. Wyrowski. Diffractive optical elements: iterative calculation of quantized, blazed phase structures. *J. Opt. Soc. Am. A*, 7(6):961–969, 1990.

[61] W. Däshner, M. Larsson, and S.H. Lee. Fabrication of monolithic diffractive optical elements by the use of e–beam direct write on analog resist and chemically assisted ion–beam etching step. *Appl. Opt.*, 34:2534–2539, 1995.

[62] W. Däshner, P. Long, R. Stein, C. Wu, and S.H. Lee. Cost–effective mass production of multilevel diffractive optical elements by use of a single optical exposure with a gray–level mask on high–energy beam–sensitive glass. *Appl. Opt.*, 36:4675–4680, 1997.

[63] S.M. Arnold. Electron beam fabrication of computer–generated holograms. *Opt. Eng.*, 24:803–807, 1985.

[64] M. Ekberg, M. Larsson, S. Hård, and B. Nilsson. Multilevel phase holograms manufactured by electron beam lithography. *Opt. Lett.*, 15:568–569, 1990.

[65] F. Nickolajeff and J. Bengtsson. Measuring and modeling the proximity effect in direct–write electron–beam lithography kinoforms. *Appl. Opt.*, 34(5):897–903, 1995.

[66] B.R. Frieden. Lossless conversion of a plane laser wave to a plane wave of uniform irradiance. *Appl. Opt.*, 4(11):1400–1403, 1965.

[67] Y.S. Liu. *Sources, optics and laser micro–fabrication system for direct writing and projection mithography.* Academic Press, 1989.

[68] W. Lee. Method for converting a Gaussian laser beam into a uniform beam. *Opt. Comm.*, 36(6):469–471, 1981.

[69] P.W. Rhodes and D.L. Shealy. Refractive optical systems for irradiance redistribution of collimated radiation: their design and analysis. *Appl. Opt.*, 19(20):3545–3553, 1980.

[70] M. Santarsiero and R. Borghi. Correspondance between super–Gaussian and flattened Gaussian beams. *J. Opt. Soc. Am. A*, 16(1):188–190, 1999.

[71] C. Sheppard and S. Saghafi. Flattened light beams. *Opt. Comm.*, 132:144–152, 1996.

[72] W. Jiang, D. Shealy, and J. Martin. Design and testing of a refractive reshaping system. *Proc. SPIE*, 2000:64–75, 1993.

[73] D. Schafer. Gaussian to flat–top in diffraction far–field. *Appl. Opt.*, 36(6):9092–9093, 1997.

[74] S. Jahan and M. Karim. Refractive systems for Gaussian–to–uniform beam transformations. *Optics and Laser Technology*, 21(1):27–30, 1989.

[75] C. Han, Y. Ishii, and K. Murata. Reshaping collimated laser beams with gaussian profile to uniform profiles. *Appl. Opt.*, 22(22):3644–3647, 1983.

[76] J.R. Fienup. Phase retreival algorithms: a comparison. *Appl. Opt.*, 21:1698–1702, 1982.

[77] J. Turunen and A. Vasara. Kinoform phase relief synthesis: a stochastic method. *Opt. Eng.*, 28:1162–1167, 1989.

[78] R. Brauer, F. Wyrowski, and O. Bryngdahl. Diffusers in digital holography. *J. Opt. Soc. Am. A*, 8(3):572–578, 1991.

[79] S.H. Lee. *Computer–Generated Holograms and Diffractive Optics.* SPIE Press, 1992.

[80] V. Soiffer, V. Kotlyar, and L. Dosklovich. *Iterative Methods for Diffractive Optical Elements Computation.* Taylor&Francis, 1997.

[81] J.M. Huntley and J.R. Buckland. Characterisation of sources of 2π phase discontinuity in Speckle interferograms. *J. Opt. Soc. Am. A*, 12(9):1990–1996, 1995.

[82] H. Aagedal, S. Teiwes, and F. Wyrowski. Consequences of illumination wave on optical function of non–periodic diffractive elements. *Opt. Commun.*, 109:22–28, 1994.

[83] H. Aagedal, F. Wyrowski, T. Beith, and S. Taiwes. Theory of Speckles in diffractive optics and its application to beam shaping. *J. of Mod. Opt.*, 43(7):1406–1421, 1996.

[84] F. Wyrowski. Iterative quantization of digital amplitude holograms. *Appl. Opt.*, 28:3864–3870, 1989.

[85] J. Bengtsson. Direct inclusion of the proximity effects in the calculations of kinoforms. *Appl. Opt.*, 33(22):4993–4996, 1994.

[86] F. Wyrowski and O. Bryngdahl. Digital holography as part of diffractive optics. *Rep. Prog. Phys.*, pages 1481–1571, 1991.

[87] P.K. Katti and P.C. Mehta. Noise elimination technique in holography. *Appl. Opt.*, 15(2):530–533, 1976.

[88] F. Wyrowski and O. Bryngdahl. Speckle–free reconstruction in digital holography. *J. Opt. Soc. Am. A*, 6:1171–1174, 1989.

[89] Y. Chen, D. LI, and Y. Sheng. Beam–shaping element with reduced sensitivity to input variations. *Appl. Opt.*, 36(3):568–571, 1997.

[90] M. Rossi and T. Hessler. Stray–light effects of diffractive beam–shaping elements in optical systems. *Appl. Opt.*, 38(14):3068–3076, 1999.

[91] O. Bryngdahl. Optical map transfoms. *Opt. Commun.*, 10:164–169, 1974.

[92] C.C. Aleksoff, K.K. Ellis, and B.D. Neagle. Holographic conversion of a Gaussian beam to a near–field uniform beam. *Opt. Eng.*, 30:537–543, 1991.

[93] J. Amako, H. Miura, and T. Sonehara. Speckle–noise reduction on kinoform reconstruction using phase–only spatial light modulator. *Appl. Opt.*, 34:3165–3171, 1995.

[94] J.N. Mait. Understanding diffractive optics design in the scalar domain. *J. Opt. Soc. Am. A*, 12(10):2145–2158, 1995.

[95] T.H. Hessler, M. Rossi, R. E. Kunz, and M.T. Gale. Analysis and optimization of continuous relief diffractive optical elements. *Appl. Opt.*, 37(19):4069–4079, 1998.

[96] A.E. Siegman. *Lasers.* University Science Books, 1999.

[97] John C. Stover. *Optical Scattering: measurements and analysis.* SPIE Press, second edition, 1995.

[98] V. Tuchin. *Tissue Optics: Light Scattering Methods and Instruments for Medical Diagnostics.* SPIE Press, 2000.

[99] T. Sharpless and R. Melamed. Estimation of cell size from pulse shape in flow cytofluorometry. *The Journal of Histochemistry and Cytochemistry*, 24(1):257–264, 1976.

[100] B. Kress. *Optimisation du calcul et de la fabrication d'Eléments Optiques Diffractifs en vue de leur integration dans des micro-systèmes.* PhD thesis, Université Louis Pasteur (Strasbourg, France), 1997.

[101] S.H. Lee. *Diffractive and miniaturized Optics.* SPIE Press, 1994.

[102] F. Wyrowski. Design theory of diffractive elements in the paraxial domain. *J. Opt. Soc. Am. A*, 10(7):1553–1561, 1993.

[103] D. Zaleta, M. Larsson, W. Daschner, and S.H. Lee. Design methods for space–variant optical interconnections to achieve optimum power throughput. *Appl. Opt.*, 34(14):2436–2447, 1995.

[104] C. Haupt, A. Kolodziejczyk, and J. Tiziani. Resolution and intensity distribution of output images reconstructed by sampled computer–generated holograms. *Appl. Opt.*, 34(17):3077–3086, 1995.

[105] M.R. Feldman and C.C. Guest. Computer generated holographic optical elements for optical interconnections of very large scale integrated circuits. *Appl. Opt.*, 26(20):4377–4384, 1987.

[106] N.C. Gallagher and B. Liu. Method for computing kinoforms that reduces image reconstruction errors. *Appl. Opt.*, 12(10):2328–2335, 1973.

[107] M. Flemming and M.C. Hutley. Blazed diffractive optics. *Appl. Opt.*, 36(20):4635–4643, 1997.

[108] M.C Nuss and R.L. Morrison. Time–domain images. *Opt. Lett.*, 20(7):740–742, 1995.

[109] H. Bartlet. Computer generated holographic component with optimum light efficiency. *Appl. Opt.*, 23:1499–1502, 1984.

[110] D. Daly, S.M. Hodson, and M.C. Hutley. Fan–out gratings with a continuous profile. *Opt. Commun.*, 82:183–187, 1991.

[111] J.W. Goodman and A.M. Silvestri. Some effects of Fourier–domain phase quantization. *IBM J. Res. Dev.*, 14:478–484, 1970.

[112] S. Sinzinger and M. Testorf. Transition between refractive and diffractive micro–optical components. *Appl. Opt.*, 34:5970–5976, 1995.

[113] D. Kermish. Image reconstruction from phase information only. *J. Opt. Soc. Am. A*, 60:15–17, 1970.

[114] G. Yang. Iterative optimization approach for the design of diffractive phase elements simultaneously implementing several opical functions. *J. Opt. Soc. Am. A*, 11(5):1632–1640, 1994.

[115] U. Mahlab. Genetic algorithm for optical pattern recognition. *Opt. Lett.*, 16(9):648–650, 1991.

[116] R. Brown. Multi–element diffractive optical designs using evolutionary programming. In I. Cindrich and S.H. Lee, editors, *Diffractive and holographic optics technology II*, pages 17–27, 1995.

[117] F. Nikolajeff, S. Jacobsson, and S. Hard. Replication of continuous–relief diffractive optical elements by conventional compact disk injection–molding techniques. *Appl. Opt.*, 36(20):4655–4659, 1997.

[118] N.C. Roberts. Multilevel computer–generated holograms with separable phase functions for beam shaping. *Appl. Opt.*, 31:3198–3200, 1992.

[119] S.K. Case, P.R. Haugen, and O.J. Lokberg. Multifacet holographic elements for wavefront transformations. *Appl. Opt.*, 20:2670–2675, 1981.

[120] W. Singer, H.P. Herzig, and M. Kuittinen. Diffractive beam shaping elements at the fabrication limit. *Opt. Eng.*, 35(10):2779–2787, 1996.

[121] J.R. Leger, D. Chen, and Z. Wang. Diffractive optical elements for mode shaping of a Nd:YAG laser. *Opt. Lett.*, 19(2):108–110, 1994.

[122] Y. Danziger, E. hasman, A.A. Friesem, and A.W. Lohmann. Multilevel diffractive elements for generalized wavefront shaping. *Opt. Eng.*, 35(9):2556–2565, 1996.

[123] L.A.Romero and F.M. Dickey. Lossless laser beam shaping. *J. Opt. Soc. Am. A*, 13(4):751–760, 1996.

[124] D. Dagenais, J. Woodroffe, and I. Itzkan. Optical beam shaping of a high power laser for uniform target illumination. *Appl. Opt.*, 24(5):671–675, 1985.

[125] R.M. Stevenson, M.J. Norman, and T.H. Bett. Binary–phase zone plate arrays for the generation of uniform focal profiles. *Opt. Lett.*, 19(6):363–365, 1994.

[126] J. Bengtsson. Kinoform–only gaussian–to–rectangle beam shaper for semiconductor laser. *Appl. Opt.*, 35(20):3807–3814, 1996.

[127] Q. Cao. Geometrical–transformation approach to optical two–dimensional beam shaping: comment. *Appl. Opt.*, 37(35):8224–8225, 1998.

[128] E.G. Churin. Diffraction–limited laser beam shaping by use of computer–generated holograms with dislocations. *Opt. Lett.*, 24(9):620–622, 1999.

[129] F.M. Dickey and S.C. Holswade. Gaussian laser beam profile shaping. *Opt. Eng.*, 35(11):3285–3295, 1996.

[130] S. Dixit, J. Lawson, K. Manes, and H. Powell. Kinoform phase plates for focal plane irradiance profile control. *Opt. Lett*, 19(6):417–419, 1994.

[131] N.C. Evans and D.L. Shealy. Design and optimization of an irradiance profile–shaping system with a genetic algorithm method. *Appl. Opt.*, 37(22):5216–5221, 1998.

[132] F. Gori. Flattened Gaussian beams. *Opt. Comm.*, 107:335–341, 1994.

[133] D.W. Griffin. Gaussian beam intensity flattener. *Opt. Eng.*, 37(7):2185–2187, 1998.

[134] S. Heinmann. Computer generated beam shaping and focusing optical elements for laser material processing. *Opt. Comm.*, 119:613–622, 1995.

[135] J. Hobfeld, E. Jager, T. Tschudi, and E. Churin. Rectangular focused spots with uniform intensity profile formed by computer generated holograms. *Proc. SPIE*, 1574:159–166, 1991.

[136] T. Kosoburd and J. Kedmi. Beam shaping with diffractive optical elements. *Proc. SPIE*, 1971:390–399, 1993.

[137] M. Kuittinen, P. Vahimand M. Honkanen, and J. Turunen. Beam shaping in the non paraxial domain of diffractive optics. *Appl. Opt.*, 36:2034–2041, 1997.

[138] B. Lu, B. Zhang, and S. Luo. Far–field intensity distribution, M^2 factor, and propagation of flattened Gaussian beams. *Appl. Opt.*, 38(21):4581–4584, 1999.

[139] W. Yen, C. Huang, H. Liu, and L. Lee. A Nd:YAG laser with a flat–top beam profile and constant divergence. *Optics and Laser Technology*, 29(2):57–61, 1997.

[140] J. Zhai, Y. Yan, G. Jin, and M. Wu. Design of kinoform phase plate for spatial beam smoothing. *J. Mod. Opt.*, 46(4):667–674, 1999.

[141] L.L. Doskolovich, N.L. Kazansky, S.I. Kharatinov, and V. Soifer. A method of designing diffractive optical elements focusing into planes areas. *J. Mod. Optics*, 43:1423–1433, 1996.

[142] S. Heinemann. Computer generated beam shaping and focusing optical elements for laser material precessing. *Optics Commun.*, 119:613–622, 1995.

[143] F.S. Roux. Intensity distribution transformation for rotationally symmetric beam shaping. *Opt. Eng.*, 30:529–536, 1991.

[144] A. Aharoni, J.W. Goodman, and Y. Amitai. Beam–correcting holographic doublet for focusing multimode laser diode. *Opt. Lett.*, 18:179–181, 1993.

[145] S. Ogata and Y. Ito. Laser–diode collimating light sources using micro–Fresnel lenses. *Opt. Eng.*, 33:3656–3661, 1994.

[146] A. Aharoni, J.W. Goodman, and Y. Amitai. Efficient beam–correcting holographic collimator for laser diode. *Opt. Lett.*, 17:1310–1312, 1992.

[147] Y. Arieli, N. Eisenberg, A. Lewis, and I. Glaser. Geometrical–transformation approach to optical two–dimensional beam shaping. *Appl. Opt.*, 36(35):9129–9131, 1997.

[148] Y. Arieli, N. Eisenberg, A. Lewis, and I. Glaser. Geometrical–transformation approach to optical two–dimensional beam shaping: erratum and reply to comment. *Appl. Opt.*, 37(35):8226, 1998.

[149] O. Bryngdahl. Computer–generated holograms as generalized optical components. *Opt. Eng.*, 14:426–435, 1975.

[150] J.N. Cederquist and J.R. Fienup. Analytic design of optimum holographic optical elements. *J. Opt. Soc. Am. A*, 4:669–705, 1981.

Index